Multiphysic Modeling of Second Generation Magnetoelectric Materials : application to Connected Objects

Tuan Anh Do

Sorbonne Université

Ecole doctorale : Sciences mécaniques, acoustique, électronique et robotique de Paris

Laboratoire d'Electronique et Electromagnétisme (L2E)

Modélisation multiphysique des matériaux magnétoélectriques de seconde génération : *Application aux objets nomades connectés*

Par Tuan Anh Do

Thèse de doctorat de Sciences de l'ingénierie

Dirigée par Zhuoxiang Ren et Hakeim Talleb

Présentée et soutenue publiquement le 04 Novembre 2019

Devant un jury composé de :

M. Elie Lefeuvre	Professeur, Université Paris Sud, France	Rapporteur
M. Anouar Belahcen	Professeur, Université Aalto, Finlande	Rapporteur
M. Xavier Mininger	Professeur, Université Paris Sud – IUT de Cachan, France	Examinateur
Mme. Souad Ammar Merah	Professeur, Université Paris Diderot, France	Examinateur
M. Zhuoxiang Ren	Professeur, Sorbonne Université, France	Directeur de thèse
M. Hakeim Talleb	Maître de Conférences-HDR, Sorbonne Université, France	Co-directeur de thèse
Mme. Aurélie Gensbittel	Maître de Conférences, Sorbonne Université, France	Encadrant-Examinateur

Acknowledgments

I would like first to express my gratitude to my supervisors Zhuoxiang, Hakeim and Aurélie whose advise, support, and criticism contributed immeasurably to all phases of this thesis work. They had provided excellent motivation throughout my research.

I want to thanks thesis reporters Prof. Elie Lefeuvre and Prof. Anouar Belahcen for reviewing my work. Thanks are also due to Prof. Xavier Mininger for his supports during three years and Prof. Souad Ammar Merah for being committee members.

I want to thank Electronic and Electromagnetism Laboratory member Zhi, Gang, Amine, Ahmed, Lydia, Mounir, Kevin, Yi, Qiang, Joanna, Laurent, Mandiaye, Solofo, Jiajia, Marie-José, Benjiamin, Fengfei, Ning, Matthieu, Ulysse, Rudy, Tianyu, Oussama, Michel, Soroush, Hélène, Muriel, Ghida, Julien, Guido, Massimiliano, Olivier, Kieu An, Hamid, Anna, Thomas, Yves, Chloé, Pascal, George, Gérard, Annie, Aziz, for their support and friendship during three year.

Many thanks also to Phong Bach for his advice in homogenization theory, to Khanh-Chi, Bach Hoang for English checking of my paper.

I give a special thanks to Minh Chien, Tung Trinh, Anh Quan, Quang Tu, Van Nhat, Minh Ngoc, Thang Tran for their moral support and great assistance during my PhD. Their encouragement has kept me going and perhaps more importantly kept me sane.

Paris, 12 September 2019

Preface

The aim of this manuscript is to describe the 3D multi-physic framework for finite element analysis of composite magnetoelectric (ME) developed in our thesis work. Application on ME materials is of great interest nowadays. The development of innovative devices based on these materials is becoming intensive, their research plays a key role. It is essential to develop the modeling tools investigating the materials and optimizing the structures.

ME materials exhibit the magneto-electro-elastic multi-physics coupling. There are two types of ME materials: the intrinsic and the composite (extrinsic), where the ME composite is more interesting because of its higher ME coupling coefficient. The composite material is composed of piezoelectric and magnetostrictive phases. The piezoelectric phase exhibits the electric-elastic coupling, whereas the magnetostrictive phase presents the magnetic-elastic coupling.

In order to investigate the material ME for application on energy harvesting, our laboratory has developed a 2D model. Simulation results show good concordance with the measurements but only valid for simple structures with plane strain or plane stress assumption. In fact, for application in energy transducers, the ME structure is required to be more effective. Thus, the investigation of the influence of the geometry dimension to the output deliverable power is required. A simulation tool which can properly consider the structure effect of the complex interaction is needed for optimal design of the future ME structures, and thus the 3D development is highly required.

The manuscript of the thesis is organized in five chapters.

Chapter 1 is a background review of ME materials and their multiphysics equations. Firstly, the definition of ME effect is introduced and the classification of ME material following the type of coupling effects (single phase and ME composite). Since the class of ME composites generates more power, we focus on this class of ME materials by presenting the principles of ME coupling in the composite as well as in its components (the piezoelectric layer, magnetostrictive layers), for the three types of ME composite (ME laminate composite, ME fiber composite, ME particulate composite). Secondly, some applications of ME materials are reported. Nowadays, the Internet of Things is pervasive which requires the autonomous energy of objects, energy harvesting using ME composite can be very interesting. The final section refers to the multiphysics equations of ME materials. The constitutive laws (coupled and uncoupled), the general equations (mechanic equilibrium, Maxwell-Ampère equation, Gauss law) as well as some existing ME modeling methods will be shortly recalled.

Chapter 2 introduces the 3D multiphysic framework of magnetoelectric (ME) modeling.

After a short introduction, we describe the magnetoelectric problem treated in our work. The analysis in both static and dynamic regimes is considered. Next, the finite element method is introduced. The differential forms (the Whitney forms) approach is used in our study for the discretization of different variables. The linear shape functions associated with the tetrahedral element for node element, edge element, facet element and volume element are reported. Under this framework, the static analysis of ME problem is firstly considered. The general physics equations, the constitutive laws, the state variable equations and the finite element formulations will be all detailed. After that, the methods used to solve the nonlinear problem of magnetostrictive materials are reported. Finally, the harmonic analysis ME considering the eddy current effect will be presented.

In the **chapter 3**, the behavior of ME laminate composites is examined. Two classes of laminate composites (circular section and rectangular section) will be considered. We perform the nonlinear static analysis firstly to determine the material coefficient of the magnetostrictive layers. When all coefficients are obtained, the linear harmonic analysis is performed in taking into account the eddy currents effect. Novel structure and the influence of geometric parameters are analyzed.

Chapter 4 presents the homogenization of two other types of ME composite, the fiber composite and the particulate composite. Finite element analysis of a representative elementary volume and the homogenization principle are described. The effective coefficients are determined and compared with the analytical results by using the analytical approach existed in the literature. Finally, the dynamic and the nonlinear behavior of the effective magnetoelectric coefficient are analyzed.

In the **last chapter**, the conclusions and the future perspective of this work are presented.

Contents

List of Figures

Chapter 1

Introduction

Summary

1.1 Magnetoelectric (ME) composites

1.1.1 Magnetoelectric (ME) effect

The ME effect is firstly reported in 1888 by Wilhelm Röntgen who discovered the magnetization of dielectric material moving in an electric field [1]. In 1894, the possibility of intrinsic ME effect in a non-moving material was reported by Pierre Curie while investigate the symmetry in the physical phenomenon [2].

The magnetoelectric (ME) effect

magnetization induced by an electric field or polarization induced by a magnetic field.

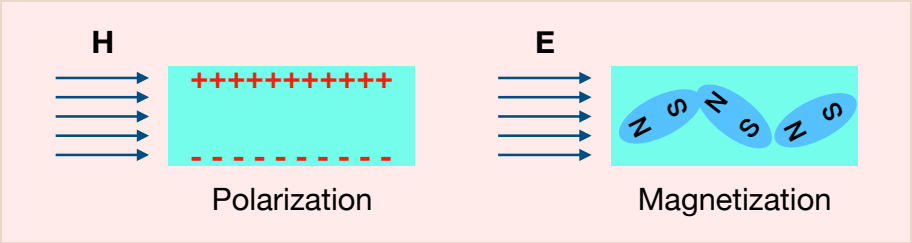

Figure 1.1: Illustration of magnetoelectric effect

The ME behavior is characterized by the ME coefficient α_V. A magnetic field $\boldsymbol{H}$ is applied on a sample where the polarization can be induced as in Figure 1.1. This will generate an electric potential V.

- In static regime:

$$\alpha_V = \frac{V}{H} \tag{1.1}$$

- In dynamic regime:

$$\tilde{\alpha}_V = \frac{\Delta V}{\Delta H} \tag{1.2}$$

Two types of material which exhibit the ME effect:

Single-phase multiferroics: some materials ($RMnO_3$, $BaMF_4$,...) exhibit the ME effect. The asymmetry between the magnetic polar sub lattices of the crystal structure plays a key role [3]. The magnetic-electric coupling in single phase ME is interesting. However, only few materials exhibit this effect at room temperature. For this type of material, the ME coupling is weak and prevents their immediate applications [4], [5].

Multiferroic composite: is a combination of the magnetostrictive material and the piezoelectric material (Figure 1.2). The magnetostrictive material exhibits the mechanic-magnetic coupling while the piezoelectric presents the mechanic-electric

coupling. The composite exhibits a magnetic-electric coupling which does not belong to any of its individual constituent phases.

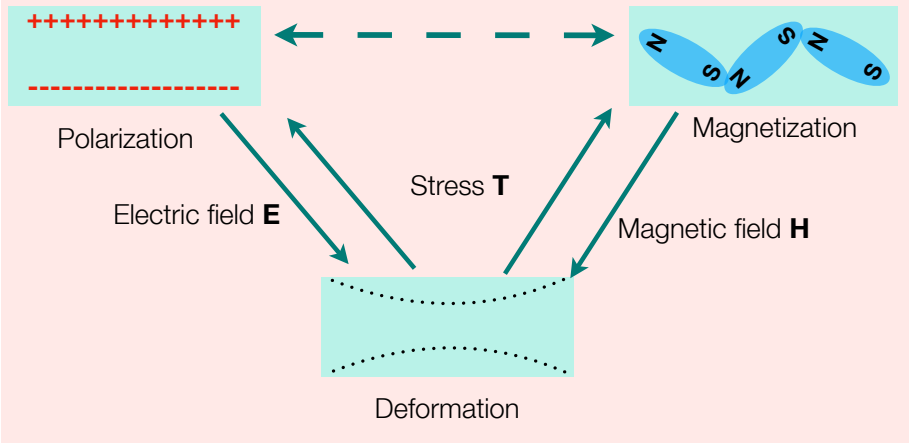

Figure 1.2: Illustration of ME composite

In fact, in a ME composite, the achieved ME coefficient is in the order of magnitude larger than that in intrinsic multiferroics [6]. In addition, the design and synthesis of ME composites offers more flexibility, resulting in cost-effectiveness and freedom in meeting the shape and size constraints. Therefore, our researches will only focus on the ME composite.

1.1.2 Magnetostrictive materials

The magnetic-mechanic coupling can be marked in Joule magnetostriction [7], [8] and Villari effect [9].

Magnetostrictive effect:

Joule magnetostriction: the material is deformed under a magnetic field [7].

Villari effect: The magnetization of material changes when it is subjected to mechanical stress [9].

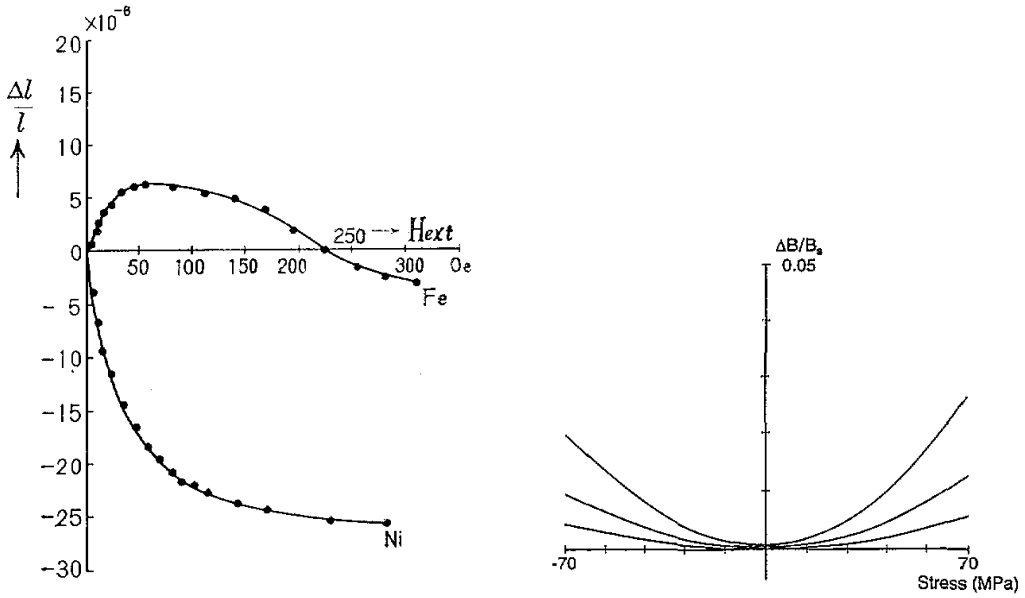

(a) magnetostriction of Fe, Ni

(b) Villari effect

Figure 1.3: Illustration of magnetostrictive effect

The magnetostriction phenomenon was first found in ferromagnetic materials such as Fe, Ni, Co but it is very hard to be recognized. In 1960s, highly magnetostrictive materials which are rare earths elements samarium (Sm), terbium (Tb), dysprosium (Dy) were discovered with the magnetostriction on the order of 200 times larger than nikel [10],[11]. However, this reduces to zeros at room temperature. After that, Terfenol-D, which is an alloy of terbium, iron and dysprosium, is synthetized. The new material can generate high strain under magnetic field at room temperature [12]. Somehow, the application of Terfenol-D is limited in 1D geometry such as rods or bars because of its brittleness. To overcome low tensile strength of Terfenol-D, Gafenol which is an alloy of Fe and Ga was developed [13], [14].

Some applications of magnetostrictive materials:

Magnetostrictive actuator: as shown in Figure 1.4, the actuator can be constituted by a Terfenol-D bar assembled in the electric coil and the magnetic armature. When the electric current in the coil changes, the Terfenol-D bar will be deformed and generates output displacement.

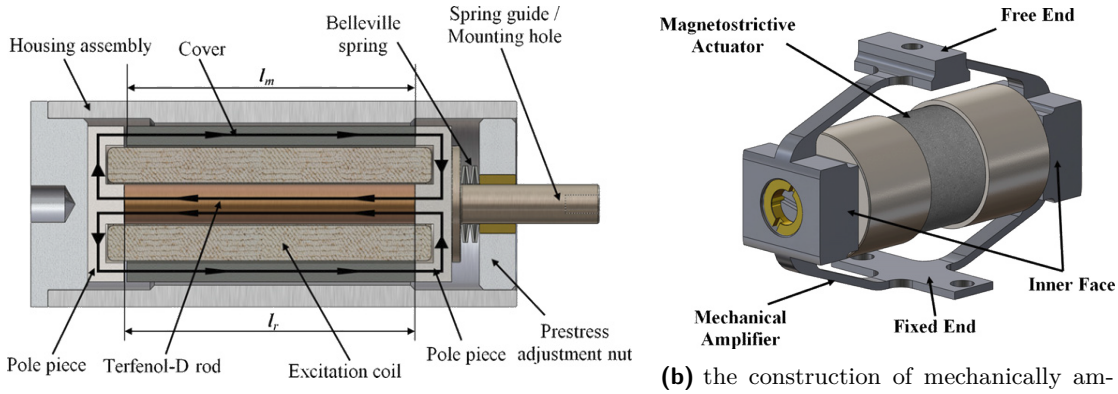

(a) Magnetostrictive actuator configuration

(b) the construction of mechanically amplified magnetostrictive actuator

Figure 1.4: Magnetostrictive actuator [15]

Ultrasonic transducer: The magnetostrictive transducer is composed by a small driving/sensing coil, a biasing magnet, and a magnetostrictive waveguide. (Figure 1.5)

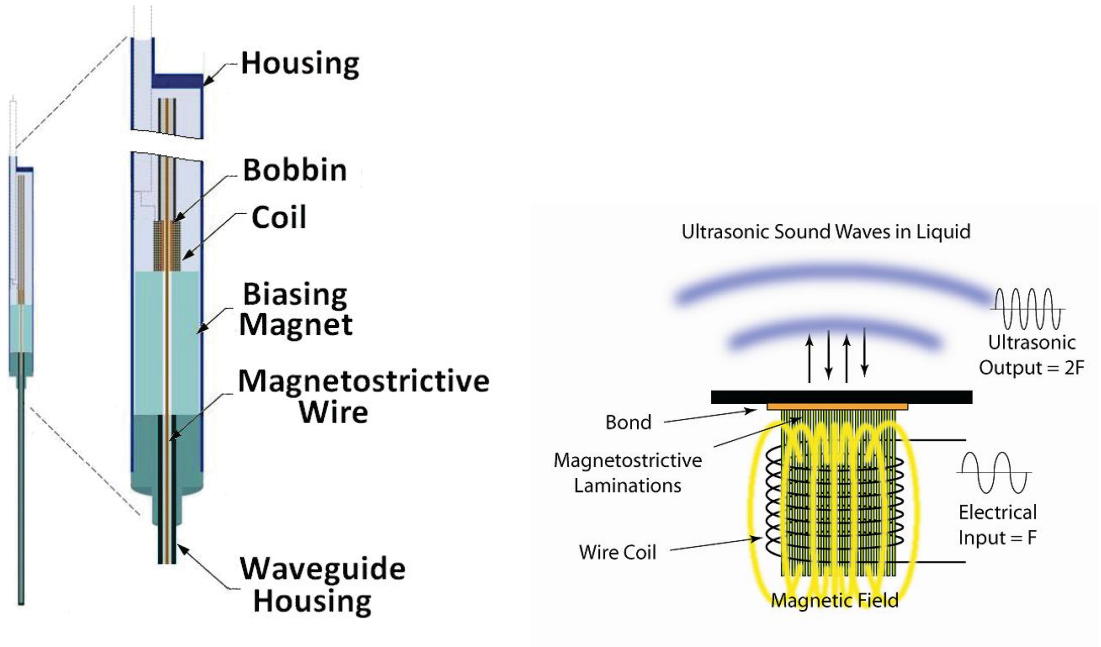

Figure 1.5: Schematic of magnetostrictive transducer design. [16]

Sensor application: The sensor basically consists of a two-part cylinder, with a conducting inner core, preferably made of copper or aluminium, and an outer magnetic thin layer, deposited on the conducting inner core (Figure 1.6)

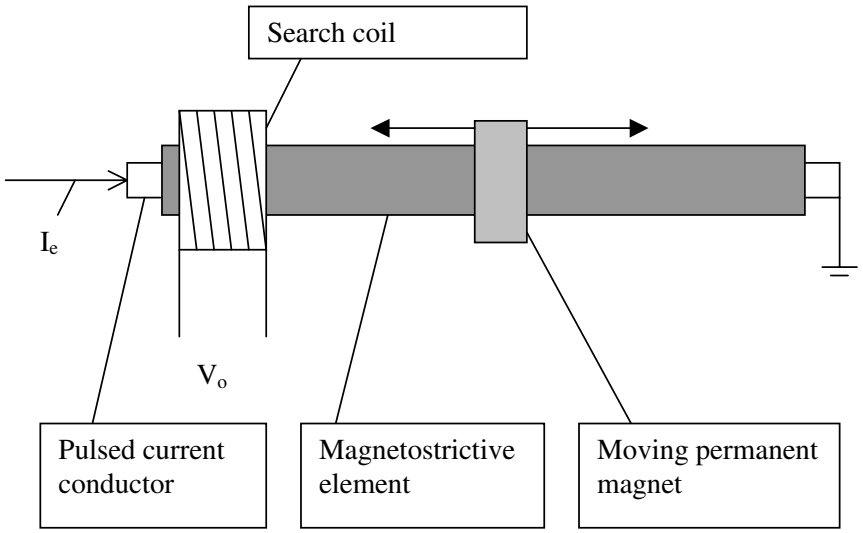

Figure 1.6: Schematic diagram of the magnetostrictive delay lines in measuring position [17]

1.1.3 Piezoelectric materials

Compare to magnetostrictive materials, the piezoelectric materials are more popular. Huge amounts of research about this materials have been presented. The piezoelectric effect is understood as the linear electromechanical interaction between the mechanical and the electrical state in crystalline materials with no inversion symmetry [18].

Piezoelectric effect:

Direct piezoelectric effect: the material is electric polarized when it is subjected to mechanical stress.

Inverse piezoelectric effect: The magnetization is deformed under electric field.

The piezoelectric effect was first discovered by Jacques et Pierre Curie in 1880 [19]. This is a reversible process, the materials exhibit the direct effect also perform the inverse effect.

Some applications of piezoelectric materials:

Vibration control: The piezoelectric, which is inserted on the stator, converts the vibration into a voltage output (Figure 1.7). When the voltage reaches the maximum value, this can be reversed by synchronized switch damping on inductor.

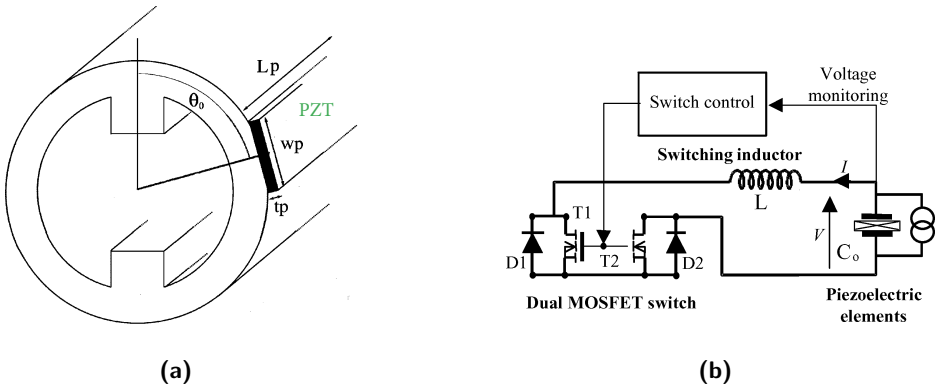

Figure 1.7: Piezoelectric actuator for vibration control in electric motor. (a) PZT integrated in switched reluctance machine (b) Schematic diagram of the circuit used for the synchronized switch damping on inductor technique [20]

Acoustic transducer: Figure 1.8 introduce a cantilever beam structure made by thin film PZT layer.

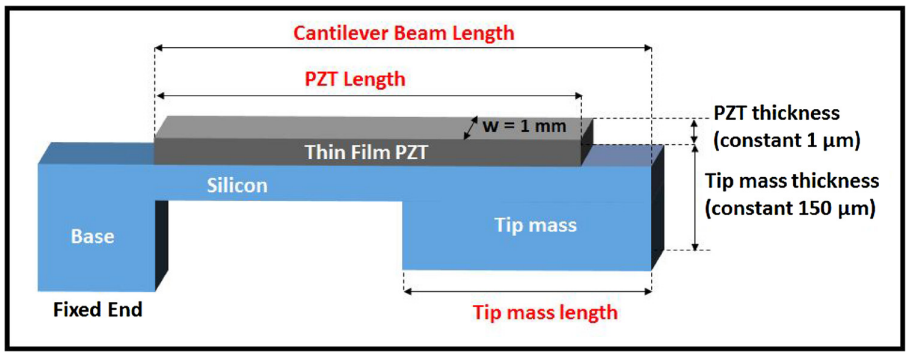

Figure 1.8: Schematic of piezoelectric acoustic transducer [21]

Piezoelectric motor: Figure 1.9 proposes a new type of micro rotary motor with a single piezoelectric stack actuator. When an electric field is applied, this results in the vibration of the piezoelectric stack actuator.

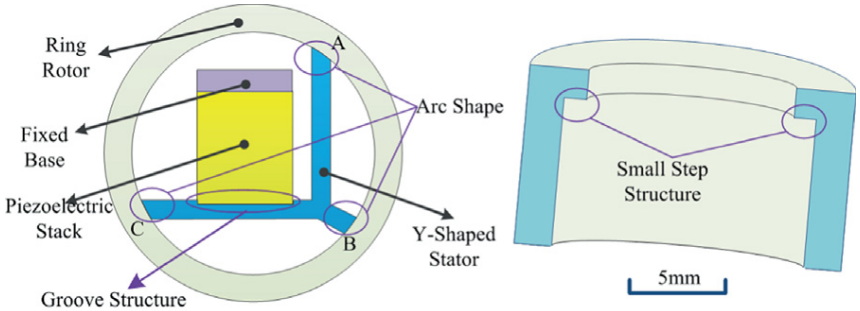

Figure 1.9: Schemes of the piezoelectric motor [22]

Energy harvesting: The piezoelectric materials can be used for energy conversion. Fig-

ure 1.10 presents a 3D piezoelectric microsystem that consists of a layer of piezoelectric polymer and metals electrodes on the top and bottom surfaces.

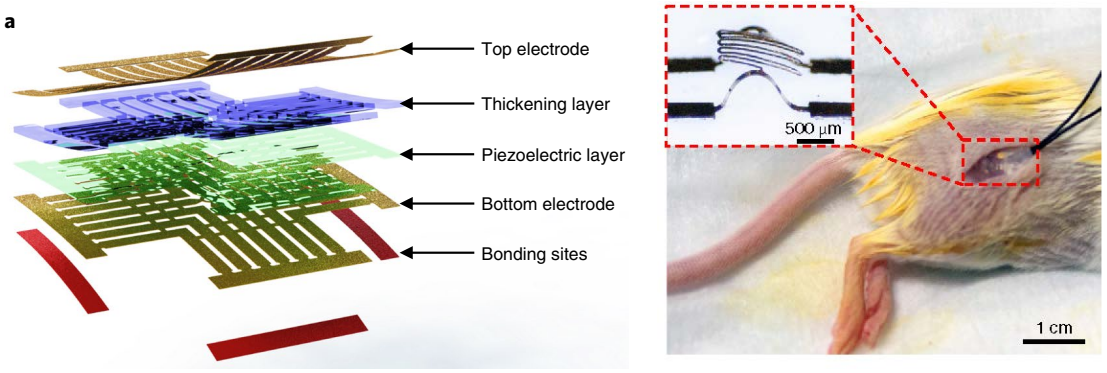

(a) Illustration of 3D PVDF mesostructure with top and bottom electrode

(b) piezoelectric energy harvester implanted into the hind leg of a mouse

Figure 1.10: Piezoelectric for energy harvesting [23]

1.1.4 Magnetoelectric composites

Many researches have been conducted to find the ME composites which can exhibit such a strain-mediated ME effect at room temperature. Many of them have been used in various applications. According to the geometry structure formed by magnetostrictive and piezoelectric phases, the ME composites can be categorized into three groups [24]: the 0-3, 2-2, 1-3 where the number refers to the connectivity of each phase (Figure 1.11).

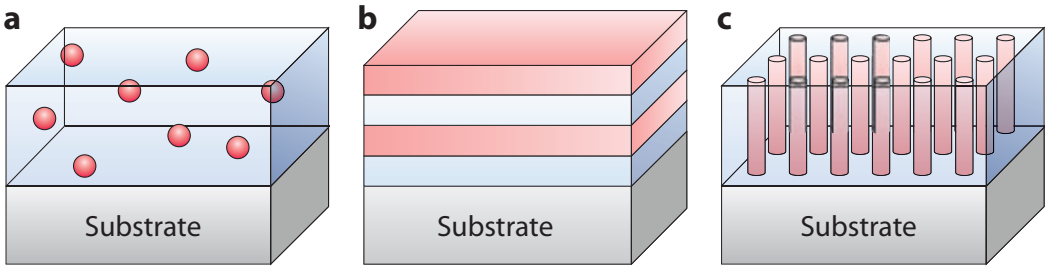

Figure 1.11: Three types of two-phase composite materials (a) 0-3 particulate nanocomposite films with magnetic particles (0) embedded in a ferroelectric film matrix (3); (b) 2-2 horizontal heterostructure with alternating ferroelectric (2) and magnetic (2) layers, or simply a ferroelectric (or magnetic) thin film grown on a magnetic (or ferroelectric) substrate; and (c) 1-3 vertical heterostructure with one-phase fiber (1) embedded in a matrix of another phase (3). [25]

Magnetoelectric laminate composite: The laminated ME composites are very promising ME materials at which the good coupling can be obtained at the ferroelectric and ferromagnetic interfaces. For this type of structure, the material can have much better ME coupling, larger ME anisotropy and higher resonance response in a wide frequency range [6], [26], [27].

Magnetoelectric fiber composite: A known fiber composite structure is a self-assembled nanostructured thin film formed on the substrate [28]. The heterostructure consists of piezoelectric matrix reinforced by nanopillars ferromagnetic. This structure performs a strong ME coupling.

Magnetoelectric particulate composite: To compare with the laminate composite, the 0-3 type particulate ME composites are interesting because of easy processing and it does not require additional adhesives for mechanical contact [29]. Due to the brittleness of Terfenol-D, the magnetic particles are often embedded in a piezoelectric matrix.

Beside the three types of composite, there are also novel designs which are the combination of these ideas to overcome the shortcomings of the classical composite. In [30], the magnetoelectric quasi (0-3) nanocomposite heterostructures are presented. The new structures get over the limitation of film connectivity of laminated composite [31] and also significantly suppress the leakage current paths due to the low resistivity of the interconnected ferromagnetic phase.

The composites can generate ME behavior by combining the magnetostrictive and the piezoelectric materials which in themselves do not exhibit the ME effect. Thanks to the mechanical coupling, an applied magnetic field induces electric polarization [32].

Properties of ME composites:

Nonlinear behavior: The ME composites have nonlinear dependencies with respect to the magnetic field (Figure 1.12) because of the nonlinear magnetostrictive response. When the magnetic field increase, the achieved ME coefficient increase until the maximal value (saturation magnetization) and decrease after that. In practical, to obtain the optimal configuration, the composite is applied by a dynamic magnetic field pre-magnetized by magnetostatic biasing. The optimal value of magnetic static field is at which the ME coefficient is maximal.

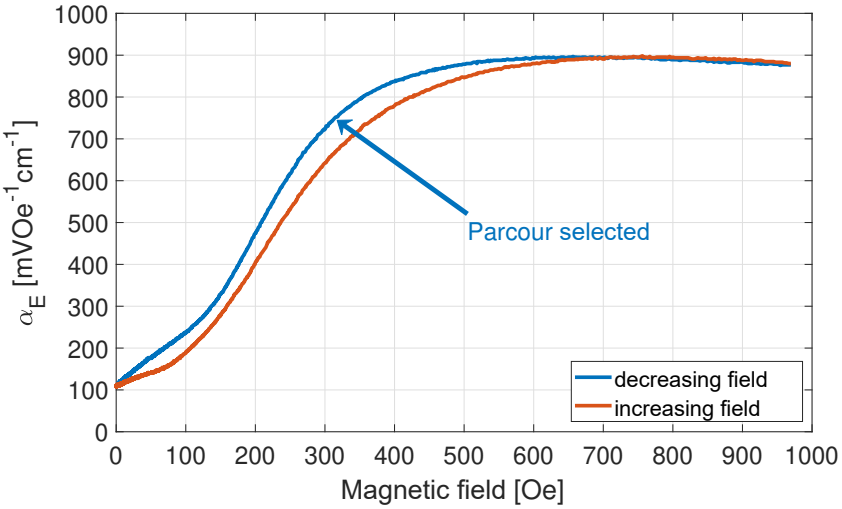

Figure 1.12: Measurement of ME coefficient for sample laminate composite [33]

Frequency dependence: Especially for laminate composite, the obtain ME coefficient

is observed very high at resonance frequency (Figure 1.13 [34]). This particular property has attracted many scientific researches. Working around the resonance frequency will make the materials more effective. In another aspect, as the magentostrictive layer is conductive, the effect of eddy currents is important at higher frequency.

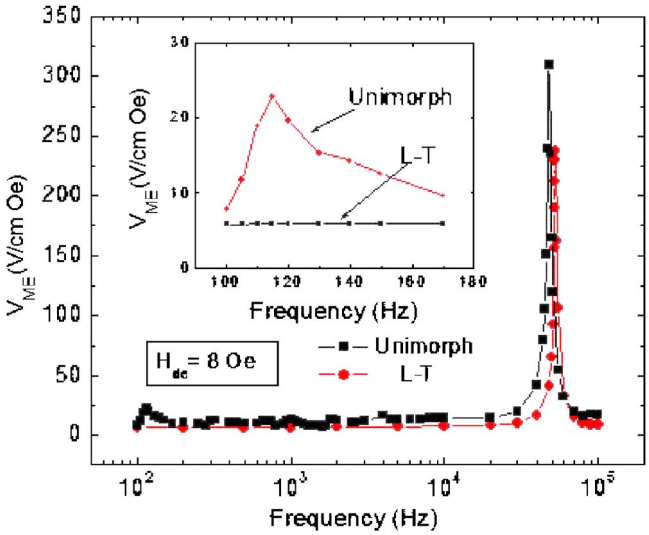

Figure 1.13: Frequency dependence of the ME voltage coefficient of both three-layer Metgals (SA1)/PVDF and unimoprh Metglas (CO)/PVDF laminates

1.2 Applications of ME composites

1.2.1 Energy haverting and Internet of Things (IoT)

The evolution of internet and IoT

The research on the internet design was started in 1973; the network became operational in 1983. The internet was firstly reserved for technological, academic, research elite. From the very early days when it was a group of machines all hooked together with email and very little functional, the internet is evolved to a platform where people can share knowledge, find information, have tele-conferences or meetings that may be miles away. The internet is changing in profound ways, it's no longer just means of communication. The Internet of Things (IoT) means the internet doesn't just collect and distribute information, it can also feel and intelligently respond.

Smart cities – IoT scenarios

The evolution of internet creates the IoT connecting physical devices and everyday objects. These objects are embedded with sensors and internet connectivity to communicate and interact with other objects. For example, IoT brings a new concept of smart cities [35] which contain intelligent, virtual, digital, information cities. The design of smart city is

changing depending on the information and communication technology. In general way, municipalities around the globe use IoT sensors to collect data in order to enhance their services, reduce costs and improve interaction [36]. The smart city innovation is expected to improve human life with more efficient water supply, an innovative solution to traffic congestion, more reliable public transportation, energy-efficient buildings, improved public safety... Contribute to the development of smart cities, more and more IoT devices are fabricated.

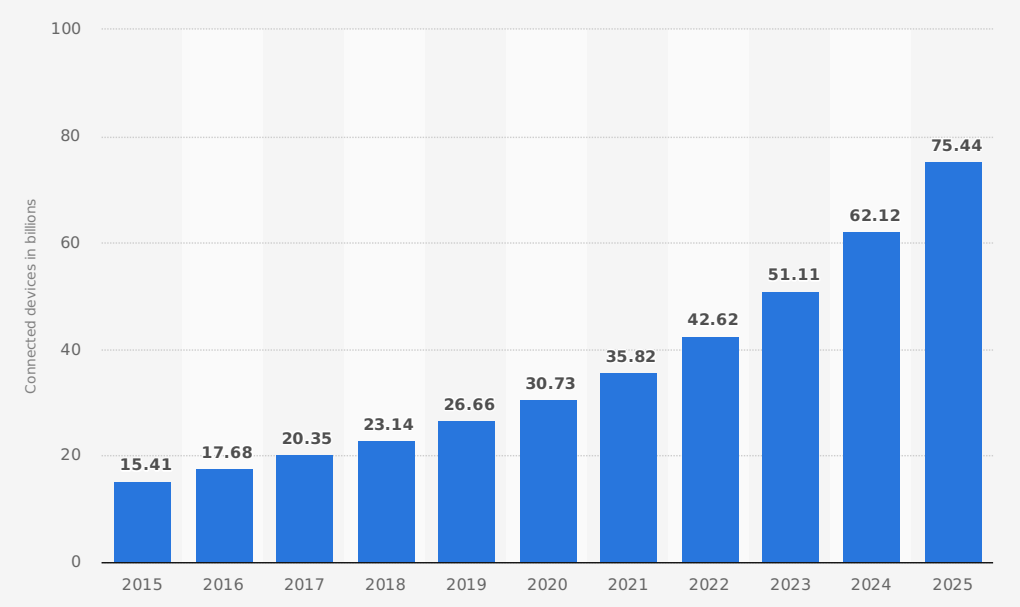

Figure 1.14: IoT connected devices installed worlwide from 2015 to 2025. Source: IoT platforms: enabling the Internet of Things, March 2016 [37].

As shown in Figure 1.14, the number of IoT installed devices is around 15.4 billion in 2015 and is predicted to be 30.7 billion in 2020, 75.4 billion in 2025 according to IHS forecast.

However, the main problem remains on that of the energy supply modes. The object interconnection project is seen on a large scale. The recovery of information is envisaged on very numerous objects but also physically spaced from each other, sometimes on huge surfaces. The objects are therefore considered autonomous, without any wire. When the data is exchanged without wires, the energy stays wired. The use of batteries remains the main way to overcome this problem. However, this requires recharging or replacing the batteries by an outside operator, but it is sometimes very difficult to access the objects. To solve the energy need problem, the self-powering remote sensors using wireless power transmission techniques can be the solution.

Magnetoelectric transducer – self-powering devices

Many researches on energy harvester are being conducted to solve the power requirements problem of wireless sensor networks. There are ways of energy collection from environment using materials such as piezoelectric, magnetoelectric, inductive, photovoltaic, dielectric ...materials. The efficiency of the materials is optimized following various applications

[38], [39], [40]. For a wireless network, magnetic field energy harvesting by magnetoelectric composite provides a great potential.

For energy harvesting applications, the working principle of the ME composite is shown in Figure 1.15. The composite is magnetized by a dynamic magnetic field H_{ac} with an additional DC magnetic bias. Since the material behavior is nonlinear, it is necessary to find the optimum magnetic DC bias so that the ME composite can generate maximum output voltage. When a dynamic magnetic field is applied, the magnetostrictive layers will be deformed. This results a stress field on the piezoelectric layer. The electrodes is put on the opposite surfaces of piezoelectric layer for the electric polarization, which are also going to allow an electrical contact and connect the output load of the transducer ME that represents the object to supply the electric energy.

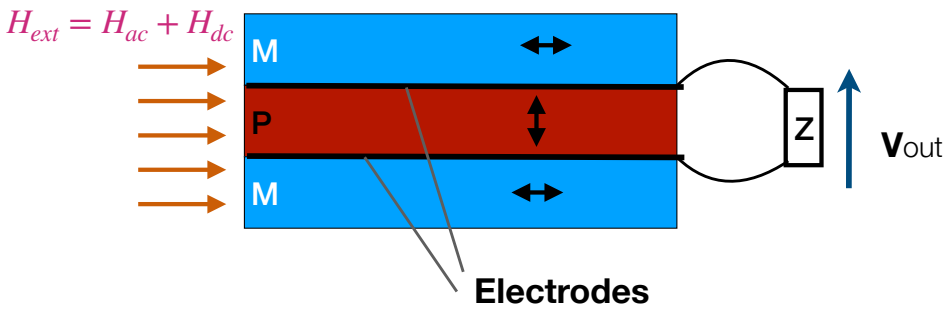

Figure 1.15: Working principle of ME energy harvesting

The number of investigation of ME energy harvesting is still limited. From 2000 to 2010, several researches on energy recovery from unused sources and for self-powered sensors were developed [41], [42], [43], [44], [45], [46]. In [47], the fork composite structure with power management circuit to increase the output power is presented. To improve the way the sensors utilizing ME phenomenon in the absence of a DC magnetic field, a self-biased magnetoelectric energy harvester can be considered [48], [49].

1.2.2 Other applications

Beside the energy transducer applications, the ME composites exhibiting strong coupling coefficient have been used for various applications [50].

Magnetic sensor

ME composite can be integrated in an ultra-sensitive magnetic sensor for brain activity recording technique based on measurement of magnetic fields generated by brain. Because of the natural properties and self-powered operation at room temperature, this can replace other expensive techniques which require cryogenic conditions. Figure 15 is an illustration of resonant magnetic field sensor. An ultra-sensitive DC magnetic field detective for electro-magneto-brain activity was presented in [52]. Research in [53] proposed novel technique using ME effect of multiferroic nanoparticles for examine local electric fields in

response to neural activity in real time. A ME microcantilever, which capable of measuring minimum magnetic field up to $1 * 10^{-12}$ T, consists of Terfenol-D and PZT is introduced in [54]. To overcome the detection limit, a thin film ME heterostructures was investigated in [55].

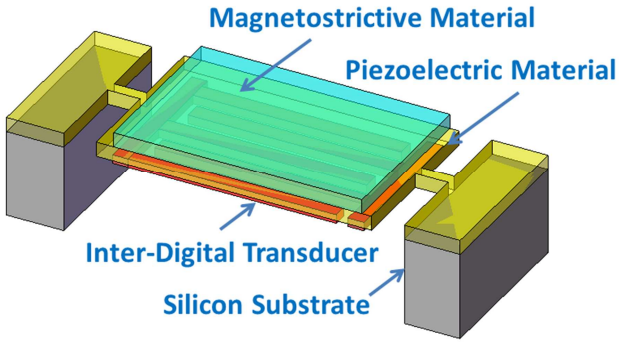

Figure 1.16: 3D schematic representation of the proposed MEMS resonant magnetic field sensor in [51]

Phase shifter

Microware phase shifters are used in oscillators and phased array antenna systems. A ME phases shifter composed by YIG and PZT was studied in [52]. This technique reduces power dissipation compared with traditional phase shifter based on Faraday rotation for electromagnetic waves.

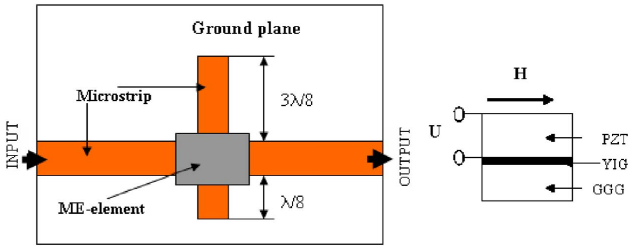

Figure 1.17: ME phase shifter [56]

Resonator

Resonator is a device generating waves of specific frequencies, used in phased array radars, filters and phase shifters. The employments of ME composite, replacing ferrite materials, are less noisy, low power consumption.

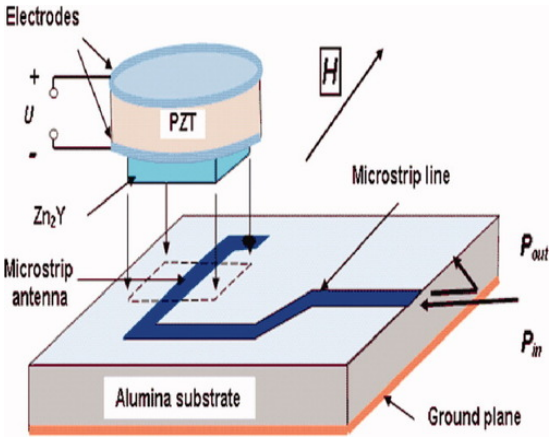

Figure 1.18: ME resonator [57]

Inductors

A novel application of ME composite is inductor, one of three fundamental components for electronic circuits. The principle of the variable inductance, using the ME material, is as follows: the static electric field induces the deformation of the piezo-

electric element. The polarization point of
the magnetostrictive element varies as a function of the deformation transmitted by the piezoelectric element. The advantage of ME inductor is tuning magnetic properties by electric field at low fields.

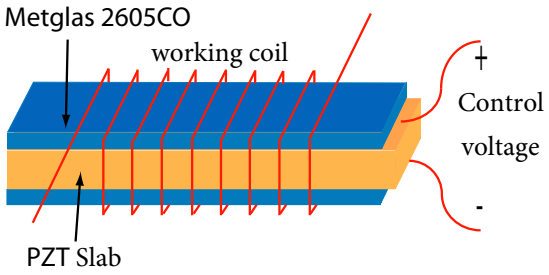

Figure 1.19: Tunable inductor [58]

1.3 Physical equations of ME materials

1.3.1 Constitutive laws

The ME composite functionality interacts with many physical phenomena at different scales. The coupled effects are the interaction between the magnetics, the mechanics and the electrostatics while the thermal effect is ignored. For example, the magnetostrictive behavior is recognized when the material deformed under magnetic field whereas the piezoelectric behavior is the electric polarization under stress. The response of material under applied loading depends on the constitutive laws. In general, the loading can be mechanical force, magnetic or electric field. For energy transducer, it's the magnetic field. The response is the strain, magnetic induction or electric displacement. In this section, the uncoupled behavior is presented firstly, the coupled behavior is afterwards.

Uncoupled constitutive laws

- **Mechanics**

  In linear elasticity, the Cauchy stress $\boldsymbol{T}$ (N/m^2) refers to the force divided by area. Under an applied force, the mechanical strain S can be obtained by Hooke's law:

  $$\boldsymbol{T} = c\boldsymbol{S}, \tag{1.3}$$

  where $\boldsymbol{T}$ and $\boldsymbol{S}$ are second-order tensors (3x3) and c is called the stiffness tensor (N/m^2) which is a fourth-order tensor (3x3x3x3). The expression of the Hooke's law needs the use of quantities with four indexes, which can be somewhat cumbersome and heavy. Therefore, some simplified notations have been proposed. As $\boldsymbol{T}$ and $\boldsymbol{S}$ are both symmetric, they have six independent entries. They allow the representation by a vector (6x1), the fourth-rank tensor is switched to 6x6 square symmetric matrix. The most well-known of the matrix formalisms for anisotropic elasticity is that of Voigt [59]. The Voigt representation is presented in Appendix A.1.

The mechanical response of material can be also expressed in the displacement field $\boldsymbol{u}$ (m), which is linked with the strain tensor $\boldsymbol{S}$ by the following:

$$\boldsymbol{s} = \mathfrak{D}\boldsymbol{u} = \frac{1}{2}(\text{grad } \boldsymbol{u} + \text{grad } {}^t\boldsymbol{u}), \tag{1.4}$$

where $\boldsymbol{u}$ is a vector (3x1), refers to three directions of movement. The operation X^t denotes the transposition operation over X.

- **Magnetics**

In uncoupled-magnetic problem, the magnetic induction $\boldsymbol{B}$ (T) can be computed from the magnetic field $\boldsymbol{H}$ (A/m) through:

$$\boldsymbol{B} = \mu\boldsymbol{H}, \tag{1.5}$$

where $\boldsymbol{B}$ and $\boldsymbol{H}$ are vectors (3x1), μ (H/m) is the permeability which is a second-order tensor (3x3).

- **Electrostatics**

In uncoupled-electrostatic problem, the electric displacement $\boldsymbol{D}$ (C/m^2) can be computed from the electric field $\boldsymbol{E}$ (V/m) through:

$$\boldsymbol{D} = \varepsilon\boldsymbol{E}, \tag{1.6}$$

where $\boldsymbol{D}$ and $\boldsymbol{E}$ are vectors (3x1), is ε (F/m) is permittivity which is a second-order tensor (3x3).

Coupled constitutive laws

- **Linear piezoelectricity**

For linear piezoelectricity, the mechanical-piezoelectric coupling refers to the relation between electric the displacement $\boldsymbol{D}$, the stress $\boldsymbol{T}$ and the electric field $\boldsymbol{E}$, the strain $\boldsymbol{S}$ (following IEEE standard [60]).

$$\begin{cases} \boldsymbol{T} = c^E\boldsymbol{S} - (e)^t\boldsymbol{E} \\ \boldsymbol{D} = e\boldsymbol{S} + \varepsilon^S\boldsymbol{E} \end{cases} \tag{1.7}$$

where c^E and ε^S are respectively, the elastic under constant electric field and permittivity coefficient under constant strain. e (NV-1m-1) denotes the piezoelectric coefficient (6x3). An alternative system to present the constitutive laws is also widely used:

$$\begin{cases} \boldsymbol{S} = s^E\boldsymbol{T} - (d)^t\boldsymbol{E} \\ \boldsymbol{D} = d\boldsymbol{T} + \varepsilon^T\boldsymbol{E} \end{cases} \tag{1.8}$$

where s^E and ε^T are respectively, the compliance at constant electric field, permittivity at constant stress, d (6x3) is the piezoelectric coefficient (C/N). This leads the following relations:

$$s^E = [c^E]^{-1} \tag{1.9}$$

$$e = dc^E \tag{1.10}$$

$$\varepsilon^S = \varepsilon^T - de^T \tag{1.11}$$

The matrix presentation of these coefficients is given in the Appendix A.2

- **Linear magnetostrictive laws**

The magnetic-mechanical coupling refers to the relations between the stress, the magnetic field and the strain, the magnetic induction (IEEE standard [61])

$$\begin{cases} \boldsymbol{T} = c^B \boldsymbol{S} - (h)^t \boldsymbol{B} \\ \boldsymbol{H} = -h\boldsymbol{S} + \nu^S \boldsymbol{B} \end{cases} \tag{1.12}$$

where c^B and ν^S are respectively, the elastic coefficient under constant magnetic induction and the reluctivity under constant strain. h ($\mathrm{NA^{-1}m^{-1}}$) denotes the piezomagnetic coefficient (6x3). We can also re-write:

$$\begin{cases} \boldsymbol{S} = s^H \boldsymbol{T} - (d_m)^t \boldsymbol{H} \\ \boldsymbol{B} = -d_m \boldsymbol{T} + \mu^T \boldsymbol{H} \end{cases} \tag{1.13}$$

where s^H and μ^T are respectively, the compliance at constant magnetic field, permeability at constant stress, d (6x3) is the piezomagnetic coefficient (m/A).

- **Nonlinear magnetostrictive laws**

Considering nonlinear behaviors, the material properties is expressed as functions of magnetic field and stress state

$$\begin{cases} \boldsymbol{S} = s(\boldsymbol{H},\boldsymbol{T})\boldsymbol{T} - (d_m(\boldsymbol{H},\boldsymbol{T}))^t \boldsymbol{H} \\ \boldsymbol{B} = -d_m(\boldsymbol{H},\boldsymbol{T})\boldsymbol{T} + \mu(\boldsymbol{H},\boldsymbol{T})\boldsymbol{H} \end{cases} \tag{1.14}$$

The determination of material properties $c(\boldsymbol{H},\boldsymbol{T})$, $h(\boldsymbol{H},\boldsymbol{T})$, $\mu(\boldsymbol{H},\boldsymbol{T})$ is needed for the FEM analysis. In order to compute material coefficients, we can use the B-H, S-H curves which are obtained from experimental or numerical model.

$$\zeta = \begin{bmatrix} \mu^S = \dfrac{\partial \boldsymbol{B}}{\partial \boldsymbol{H}}(\boldsymbol{H}_0,\boldsymbol{T}_0) & d_m = \dfrac{\partial \boldsymbol{B}}{\partial \boldsymbol{T}}(\boldsymbol{H}_0,\boldsymbol{T}_0) \\ d_m^t = \dfrac{\partial \boldsymbol{S}}{\partial \boldsymbol{H}}(\boldsymbol{H}_0,\boldsymbol{T}_0) & s^H = \dfrac{\partial \boldsymbol{S}}{\partial \boldsymbol{T}}(\boldsymbol{H}_0,\boldsymbol{T}_0) \end{bmatrix} \tag{1.15}$$

Jiles-Atherton model is a popular model to describe the magnetic hysteresis [62]. This approach is only valid for isotropic materials. The other analytic model is to use polynomial which is fitted with the measurement [63]. However, application of these models in 3D problem seems to be complex. Armstrong models [64] or multi-scale model [65] developed energy-averaged models based on the energy-weighted of the domains orientation and evaluate the energy contributions of these domains. Nevertheless, the model

requires energy estimation for all possible orientations which are time consuming. Evans and Dapino [66] presented the discrete energy averaged model (DEAM), reducing the number of directions to six easy axis. It is this model adopted in our study. Its principle is shortly described below.

Firstly, the magnetic induction and the strain in magnetostrictive phase is determined by the relation:

$$\begin{cases} \boldsymbol{S} = s\boldsymbol{T} + \boldsymbol{S}_m \\ \boldsymbol{B} = \mu_0(\boldsymbol{H} + \boldsymbol{M}) \end{cases} \tag{1.16}$$

where the strain $\boldsymbol{S}$ is decomposed purely in mechanical part and in magnetostriction $\boldsymbol{S}_m$. $\boldsymbol{M}$ (3x1) denotes the magnetization (A/m) and μ_0 is the permeability of the free space ($4\pi 10^{-7}$ Hm^{-1}). The magnetization and the magnetostriction are determinated by averaging these values along six easy axis:

$$\begin{cases} \boldsymbol{S}_m = \Sigma_{k=1}^{6} \xi_{an}^k \boldsymbol{S}_m^k \\ \boldsymbol{M} = M_s \Sigma_{k=1}^{6} \xi_{an}^k \boldsymbol{m}^k \end{cases} \tag{1.17}$$

where m^k, $\boldsymbol{S}_m^k$, ξ_{an}^k is the magnetization, the magnetostriction and the averaged anhysteretic volume fraction of each orientation, which are related to energy minimization of the easy axis. The energy of a domain close to the easy axis $\boldsymbol{c}^k$ is estimated by:

$$G^k = \frac{1}{2} K^k |\boldsymbol{m}^k - \boldsymbol{c}^k|^2 - \boldsymbol{S}_m^k \cdot \boldsymbol{T} - \mu_0 M_s \boldsymbol{m}^k \cdot \boldsymbol{H}, \tag{1.18}$$

and simplified as

$$G^k = \frac{1}{2} \boldsymbol{m}^k \cdot \boldsymbol{K}^k \boldsymbol{m}^k - \boldsymbol{m}^k \cdot \boldsymbol{B}^k \tag{1.19}$$

with

$$\boldsymbol{K}^k = \begin{bmatrix} K^k - 3\lambda_{100} T_1 & -3\lambda_{111} T_4 & -3\lambda_{111} T_6 \\ -3\lambda_{100} T_4 & K^k - 3\lambda_{100} T_2 & -3\lambda_{111} T_5 \\ -3\lambda_{111} T_6 & -3\lambda_{111} T_5 & K^k - 3\lambda_{100} T_3 \end{bmatrix}$$

$$\boldsymbol{B}^k = \begin{bmatrix} c_1^k K^k + \mu_0 M_s H_1 & c_2^k K^k + \mu_0 M_s H_2 & c_3^k K^k + \mu_0 M_s H_3 \end{bmatrix}^t$$

The minimization problem is formulated as eigenvalue problem

$$(\boldsymbol{K} - \gamma \boldsymbol{I}) \boldsymbol{m}^k = \boldsymbol{B}^k \tag{1.20}$$

where $\boldsymbol{I}$ is the sixth order matrix, γ is unknown eigenvalue. The solution for $\boldsymbol{m}^k$ is given as following:

$$\boldsymbol{m}^k = (\boldsymbol{K}^k)^{-1}\left[\boldsymbol{B}^k + \frac{1 - \boldsymbol{c}^k \cdot (\boldsymbol{K}^k)^{-1}\boldsymbol{B}^k}{\boldsymbol{c}^k \cdot (\boldsymbol{K}^k)^{-1}\boldsymbol{B}^k}\boldsymbol{c}^k\right] \tag{1.21}$$

From that, $\boldsymbol{S}_m$ can be obtained by :

$$\boldsymbol{S}_m = \begin{bmatrix} \frac{3}{2}\lambda_{100}(m_1^k)^2 \\ \frac{3}{2}\lambda_{100}(m_2^k)^2 \\ \frac{3}{2}\lambda_{100}(m_3^k)^2 \\ 3\lambda_{111}m_1^k m_2^k \\ 3\lambda_{111}m_3^k m_2^k \\ 3\lambda_{111}m_1^k m_3^k \end{bmatrix} \tag{1.22}$$

These results allow us to determine the energy in equation 1.19, the anhysteretic can be computed by:

$$\xi_{an}^k = \frac{\exp(-G^k/\Omega)}{\Sigma_{j=1}^6 \exp(-G^j/\Omega)} \tag{1.23}$$

Finally, the magnetostriction and magnetization in equation 1.16 can be estimate to characterize the nonlinear behavior of the material.

1.3.2 General physical equations

To study the magnetoelectric problem, we consider in this section respectively the mechanic, the electric and the magnetic problems. The influence of temperature is neglected.

- **Mechanic equilibrium**

  In mechanic static, the balance of linear momentum can be expressed as:

$$\text{div}\ \boldsymbol{T} + \boldsymbol{f} = 0, \tag{1.24}$$

  where $\boldsymbol{f}$ (Newton) is the volume force vector (3x1).

Under dynamic excitation:

$$\text{div } \boldsymbol{T} + \boldsymbol{f} = \rho \frac{d^2 \boldsymbol{u}}{dt^2} \tag{1.25}$$

where ρ (kg/m^3) is the density.

- **Electrostatic field equation**

$$\text{curl } \boldsymbol{E} = 0 \tag{1.26}$$

We can introduce scalar electric potential V

$$\boldsymbol{E} = -\text{grad } V \tag{1.27}$$

- **Gauss's law**

Gauss's law states how electric field behave around electric charge

$$\text{div } \boldsymbol{D} = \rho_V \tag{1.28}$$

ρ_V is the electric charge density

- **Maxwell-Faraday equation**

The electromagnetic induction is described as

$$\text{curl } \boldsymbol{E} = \frac{d\boldsymbol{B}}{dt} \tag{1.29}$$

- **Maxwell-Ampere equation**

The Maxwell-Ampere law relates electric currents and magnetic field, which describes the magnetic fields that result from a transmitter wire or loop in electromagnetic.

$$\text{curl } \boldsymbol{H} = \boldsymbol{J} + \frac{d\boldsymbol{D}}{dt} \tag{1.30}$$

Where $\boldsymbol{J}$ denotes free current density (A.m^{-2})

- **Gauss's law for magnetism**

$$\text{div } \boldsymbol{B} = 0 \tag{1.31}$$

Due to the Helmholtz decomposition theorem, a magnetic vector potential can be introduced

$$\boldsymbol{B} = -\text{curl } \boldsymbol{a} \tag{1.32}$$

- **Ohm's law**

Since the magnetostrictive layer is conductive material, the vector form of Ohm's law describes the eddy current induced in magnetostrictive layer:

$$\boldsymbol{J}_c = \sigma \boldsymbol{E} \tag{1.33}$$

with $\boldsymbol{J}_c$ is the current density and σ (Siemens) is conductivity constant which depends on the material properties.

1.3.3 Existing models

The ME composites have attracted scientific interests for applications such as energy harvesters, sensors, resonators, phase shifters ... The requirement for engineering applications is a high ME voltage coefficient, which can be upgraded by the synthesis of new materials or the optimal design of ME structures. Many experimental researches have been conducted to improve the performance of ME composite. However, the laborious tests can be overlong and expensive. Therefore, numerical simulation methods are highly desired.

The numerical modeling of the ME composite exists in electronic scale, atomic scale and mmacrocopic scale. At the electronic scale, density function theory (DFT) predicts electronic and lattice contributions to the ME coupling of these materials [67], [68]. Understanding low-energy states of ME materials under various condition rely on effective Hamiltonian approach at the atomistic scale [69], [70]. On the macroscale, the approaches are based on the constitutive laws and equilibrium equations. Our works focus on the modelling of ME composite at the macroscopic scale as an application for energy harvester.

The development of analytical or numerical models of constitutive laws is necessary to analyze the multiphysics behavior and to investigate the ME composite voltage coefficient or to investigate the output deliverable power when the ME composite is used as an energy transducer. The first linear model for magnetostrictive materials is presented in [71] considering no hysteresis effects. For laminate magnetoelectric composite, based on the constitutive equations and the averaging method, the static response of ME composite has been performed [72], [73], [74], [75]. As these approaches do not take into

account the coupled equation of motion for the laminate, a magneto-elasto-electric coupling equivalent circuits in [76] analyzes ME effect of Terfenol-D/PZT at low-frequency and resonance-frequency. Moreover, an analytical approach using the simultaneous solution of electrostatic, magnetostatic and elasto-dynamic equations in [77], [78] estimates the frequency dependence of ME voltage coefficient. In order to consider the geometry-dependence, [79] develop an average-field method. Following this, the impact of length and width fractions for the piezoelectric or magnetostrictive components on ME composite performance is evaluated. Next, because the response of magnetostrictive materials depends on the magnetic bias field, [80] employed the equivalent circuit method to establish an analytical nonlinear magnetic–mechanical–electric coupling model in which nonlinear magnetostrictive constitutive relations are adopted. Furthermore, the influence of residual stress during the processing and preparation of magnetoelectric devices is prefigured also. For the Terfenol-D or Galfenol, the conductivity is usually strong ($\approx 10^6$ S/m), [81], [82] introduced the complex permittivity model to take into account the losses due to the eddy currents effect inside a magnetostrictive layer. In brief, the analytical models have been developed in many physical aspects. In some cases, these models are very practical in calculation of ME behavior. Nevertheless, they are only valid in 1D assumption for simplified canonical forms (laminate rectangular tri-layer or bi-layer).

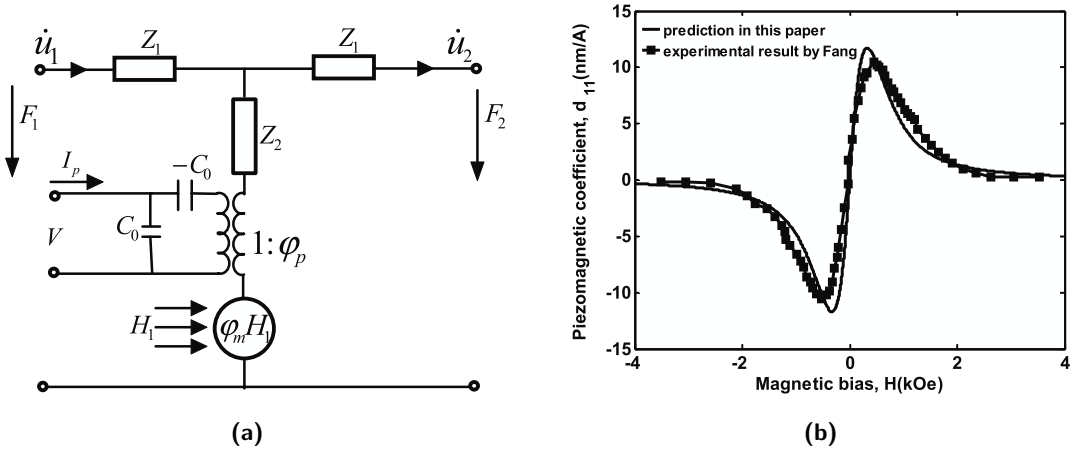

Figure 1.20: The theoretical model developped by zhou [80]. (a) magnetic–mechanical–electric equivalent circuit. (b) analytical results compared with the measurement of piezomagnetic coefficient.

In order to improve the performance of future ME composite (energy transducer or sensors), it is necessary to procure a numerical multiphysics modeling in which all physical coupling phenomena are taken into account, whatever the studied structural forms. At first, a 2D multiphysics code based on the finite element method (FEM) [83], [84], [85], [86], [87], [88], which uses a $\boldsymbol{a}$ - V formulation (mixed magnetic vector potential $\boldsymbol{a}$ – electric scalar potential V) and triangular nodal elements, has been developed as a first approach to investigate rectangular structures. Among the macroscopic numerical methods, the finite element method is one of the methods of discretization adapted to complex geometry problems. In the literature, for each coupling considered (magneto-mechanical or electro-mechanical), the finite element modeling research work already exists.

For piezoelectric materials, the finite element modeling on electric-mechanic behavior has been investigated by several groups. Piefort's work [89] focuses on the modeling of piezo-

electric multilayers in static and dynamic modes. The state variables considered are the deformation and the electric field, and the constitutive laws are assumed to be linear. The variational method was used to obtain the finite element formulation. The code has been applied to a piezoelectric actuator.

For magnetostrictive materials, Azoum's model [91] is a model of magneto-mechanical coupling in static regime. The constitutive laws are non-linear. The total deformation is decomposed into a deformation of mechanical origin and a magnetostriction deformation. Magnetostriction deformation is modeled by a quadratic function of magnetic induction. Following these studies, the Galopin model [92] is a model of magneto-electric coupling in static regime. In order to update the model with relevant magneto-elastic constitutive laws, a platform for the characterization of magnetostrictive materials has been developed. The model was applied on a displacement sensor. The numerical results were compared with the experimental results of [93]. Belahcen [90] proposed to determine constitutive laws from Helmholtz's free energy. This model has been experimentally validated and applied to the calculation of vibrations in electrical machines.

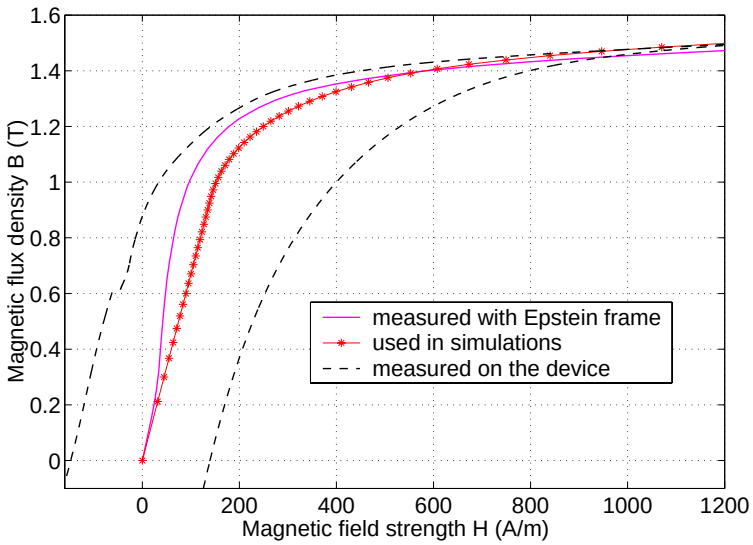

Figure 1.21: Simulation result of magnetostriction behavior by Belahcen

Combination of 2D FEM formulation for piezoelectric and magnetostrictive material, the FEM is developed to investigate the ME effect. In [85], A numerical study of ME composite in dynamic regime is introduced for magnetic sensor application. Multiphysics modeling of ME energy transducer employing FEM was afterward [83], [94], [95]. The piezoelectric behavior is assumed linear, the nonlinear magnetostrictive is considered either using quadratic function of magnetization or Jile-Atherton model [9], [96], [97]. Several important phenomenal physics are taken into account: the non-linearities of the magneto-mechanical couplings, the mechanical frequency effect of the structure, electromagnetic coupling by Maxwell's equations under dynamic excitation. These approaches make it easier to understand the ME sensor/transducer working principle. Although the simulation results have shown good concordances with the measurement ones, the model limits to rectangular structures and cannot consider more complex structures such as trilayer laminar-disks. Moreover, in a 2D model, the influence of the eddy currents in magnetody-

namic regime is approximately addressed since only the normal component of the potential vector $\boldsymbol{a}$ is considered.

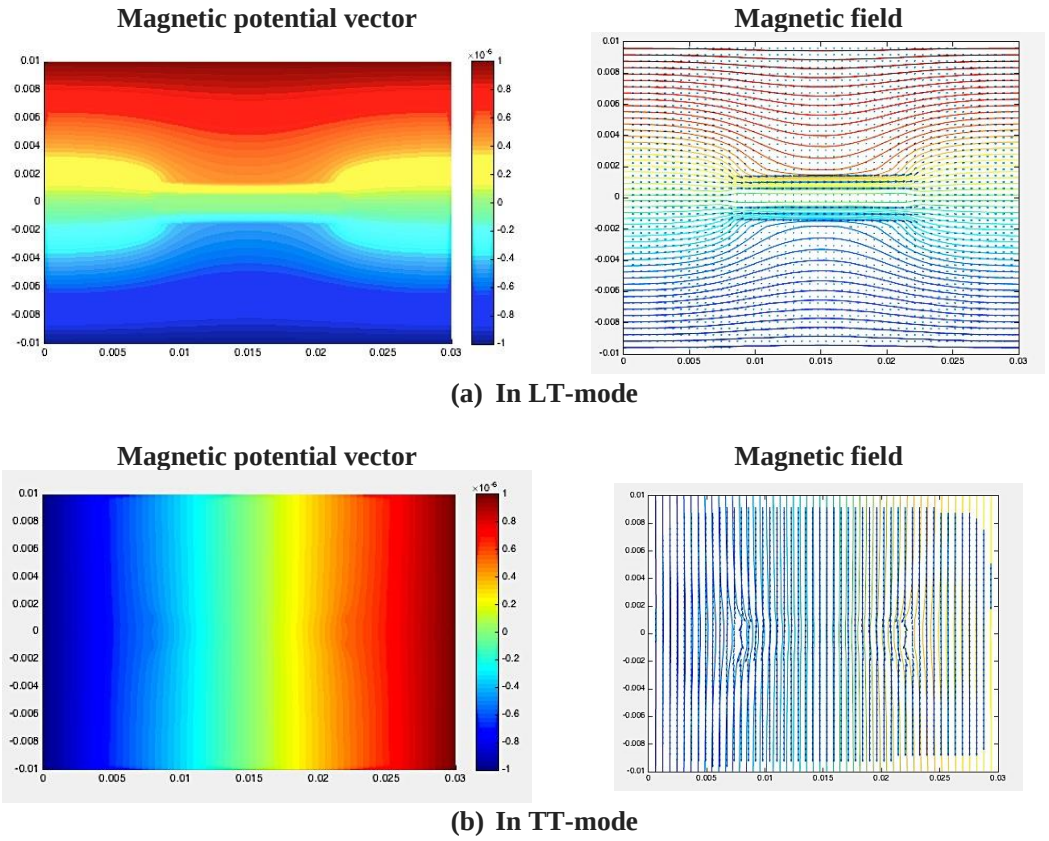

Figure 1.22: Illustration of magnetic field obtained by 2D FEM analysis in [97]

Recently, Spark plasma sintering (SPS) has been reported as an efficient fabrication process of ME composites. The short time and low temperature requirement of SPS make it possible to get the ME response close to the value predicated by the theoretical calculations [98]. The induced magnetic anisotropy in the direction of applied pressure during SPS process enhanced actually the magnetoelectric effect [99]. Employing this fabrication approach, the obtained structure is in cylinder form. For this type of geometry or when the stress is no longer uniform, the 2D FEM can't be applied. In order to investigate different ME structure with more complicated strain and stress state, 3D FE analyses is highly demanded as they are more flexible to model configurations and capable to obtain full field numerical solutions.

Generally, the 3D FE analysis of piezoelectric is introduced in numerous researches and exists in commercial software. The piezoelectric ultrasonic transducer motion is analyzed by ATILA software and experimentally compared in [100]. Braess [101] developed a formulation for thin film material to compute the deformation of structure exited by piezoelectric actuators. In another hand, magnetostrictive models are recently developed. In [102], magnetic and elastic problems are studied individually where different discretization techniques are applied for the mechanical and magnetic fields. This technique requires mesh projection and coupling interaction procedure which demands simulation times. Evans

[103] proposes a strongly coupled magnetostrictive model discretizing mechanical displacement and vector magnetic potential by nodal elements. However, Considering Whitney elements or vector basis functions can be more advantageous [104] and the $\boldsymbol{a}$ - ϕ formulation is proved to be more stable and have better convergence rate, especially in magneto-dynamic problems [105].

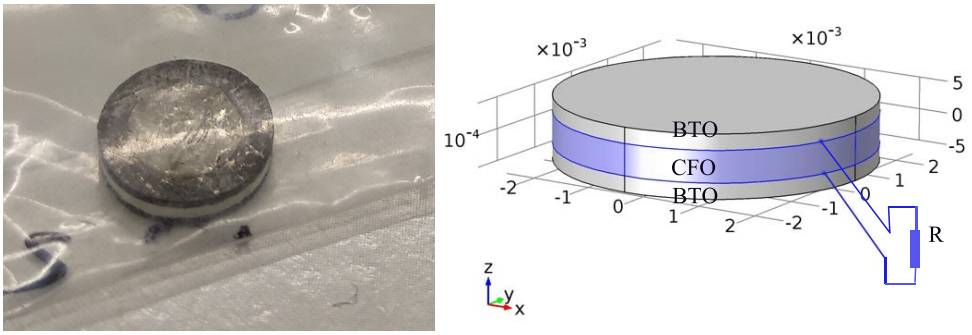

(a) (b)

Figure 1.23: ME laminate composite of circular section which 3D analysis is needed.

In this context, Zhi [106] developed multiphysic framework and constitutive models for piezoelectric and magnetostrictive materials in our laboratory. The 3D FE analysis is based on the equilibrium of electro-magnetic, elastic and thermals field, Whitney elements are employed. Piezoelectric model is applied for piezoelectric bimorph and surface acoustic wave (SAW) [107]. The magnetostrictive model used the $\boldsymbol{a}$ - ϕ formulation for magnetodynamic, implemented the Discrete Energy-Averaged Model (DEAM), modified Armstrong model [64], to describe the nonlinear magnetostrictive response [66], [108].

Finally, based on the formulation developed by Zhi, our objective of the thesis is to build a 3D FE framework to investigate the ME energy transducers. The proposed 3D formulation combines the linear model of the piezoelectric layer introduced in [107] and the non-linear dependence of the magnetic permeability $\boldsymbol{B}(\boldsymbol{H})$ model and mechanical stiffness $\boldsymbol{S}(\boldsymbol{H})$ model of the magnetostrictive layer. For that, the use of a magneto-elastic multi-scale model including hysteresis effect such as the Discrete Energy-Averaged Model (DEAM) [109], [110] or multiscale approach [65] is fundamental. These models extend the energy-weighted averaging class of magnetomechanical models by developing an efficient implementation for magnetic hysteresis due to both the applied magnetic field $\boldsymbol{H}$ and stress $\boldsymbol{T}$. This approach is applied to compute the behavior of ME laminate composite, particulate inclusion, fiber composite for energy harvester application.

1.4 Conclusion

In this chapter, the definition of the ME effect, the magnetostrictive effect, the piezoelectric effect and the principle of ME composite have been introduced, as well as some applications of these effects. The evolution of IoT requires novel technique responding to power demand of the connected objects and electronic devices. The ME composites

have attracted scientific interests by the capability of transforming the magnetic energy to electric energy at room temperature.

So far, numerical approaches have been presented to investigate ME composites mostly by analytical methods or 2D FE based method. The goals of our work are to develop a multiphysic model allowing the 3D FE analysis of ME composite and optimize the ME structure configuration for energy harvester applications.

In next chapter, the 3D FEM analysis of ME composite will be introduced in both static and dynamic regimes. The constitutive laws of magnetic-mechanic-electric coupling and the FE formulations are established.

Chapter 2

3D Finite Elements Modeling of Magnetoelectric Composite

Summary

2.1 Introduction

The objective of this chapter is to present the multiphysic modeling framework of magnetoelectric (ME) composites. Firstly, the magnetoelectric problem is described. The analysis of ME materials in both static and dynamic regimes is proposed. The suggested assumptions are described.

Secondly, the finite element method is introduced. The differential forms (the Whitney forms) approach is used in our study for the discretization of different variables. The linear shape functions associated with the tetrahedral element for node element, edge element, facet element and volume element are reported.

Next, static analysis of ME problem using this FEM framework is considered. The general physical equations, the constitutive laws, the state variable equations, and the FE procedure will be all detailed. To take into account the nonlinear property of magnetostrictive materials, we implement the DEAM into the 3D model.

Finally, the harmonic analysis of ME considering the effect of eddy currents will be presented.

2.2 Description and configuration

During the past years, the L2E laboratory developed a 2D FE multiphysics model that considers simultaneously the magnetic-mechanic-electric coupling [83], [97], [87]. This model can be applied to investigate the performance of laminate composite with rectangular surface for applications in energy transducer.

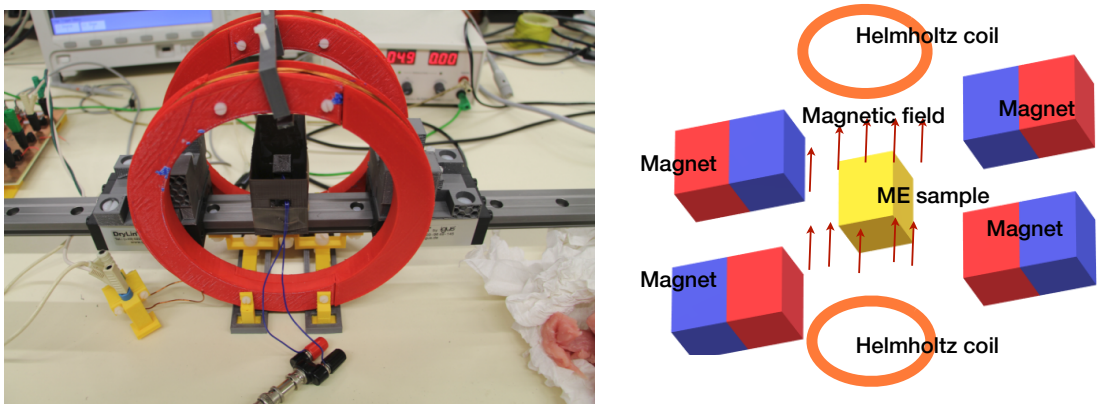

(a) experiment setup **(b)** illustration

Figure 2.1: Measurement of ME coefficient

The experiment of ME measurement considered in the presented work and its illustration are given in Figure 2.1. As mentioned before, to have an optimal magnetoelectric coupling coefficient, the ME materials are excited by a dynamic magnetic field with a static magnetic bias. The ME sample is placed in a magnetic field created by the Helmholtz coil (the dynamic magnetic field) and the magnets (the static magnetic field).

In order to establish a mathematic model, the applied hypothesis are recapitulated as follows:

- The magnetic excitation is uniform.
- The assumption of small displacement is made and the linear strain–displacement relations are assumed.
- The influence of temperature is neglected.
- The piezoelectric coefficients are constants.
- Perfect mechanical contact on magnetotrictive/piezoelectric interface.
- The electric conductivity is constant in magneticstrictive materials and zero in other domains.

2.3 Finite Elements method

For electromagnetic problem, in order to preserve the field continuity properties, the differential forms based elements, called Whitney elements [111], are employed.

2.3.1 Differential forms

In 3D application, four types of entries called k-forms are used. Firstly, a differential 1-form on an open subset of $\mathbb{R}^3$ can be expressed

$$F(x,y,z)dx + G(x,y,z)dy + H(x,y,z)dz \tag{2.1}$$

where F, G, H are defined function in $\mathbb{R}$, (dx, dy, dz) is the basis. This form is integrated over a line, which is suited for the representation of field quantities such as the electric field having tangential continuity.

A 2-form, integrated over a surface, is an expression built using wedge products

$$F(x,y,z)dx \wedge dy + G(x,y,z)dy \wedge dz + H(x,y,z)dz \wedge dx \tag{2.2}$$

The significance of 2-form is continuous in the normal direction, making it suitable for representing flux quantities.

Next, 3-form is integral over a region of space and constant in the volume. It can represent quantities like scalar densities.

$$f(x,y,z)dx \wedge dy \wedge dz \tag{2.3}$$

with $f(x,y,z)$ the $\mathbb{R}$-valued function. Finally, 0-form $f(x,y,z)$ is defined on a point, can be utilized to represent potential variables as it is continuous along all orientations.

So far, we apply derivative operator to k-form in order to obtain (k+1) form

$$\frac{\{0-\text{form}\}}{\text{function}} \xrightarrow{\text{grad}} \frac{\{1-\text{form}\}}{\text{vector field}} \xrightarrow{\text{curl}} \frac{\{2-\text{form}\}}{\text{vector field}} \xrightarrow{\text{div}} \frac{\{3-\text{form}\}}{\text{function}} \tag{2.4}$$

2.3.2 Linear shape function on tetrahedral elements

In our works, the domain is discretized using linear tetrahedrons (Figure 2.2). This element contains 4 nodes (x_1, y_1, z_1), (x_2, y_2, z_2), (x_3, y_3, z_3), (x_4, y_4, z_4), 6 edges $e_1, e_2, e_3, e_4, e_5, e_6$, 4 faces $f^1_{234}, f^2_{134}, f^3_{124}, f^4_{123}$ and 1 volume.

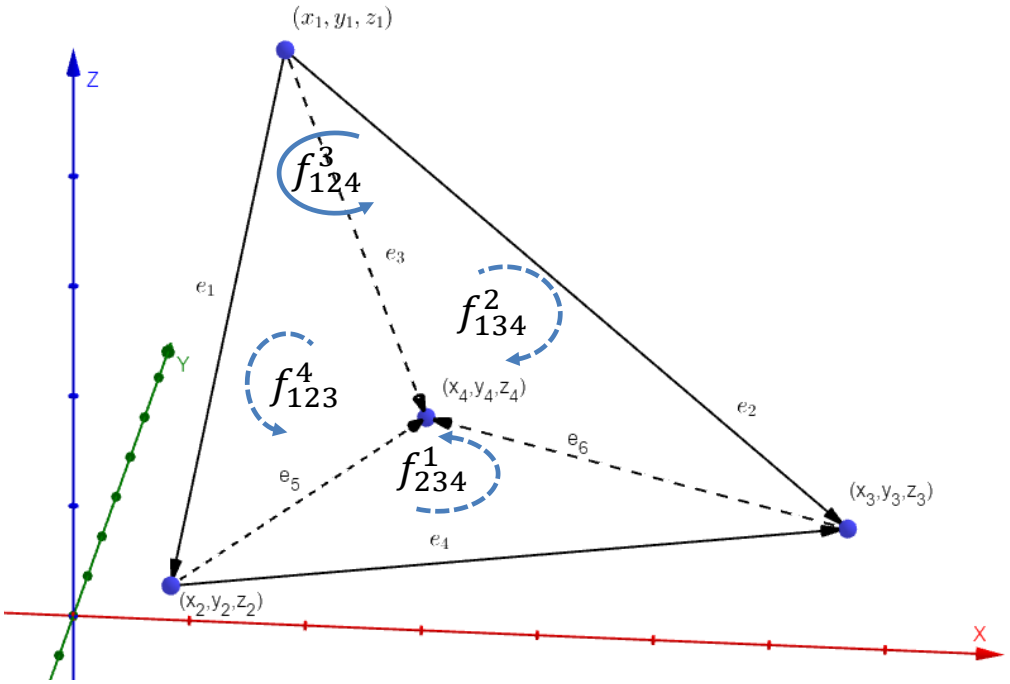

Figure 2.2: Tetrahedral element

For interpolation by node element, the unknown field in the tetrahedron is approximated by linear function

$$f(x, y, z) = a + bx + cy + dz \tag{2.5}$$

Assuming the field values at 4 nodes of the tetrahedral element is f_1, f_2, f_3, f_4, this satisfies

$$\begin{cases} f_1 = a + bx_1 + cy_1 + dz_1 \\ f_2 = a + bx_2 + cy_2 + dz_2 \\ f_3 = a + bx_3 + cy_3 + dz_3 \\ f_4 = a + bx_4 + cy_4 + dz_4 \end{cases} \tag{2.6}$$

Solve equation 2.6 for a, b, c, d, we obtain

$$\begin{cases} f_1 = a_1 + b_1x_1 + c_1y_1 + d_1z_1 \\ f_2 = a_2 + b_2x_2 + c_2y_2 + d_2z_2 \\ f_3 = a_3 + b_3x_3 + c_3y_3 + d_3z_3 \\ f_4 = a_4 + b_4x_4 + c_4y_4 + d_4z_4 \end{cases} \tag{2.7}$$

Now, the equation 2.5 is rewritten

$$f(x,y,z) = (a_1 + b_1x + c_1y + d_1z)f_1 + (a_2 + b_2x + c_2y + d_2z)f_2 + (a_3 + b_3x + c_3y + d_3z)f_3 + (a_4 + b_4x + c_4y + d_4z)f_4 = \sum_{i=1}^{4} \lambda_i f_i \tag{2.8}$$

It is the introduction of the shape function λ_i. Detail formulation of basis function is presented in Appendice.

In general, the Whitney k-form basis function is given by [112]

$$w_{0,\dots,k} = k! \sum_{i=0}^{k} (-1)^i \lambda_i d\lambda_0 \times \cdots \times d\lambda_{i-1} \times \lambda_{i+1} \times \cdots \times d\lambda_k \tag{2.9}$$

If $k = 0$, field values are interpolated by the node element

$$w_i = \lambda_i \tag{2.10}$$

If $k = 1$, field values are interpolated by the edge element, let i and j are the vertices of an edge:

$$w_{ij} = \lambda_i \text{grad}\lambda_j - \lambda_j \text{grad}\lambda_i \tag{2.11}$$

If $k = 2$, field values are interpolated by facet element, let i, j and k are the vertices of a facet:

$$w_{ijk} = 2(\lambda_i \text{grad}\lambda_j \times \text{grad}\lambda_k - \lambda_j \text{grad}\lambda_k \times \text{grad}\lambda_i + \lambda_k \text{grad}\lambda_i \times \text{grad}\lambda_j \tag{2.12}$$

Finally, for $k = 3$, volume shape function w_{ijkl} is constant on tetrahedral and zero elsewhere.

2.4 Static 3D FEM analysis in magnetostatic biasing

2.4.1 Weak formulation

Let us consider a domain $\Omega \in \mathbb{R}^3$ that is composed of the material domain $\Omega_U = \Omega_M \cup \Omega_P$ (magnetostrictive + piezoelectric) and the air domain $\Omega_A = \Omega / \Omega_U$ enveloping Ω_U. The boundary of the domain $d\Omega$ is also boundary of the air domain.

In static regime, the 3D finite element formulation of the MEC coupled problems is derived by combining the elastic equilibrium equation 1.24 with the magnetic and electric equilibrium equations, namely Ampère's and Gauss's laws given by equations 1.30 and 1.28:

$$\begin{cases} \text{div } \boldsymbol{T} + \boldsymbol{f} = 0 \\ \text{curl } \boldsymbol{H} = \boldsymbol{J} \\ \text{div } \boldsymbol{D} = \rho_V \end{cases} \tag{2.13}$$

In our case, $\boldsymbol{J} = 0$ because there is no applied current in the study domain. $\rho_V = 0$ because the piezoelectric layer is considered as a perfect dielectric.

The constitutive relations are the combination of the electro-mechanical constitutive laws 1.7 in the piezoelectric material and the magneto-mechanical constitutive laws 1.12 in the magnetostritive material:

$$\begin{cases} \boldsymbol{T} = c\boldsymbol{S} - e^t\boldsymbol{E} - h^t\boldsymbol{B} \\ \boldsymbol{H} = -h\boldsymbol{S} + \nu^S\boldsymbol{B} \\ \boldsymbol{D} = -e\boldsymbol{S} + \varepsilon^S\boldsymbol{E} \end{cases} \tag{2.14}$$

Substituting 2.14 into 2.13 leads to system equation

$$\begin{cases} \text{div } (\boldsymbol{cS} - \boldsymbol{e^tE} - \boldsymbol{h^tB}) + \boldsymbol{f} = 0 \\ \text{curl } (-h\boldsymbol{S} + \nu^S\boldsymbol{B}) = 0 \\ \text{div } (-e\boldsymbol{S} + \varepsilon^S\boldsymbol{E}) = 0 \end{cases} \tag{2.15}$$

The fields $\boldsymbol{S}$, $\boldsymbol{E}$ and $\boldsymbol{B}$ can be expressed, respectively, by the state variables: the mechanical displacement $\boldsymbol{u}$ (m), the electric scalar potential V (V) and the magnetic vector potential $\boldsymbol{a}$ (Wb/m) equation 1.4, 1.27, 1.32.

$$\begin{cases} \boldsymbol{S} = \mathfrak{D}\boldsymbol{u} \\ \boldsymbol{B} = \text{curl } \boldsymbol{a} \\ \boldsymbol{E} = -\text{grad } V \end{cases} \tag{2.16}$$

The system equation of the coupled problem is obtained by substituting 2.16 into 2.15. Next, the variational principle is applied in considering corresponding boundary conditions of the problem domain Ω which leads to the following finite element formulation:

$$\begin{cases} \int_\Omega \mathfrak{D}\boldsymbol{u}'(c\mathfrak{D}\boldsymbol{u} + e^t\text{grad } V - h^t\text{curl } \boldsymbol{a})d\Omega = \int_\Omega \boldsymbol{u}'\boldsymbol{f}d\Omega \\ \int_\Omega \text{curl } \boldsymbol{a}'(-h\mathfrak{D}\boldsymbol{u} + \nu\text{curl } \boldsymbol{a})d\Omega = 0 \\ \int_\Omega \text{grad } V'.(e\mathfrak{D}\boldsymbol{u} - \varepsilon^S\text{grad } V)d\Omega = 0 \end{cases} \tag{2.17}$$

where $\boldsymbol{u}', \boldsymbol{a}', V'$ are the test function.

2.4.2 Finite element discretization

The finite element discretization is realized by using the Galerkin approach. The nodal elements and the edge elements are respectively employed for the approximation of $\boldsymbol{u}, V$ and $\boldsymbol{a}$. We use $\boldsymbol{u}_h$, V_h and $\boldsymbol{a}_h$ representing these quantities in element h of the domain,

such that $\boldsymbol{u}_h = w^n \boldsymbol{u}_h^k, V_h = w^n V_h^k$ and $\boldsymbol{a}_h = \boldsymbol{w}^e \boldsymbol{a}_h^k$; where w^n and $\boldsymbol{w}^e$ are respectively, the nodal and edge basis functions and $\boldsymbol{u}_h^k$, V_h^k and $\boldsymbol{a}_h^k$ are the nodal and edge degrees of freedom of the element h. The use of edge elements for the vector potential $\boldsymbol{a}$ guarantees naturally its tangential continuity.

The basis function is chosen for the test functions, solving for one element h, the equation 2.17 becomes

$$\begin{cases} (\int_\Omega \mathfrak{D} w^n c \mathfrak{D} w^n d\Omega)\boldsymbol{u}_h^k + (\int_\Omega \mathfrak{D} w^n e^t \text{grad } w^n d\Omega) V_h^k \\ \qquad\qquad -(\int_\Omega \mathfrak{D} w^n h^t \text{curl } \boldsymbol{w}^e d\Omega)\boldsymbol{a}_h^k = \int_\Omega w^n \boldsymbol{f} d\Omega \\ -(\int_\Omega \text{curl } \boldsymbol{w}^e h \mathfrak{D} w^n d\Omega)\boldsymbol{u}_h^k + (\int_\Omega \text{curl } \boldsymbol{w}^e \nu^s \text{curl } \boldsymbol{w}^e d\Omega)\boldsymbol{a}_h^k = 0 \\ -(\int_\Omega \text{grad } w^n e \mathfrak{D} w^n d\Omega)\boldsymbol{u}_h^k + (\int_\Omega \text{grad } w^n \varepsilon^s \text{grad } w^n d\Omega)\boldsymbol{a}_h^k = 0 \end{cases}$$

This involves the differentials of the shape functions.

$$\boldsymbol{B}_u = \mathfrak{D} w^n = [\boldsymbol{B}_u^1 \ \boldsymbol{B}_u^2 \ \boldsymbol{B}_u^3 \ \boldsymbol{B}_u^4]$$

with

$$\boldsymbol{B}_u^i = \begin{bmatrix} \partial/\partial x & 0 & 0 \\ 0 & \partial/\partial y & 0 \\ 0 & 0 & \partial/\partial z \\ \partial/\partial x & \partial/\partial y & 0 \\ 0 & \partial/\partial y & \partial/\partial z \\ \partial/\partial x & 0 & \partial/\partial z \end{bmatrix} w_i^n$$

and

$$\boldsymbol{B}_V = \text{grad } w^n = \begin{bmatrix} \partial w_1^n/\partial x & \partial w_2^n/\partial x & \partial w_3^n/\partial x & \partial w_4^n/\partial x \\ \partial w_1^n/\partial y & \partial w_2^n/\partial y & \partial w_3^n/\partial y & \partial w_4^n/\partial y \\ \partial w_1^n/\partial z & \partial w_2^n/\partial z & \partial w_3^n/\partial z & \partial w_4^n/\partial z \end{bmatrix}$$

The term curl $\boldsymbol{w}^e$ can be written as curl $\boldsymbol{w}^e = \boldsymbol{w}^f \boldsymbol{C}$, where $\boldsymbol{w}^f$ is the facet basis functions from 2.4, and $\boldsymbol{C}$ the incident matrix associated with the curl operator [111].

Set

$$\boldsymbol{K}_{uu} = \int_\Omega \boldsymbol{B}_u^t c \boldsymbol{B}_u d\Omega \qquad F_u = \int_\Omega w^n \boldsymbol{f} d\Omega \text{ and } \quad F_a = \int_\Omega w^e \boldsymbol{J} d\Omega$$

$$\boldsymbol{K}_{au} = \boldsymbol{C}^t(\int_\Omega \boldsymbol{w}_\alpha^f h \boldsymbol{B}_u d\Omega) \qquad \boldsymbol{K}_{uv} = \int_\Omega \boldsymbol{B}_u^t e^t \boldsymbol{B}_V d\Omega$$

$$\boldsymbol{K}_{aa} = \boldsymbol{C}^t(\int_\Omega \boldsymbol{w}_\alpha^{f,t} \nu^s \boldsymbol{w}_\alpha^f d\Omega)\boldsymbol{C} \qquad \boldsymbol{K}_{vv} = \int_\Omega \boldsymbol{B}_V^t \varepsilon^s \boldsymbol{B}_V d\Omega$$

The global matrix system is obtained from the discretization of equation 2.17

$$\begin{cases} \boldsymbol{K}_{uu}\boldsymbol{u}_k - \boldsymbol{K}_{au}^t\boldsymbol{a}_k + \boldsymbol{K}_{uv}V_k = F_u \\ -\boldsymbol{K}_{au}\boldsymbol{u}_k + \boldsymbol{K}_{aa}\boldsymbol{a}_k = 0 \\ \boldsymbol{K}_{uv}^t\boldsymbol{u}_k - \boldsymbol{K}_{vv}V_k = 0 \end{cases} \tag{2.18}$$

In our study, no external body force is considered, i.e. $F_u = 0$.

For the magnetic problem, the magnetic excitation is implemented in considering a non-homogenous Dirichlet condition of the magnetic vector potential a_k on the boundary of the problem domain Ω. By this, we assign zero to all a_k on the boundary surface, except for those crossing a randomly built path constituted of one layer of surface elements, so that a_i, the line integral of $\boldsymbol{a}$ on ith edge across this path, equals to the applied magnetic flux crossing the study domain (see Figure 2.3). In this case, the right hand side can be written as $F_a = \boldsymbol{K}_{aa}a_p$. The index p denotes the set of edges across the one-layer elements path.

2.4.3 Boundary conditions

Let take an example of a ME composite, the solution domain is a cylinder introduced in Figure 2.3a, wrapped by the air boundary. The applied magnetics flux is assumed to be uniform in the domain.

Mechanical condition

Usually, the composite material is fixed in the magnetic field created by Helmholtz coil (Figure 2.1) by two fixed point at the center of top face and bottom face of the ME composite. With this configuration, the material can be freely deformed. In the model, we introduce these points as in the Figure 2.3a (orange color), and its Dirichlet boundary condition is used:

$$\boldsymbol{u} = 0$$

Magnetic condition

Suppose that we want to apply magnetic flux in x direction $\bar{B}_x$. Consider a surface S and its boundary L in the Figure 2.3b, By Stokes' theorem, the magnetix flux through the surface S is measured by

$$\Phi_B = \iint_S BdS = \oint_{L(S)} \boldsymbol{a}dl$$

Therefore, one way to apply magnetic flux is building a set of edge elements a_k at the air boundary surface (in red of Figure 2.3a). This set must create a line from the left end to the right end of the domain. The value of magnetic potential for these edge elements is

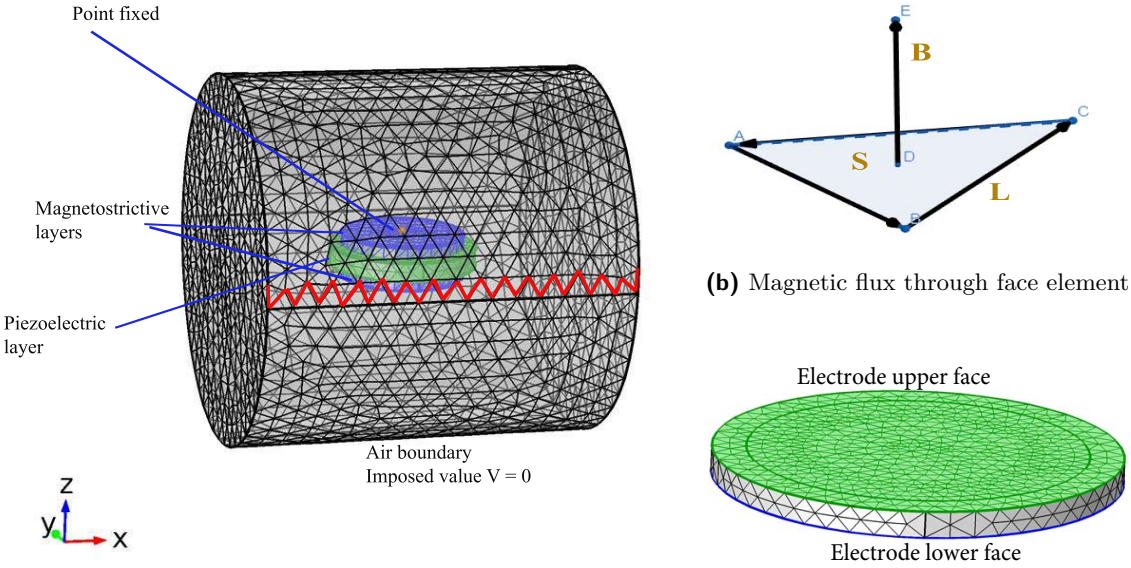

(a) The domain considered

(b) Magnetic flux through face element

(c) The piezoelectric layer

Figure 2.3: Boundary conditions

$$a_k = \bar{B}_x S_0$$

where S_0 is the cross section surface of the cylinder. The magnetic potential of other edges on the boundary surface are null.

Electrical condition

In order to represent the electrodes on the upper face and lower face of the piezoelectric layer, the value of electric potential at node element on the electrode (Figure 2.3c) must be the same. To guarantee the solution of the electric potential, the Dirichlet condition $V = 0$ is applied on the air boundary of the solution domain.

2.4.4 Matrix equation

The equation 2.18 can be finally written in the following matrix form:

$$[\boldsymbol{K}]\{X\} = [F] \tag{2.19}$$

where

$$[\boldsymbol{K}] = \begin{bmatrix} \boldsymbol{K}_{uu} & -\boldsymbol{K}_{au}^t & \boldsymbol{K}_{uv} \\ -\boldsymbol{K}_{au} & \boldsymbol{K}_{aa} & 0 \\ \boldsymbol{K}_{uv}^t & 0 & -\boldsymbol{K}_{vv} \end{bmatrix}$$

and $\{X\} = \{\boldsymbol{u}\ \boldsymbol{a}\ V\}^t$. The values of F_a are determined by the static magnetic bias $\boldsymbol{H}_{dc}$.

In the magnetoelectric problem, the magnetostrictive coefficient must be determined firstly at bias-point (Figure 2.4) combining the nonlinear magnetostrictive analysis (nonlinear static piecewise procedure) and the static ME analysis to compute the state variables. After that, the performance of ME composite under dynamic magnetic field will be studied by the harmonic analysis.

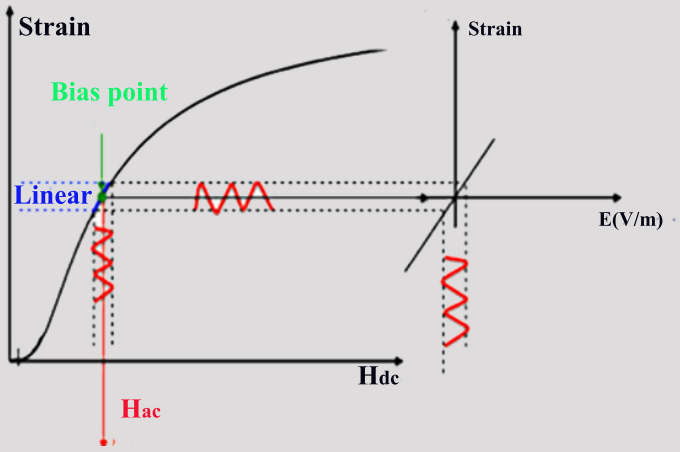

Figure 2.4: Bias-point in magnetoelectric analysis

2.5 Nonlinear magnetostrictive analysis

2.5.1 The multiscale model

For a given magnetic bias, because of the nonlinearity, the magnetostrictive material properties at a given location are determined by the state variables on that location. As the stress and the magnetic field are different from one location to the other, the material constants vary spatially (non-homogeneity) and depend on the applied static field. As a result, in the calculation of magnetoelectric response, the consideration of the material non-homogeneity and nonlinearity is necessary. The calculation of the nonlinear magnetostrictive coefficients involves a recursive algorithm: material coefficient constants are solved on the microscopic structure using the DEAM model (presented in section 1.3.1) which needs the state variable; while the state variables can be computed after solving FEM equations using material constants.

In Figure 2.5 we describe the variations of the magnetization and the magnetostriction as respectively function of the mechanical and magnetic bias conditions. These results are obtained using our implementation and in concordance with [113].

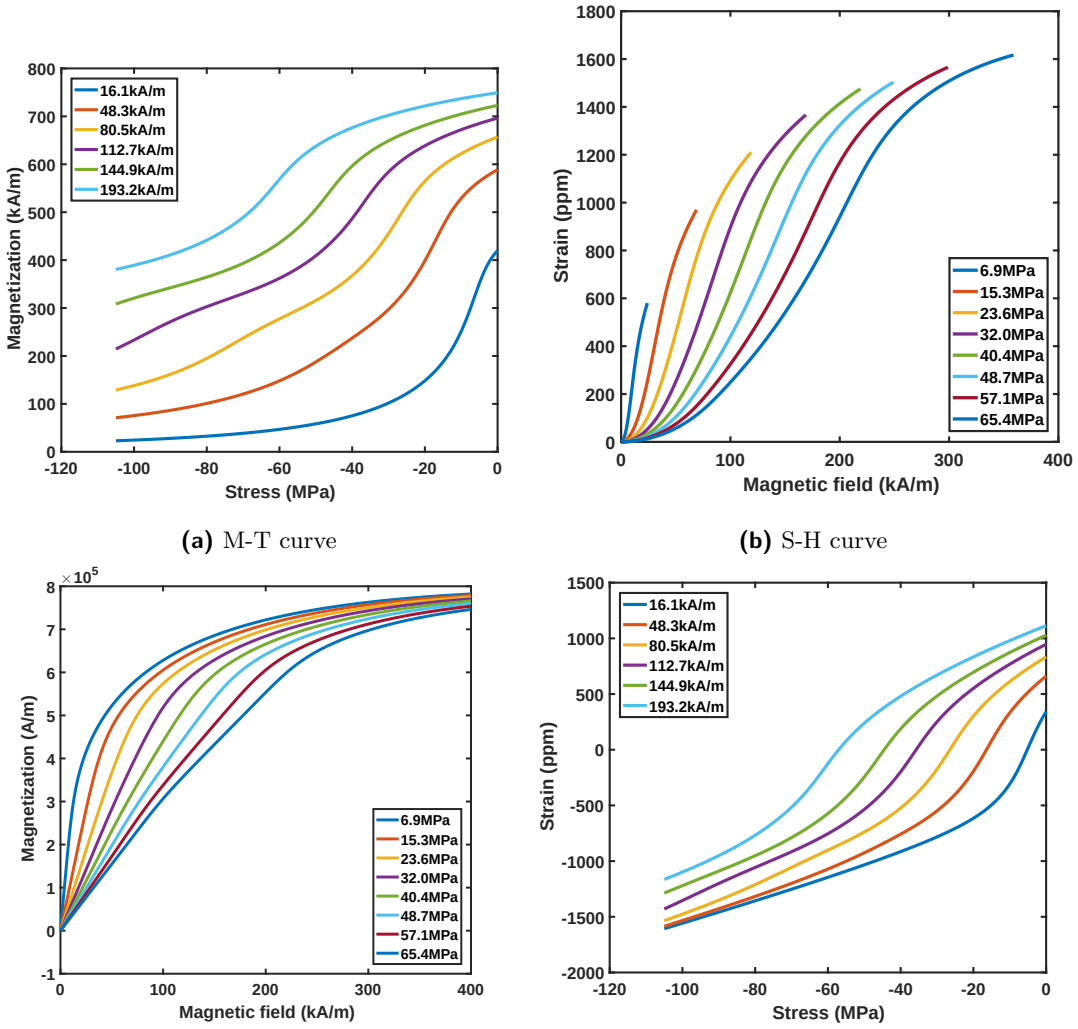

(a) M-T curve

(b) S-H curve

(c) M-H curve

(d) S-T curve

Figure 2.5: Simulation results of Terfenol-D using data of reference

2.5.2 The nonlinear static piecewise procedure

After the implementation of the multi-scale model, the state variables are computed using the macroscopic laws determined by 1.16 in solving the matrix system 2.19 with a piecewise linear procedure.

The process of piecewise linear solution is presented in Figure 2.6 and summarized as follows. First, the DEAM model is used to evaluate the coefficients of the magnetostrictive material through the Jacobian matrix ζ under initially set of bias points $(\boldsymbol{H}_0, \boldsymbol{T}_0)$.

$$\zeta = \begin{bmatrix} \mu^S = \dfrac{\partial \boldsymbol{B}}{\partial \boldsymbol{H}}(\boldsymbol{H}_0, \boldsymbol{T}_0) & d = \dfrac{\partial \boldsymbol{B}}{\partial \boldsymbol{T}}(\boldsymbol{H}_0, \boldsymbol{T}_0) \\ d^t = \dfrac{\partial \boldsymbol{S}}{\partial \boldsymbol{H}}(\boldsymbol{H}_0, \boldsymbol{T}_0) & s^H = \dfrac{\partial \boldsymbol{S}}{\partial \boldsymbol{T}}(\boldsymbol{H}_0, \boldsymbol{T}_0) \end{bmatrix} \tag{2.20}$$

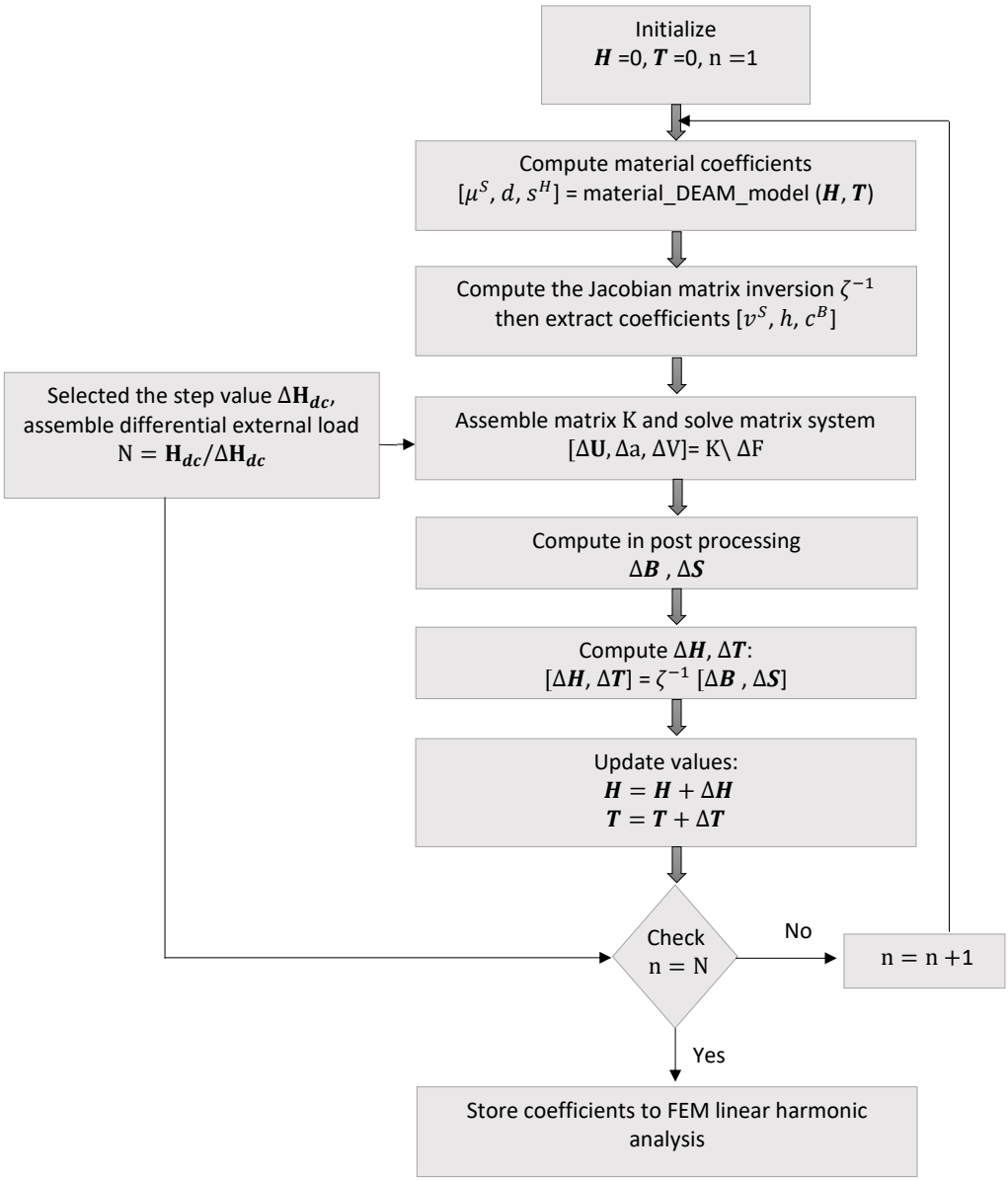

Figure 2.6: Flowchart of piecewise linear solution process to compute the magnetostrictive coefficient for simulation of magnetoelectric material

Second, the inversion of the Jacobian matrix given by 2.21 is used to extract the incremental coefficients μ^S, h, c^B. In this way, the values of the incremental solutions $\Delta\boldsymbol{B}$ and $\Delta\boldsymbol{S}$ prevailing inside the MEC are extracted after computing the global matrix system 2.19. The submatrices $\boldsymbol{K}_{xx}$ takes the same forms as the previous section. The values of the incremental set bias points ($\Delta\boldsymbol{H}$, $\Delta\boldsymbol{T}$) inside the MEC are then computed through the constitutive laws given by 2.22. This procedure can preserve the spatial inhomogeneity in the distribution of the field and stress in the magnetostrictive material.

$$\zeta^{-1} = \begin{bmatrix} \nu^S & -h \\ -h^t & c^B \end{bmatrix} \tag{2.21}$$

$$\begin{bmatrix} \Delta \boldsymbol{H} \\ \Delta \boldsymbol{T} \end{bmatrix} = \zeta^{-1} \begin{bmatrix} \Delta \boldsymbol{B} \\ \Delta \boldsymbol{S} \end{bmatrix} \tag{2.22}$$

2.6 Linear harmonic magnetoelectric analysis

In the previous section, the solution of the static nonlinear problem has been presented. It allows the determination of incremental material constants for a given magnetostatic bias. To model the dynamic behavior of the MEC, the small signal assumption is made. The dynamic field oscillates around the static bias field. The incremental material coefficients are considered as constants. The linear harmonic magnetoelectric analysis is used to investigate the performance of laminate composites.

2.6.1 Magnetostrictive material in dynamic regime

Under dynamic excitation, since the magnetostrictive material is conductive, it is essential to consider the non-vanishing electric conductivity, the effect of eddy currents. we formulate the magnetostrictive problem taking into account the eddy current in equation 2.23 and 2.24

$$\begin{cases} \text{div } \boldsymbol{T} + \boldsymbol{f} = \rho_m \dfrac{d^2 \boldsymbol{u}}{dt^2} \\ \text{curl } \boldsymbol{H} = \boldsymbol{J}_s + \boldsymbol{J}_c \\ \text{div } \boldsymbol{J}_c = 0 \end{cases} \tag{2.23}$$

$$\begin{cases} \boldsymbol{T} = c\boldsymbol{S} - h^t \boldsymbol{B} \\ \boldsymbol{H} = -h\boldsymbol{S} + \nu \boldsymbol{B} \\ \boldsymbol{J}_c = \sigma_c \boldsymbol{E} \end{cases} \tag{2.24}$$

where ρ_m (kg/m^3) is the mass density of the medium, , $\boldsymbol{J}_s = 0$ in our case, and $\boldsymbol{J}_c = \sigma_c \boldsymbol{E}$ (A/m^2) is the eddy current density with σ_c (S/m) the conductivity which is nonzero in magnetostrictive domain and vanishes in others, $\frac{d^2}{dt^2}$ denotes the two time derivative operator. The mechanical displacement $\boldsymbol{u}$, the magnetic vector potential $\boldsymbol{a}$ and a scalar potential ψ (which is the time primitive of the aforementioned electric potential V used for the symmetry purpose) are introduced as the state variables:

$$\begin{cases} \boldsymbol{S} = \mathfrak{D}\boldsymbol{u} \\ \boldsymbol{B} = \text{curl } \boldsymbol{a} \\ \boldsymbol{E} = -\dfrac{d(\boldsymbol{a} + \text{grad}\psi)}{dt} \end{cases} \tag{2.25}$$

Appling 2.25 and 2.24 into 2.23 the variation formula take

$$\begin{cases} \displaystyle\int_\Omega \mathfrak{D}\boldsymbol{u}'(c\mathfrak{D}\boldsymbol{u} - h^t\text{curl } \boldsymbol{a})d\Omega + \int_\Omega \boldsymbol{u}'\rho_m \frac{d^2\boldsymbol{u}}{dt^2}d\Omega = \int_\Omega \boldsymbol{u}'\boldsymbol{f}d\Omega \\ \displaystyle\int_\Omega [\text{curl } \boldsymbol{a}'(-h\mathfrak{D}\boldsymbol{u} + \nu\text{curl } \boldsymbol{a}) + \sigma_c\boldsymbol{a}'.(\frac{d\boldsymbol{a}}{dt} + \text{grad}\frac{d\psi}{dt})]d\Omega = 0 \\ \displaystyle\int_\Omega \sigma_c\text{grad}\psi'.(\frac{d\boldsymbol{a}}{dt} + \text{grad}\frac{d\psi}{dt})d\Omega = 0 \end{cases} \tag{2.26}$$

The same finite element discretization procedure is employed, note that grad $w^n = w^e\boldsymbol{G}$, the submatrices $\boldsymbol{K}_{xx}$ takes the same forms as the previous section, while

The submatrices K_{xx} takes the same forms as the previous section, while
$\boldsymbol{M}_{uu} = \int_\Omega^e (w^n)^t\rho_m w^n d\Omega$, $\boldsymbol{C}_{aa} = \int_\Omega^e (w^e)^t\sigma_c w^n d\Omega$,
$\boldsymbol{C}_{a\psi} = (\int_\Omega^e (w^e)^t\sigma_c w^n d\Omega)\boldsymbol{G}$, $\boldsymbol{C}_{\psi\psi} = \boldsymbol{G}^t(\int_\Omega^e (w^e)^t\sigma_c w^n d\Omega)\boldsymbol{G}$,

We obtain the global system equation

$$\begin{cases} \boldsymbol{M}_{uu}\dfrac{d^2\boldsymbol{u}_k}{dt^2} + \boldsymbol{K}_{uu}\boldsymbol{u}_k - \boldsymbol{K}_{au}^t\boldsymbol{a}_k = \boldsymbol{F}_u \\ -\boldsymbol{K}_{au}\boldsymbol{u}_k + \boldsymbol{K}_{aa}\boldsymbol{a}_k + \boldsymbol{C}_{aa}\dfrac{d\boldsymbol{a}_k}{dt} + \boldsymbol{C}_{a\psi}^t\dfrac{d\psi_k}{dt} = \boldsymbol{F}_a \\ \boldsymbol{C}_{a\psi}\dfrac{d\boldsymbol{a}_k}{dt} + \boldsymbol{C}_{\psi\psi}\dfrac{d\psi_k}{dt} = 0 \end{cases} \tag{2.27}$$

where $\boldsymbol{G}$ is the incident matrix associated with the gradient operator [111]. Same as the previous section, $F_u = 0$ because no external body force exists in our case and the magnetic excitation is considered trough the line integrals of $\boldsymbol{a}$ along the edges of a randomly built path on the boundary surface, which leads to F_a.

2.6.2 Piezoelectric layer in dynamic regime

The governing equations describing piezoelectricity are the elastic equilibrium and electrostatic (for a perfect dielectric i.e. no free charges) equations 2.28. The elastic-electrical coupled behavior laws are given in equation 2.29

$$\begin{cases} \text{div } \boldsymbol{T} + \boldsymbol{f} = \rho_m\dfrac{d^2\boldsymbol{u}}{dt^2} \\ \text{div } \boldsymbol{D} = 0 \end{cases} \tag{2.28}$$

$$\begin{cases} \boldsymbol{T} = c\boldsymbol{S} - e^t\boldsymbol{E} \\ \boldsymbol{D} = \varepsilon\boldsymbol{E} + e\boldsymbol{S} \end{cases} \tag{2.29}$$

To be coherent with the formulation of the previous magnetostriction, the time primitive ψ of the scalar electric potential V is introduced:

$$\begin{cases} \boldsymbol{S} = \mathfrak{D}\boldsymbol{u} \\ \boldsymbol{E} = -\operatorname{grad}\dfrac{d\psi}{dt} \end{cases} \tag{2.30}$$

In order to preserve the symmetry of the system, the Gaussian law is modified by taking its derivative with respect to time.

$$\frac{d(\operatorname{div}\boldsymbol{D})}{dt} = 0 \tag{2.31}$$

The weak formulation and the matrix system for piezoelectric material are as follows:

$$\begin{cases} \displaystyle\int_\Omega \mathfrak{D}\boldsymbol{u}'(c\mathfrak{D}\boldsymbol{u} + e^t\operatorname{grad}\frac{d\psi}{dt})d\Omega + \int_\Omega \boldsymbol{u}'\rho_m\frac{d^2\boldsymbol{u}}{dt^2}d\Omega = \int_\Omega \boldsymbol{u}'\boldsymbol{f}d\Omega \\ \displaystyle\int_\Omega \operatorname{grad}\psi'(e\mathfrak{D}\boldsymbol{u}' - \varepsilon\operatorname{grad}\frac{d^2\psi}{dt^2})d\Omega = 0 \end{cases} \tag{2.32}$$

$$\begin{cases} \boldsymbol{M}_{uu}\dfrac{d^2\boldsymbol{u}_k}{dt^2} + \boldsymbol{K}_{uu}\boldsymbol{u}_k + \boldsymbol{K}^t_{u\psi}\dfrac{d\psi_k}{dt} = \boldsymbol{F}_u \\ \boldsymbol{K}_{u\psi}\dfrac{d\boldsymbol{u}_k}{dt} - \boldsymbol{K}_{\psi\psi}\dfrac{d^2\psi_k}{dt^2} = 0 \end{cases} \tag{2.33}$$

2.6.3 Magnetoelectric in dynamic regime

The overall system for a magnetoelectric composite from the previous systems is therefore the following:

$$\begin{cases} \boldsymbol{M}_{uu}\dfrac{d^2\boldsymbol{u}_k}{dt^2} + \boldsymbol{K}_{uu}\boldsymbol{u}_k - \boldsymbol{K}^t_{au}\boldsymbol{a}_k + \boldsymbol{K}^t_{u\psi}\dfrac{d\psi_k}{dt} = 0 \\ -\boldsymbol{K}_{au}\boldsymbol{u}_k + \boldsymbol{K}_{aa}\boldsymbol{a}_k + \boldsymbol{C}_{aa}\dfrac{d\boldsymbol{a}_k}{dt} + \boldsymbol{C}^t_{a\psi}\dfrac{d\psi_k}{dt} = \Sigma_i\bar{\boldsymbol{a}}_i \\ \boldsymbol{K}_{u\psi}\dfrac{d\boldsymbol{u}_k}{dt} + \boldsymbol{C}_{a\psi}\dfrac{d\boldsymbol{a}_k}{dt} + \boldsymbol{C}_{\psi\psi}\dfrac{d\psi_k}{dt} - \boldsymbol{K}_{\psi\psi}\dfrac{d^2\psi_k}{dt^2} = 0 \end{cases} \tag{2.34}$$

To complete this equation system, it is necessary to add an supplementary equation to take into account the effects of an impedance load Z connected between the electrodes (top and bottom) of the piezoelectric layer. This impedance represents symbolically the input impedance of an electronic device. For this, the electrical charge Q across the electrodes becomes an additional unknown to be added to the resolution system. The additional equation is then given by the following Ohm's law [83]:

$$U(t)\boldsymbol{K}_{\psi q} - Z\frac{\partial(Q)}{\partial t} = 0 \tag{2.35}$$

where $U(t) = \bar{V}(t)$ is the output voltage across the impedance Z and $\boldsymbol{K}_{\psi q}$ is an incident vector in which the elements are respectively equal to 1 or -1 depending on whether the related node is associated to the top electrode or the bottom one, otherwise they take 0.

The final system for harmonic regime $\frac{d}{dt} \rightarrow i\omega$ is as follows

$$[\boldsymbol{K}]\{X\} = [F] \tag{2.36}$$

with $\{X\} = \{\mathbf{u},\ \mathbf{a},\ \psi,\ \mathbf{Q}\}^t$, $[F] = \{0,\ \Sigma_i \bar{a}_i,\ 0,\ 0\}^t$ and

$$[\boldsymbol{K}] = \begin{bmatrix} -\omega^2\boldsymbol{M}_{uu} + i\omega\boldsymbol{C}_{uu} + \boldsymbol{K}_{uu} & -\boldsymbol{K}_{au}^t & i\omega\boldsymbol{K}_{u\psi} & 0 \\ -\boldsymbol{K}_{au} & i\omega\boldsymbol{C}_{aa} + \boldsymbol{K}_{aa} & i\omega\boldsymbol{C}_{a\psi} & 0 \\ i\omega\boldsymbol{K}_{u\psi}^t & i\omega\boldsymbol{C}_{a\psi}^t & i\omega\boldsymbol{C}_{\psi\psi} + \omega^2\boldsymbol{K}_{\psi\psi} & -\boldsymbol{K}_{\psi q} \\ 0 & 0 & -\boldsymbol{K}_{\psi q}^t & i\omega Z \end{bmatrix}$$

where $\boldsymbol{C}_{uu} = \alpha\boldsymbol{M}_{uu} + \beta\boldsymbol{M}_{uu}$ is the mechanical damping matrix established by the Rayleigh coefficients. The parameters β and α depend on the energy dissipation characteristic of the structure. Damping values for materials are not provided by manufacturers. These parameters are determined by combining experimental and numerical techniques through the quality factor (Q_m) by measuring the admittance curves which are influenced by damping [114].

2.7 Conclusion

In this chapter, the equations of mechanic equilibrium and electromagnetic have been introduced both in static regime and dynamic regime. The constitutive laws of magnetic-mechanic-electric coupling have been presented, as well as the magnetostrictive and piezoelectric constitutive laws. The 3D finite element formulation is developed to study the responses of ME materials. The nonlinear response of magnetostrictive have been also considered. The multiscale DEAM model is implemented in the 3D FE model to taking into account the nonlinear behavior of magnetostrictive material.

In the next chapter, we apply the 3D model to investigate the performant of the most popular ME composite structure, the laminate composite. By using 3D model, different laminate structures can be examined, the influence of the geometry parameter will also be considered.

Chapter 3

Study of magnetoelectric laminate composites

Summary

3.1 Introduction

In this chapter, the multiphysics model, will be applied to investigate the behavior of some magnetoelectric laminated composites. The simulation results are compared with the measurements available in our laboratory or in the literature for validation.

Firstly, a laminate composite with the circular section is examined. The geometry and the boundary conditions are respectively described. The nonlinear static analysis is considered to determine the material coefficients of the magnetostrictive layer for dynamic regime. When all the coefficients are obtained, the linear harmonic analysis is performed.

Secondly, we study a conventional laminate structure with the rectangular section, following the same procedure as the previous case of the laminate structure with the circular section.

Finally, some modifications of the structure are considered. A study on the influence of the geometry parameters to the performance of ME composite is conducted. From this, a novel structure can be suggested in order to improve the ME properties.

3.2 Introduction of ME laminate composites

The laminated ME composites are very promising ME materials. For this type of structure, the composite can have much better ME coupling, larger ME anisotropy and higher resonance response in a wide frequency range [6], [26], [27]. Spark plasma sintering (SPS) is a widely used method for fabrication of the magnetoelectric materials. This method allows rapid consolidation to obtain ME ceramic composites with high density and purity. The laminate composite with circular section is investigated experimentally in [115]. The structure consisting of Galfenol and PZT is applied as magnetic sensor in [116] which can operate in wide temperature range. In [117] a cellulose-based magnetoelectric composite is investigated. In this chapter, we use the 3D model presented in the first chapter to study the response of a circular section ME composite. The simulation results are compared with the measurement in [115]. Next, the model is applied to simulate the behavior of different laminate structures.

3.3 ME laminate composite with circular section

Firstly, the 3D FEM is applied for ME laminate with its layer in disc form. Simulation results are compared with the measurement in [115], where the FeGa magnetostrictive alloy is grown by Bridgman method whereas the piezoelectric layer is $BaTiO_3$.

3.3.1 Geometry and boundary condition

This section presents the simulation results of two tri-laminated MEC disks made of FeGa/$BaTiO_3$/FeGa under the TT and LT modes, respectively, as shown in Figure 3.1. In TT mode, the piezoelectric layer and the magnetostrictive layers are respectively, poled and magnetized along their thickness (transverse geometry). In LT mode, the magnetostrictive layers are magnetized along longitudinal direction. The MEC is connected to an electrical charge Z considered as a purely electrical resistive load R. The materials properties are given in Appendix B.1.

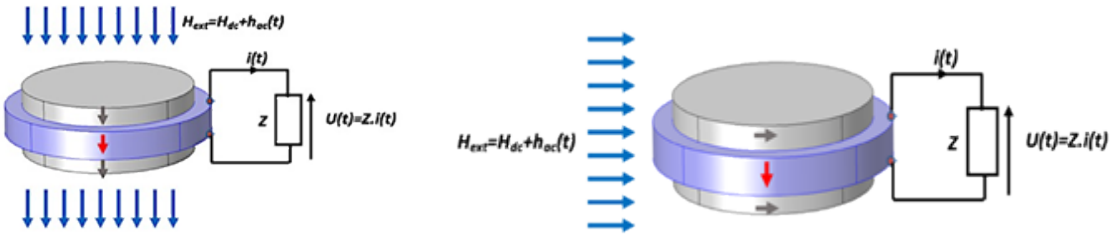

(a) TT mode **(b)** LT mode

Figure 3.1: MEC disks in TT and LT modes connected to a resistance load.
$BaTiO_3$ (grey layer) : thickness 1.5mm, Φ12mm;
FeGa (lavender layers) : thickness 1mm, Φ10mm.

As shown in Figure 3.2, the composite is fixed by two points on the outer surfaces of magnetostrictive layers (the center of the circle marked in yellow). For the piezoelectric layer, the upper and bottom surfaces are two electrodes. A cylindrical air domain is fixed around the material where the electric potential is null at the boundary surface. To consider the externally applied magnetic field, all the edge values of $\boldsymbol{a}$ are assigned to zero on the cylindrical surface, except for those crossing a randomly built path (from one end to the other end of the domain) Those edges are shown in red in Figure 3.2 , on which the circulations of $\boldsymbol{a}$ equal to the magnetic flux $\boldsymbol{B} \cdot \boldsymbol{S}_0$, where $\boldsymbol{B}$ is the externally applied magnetic induction and $\boldsymbol{S}_0$ the vector surface of the cross section of the solution domain.

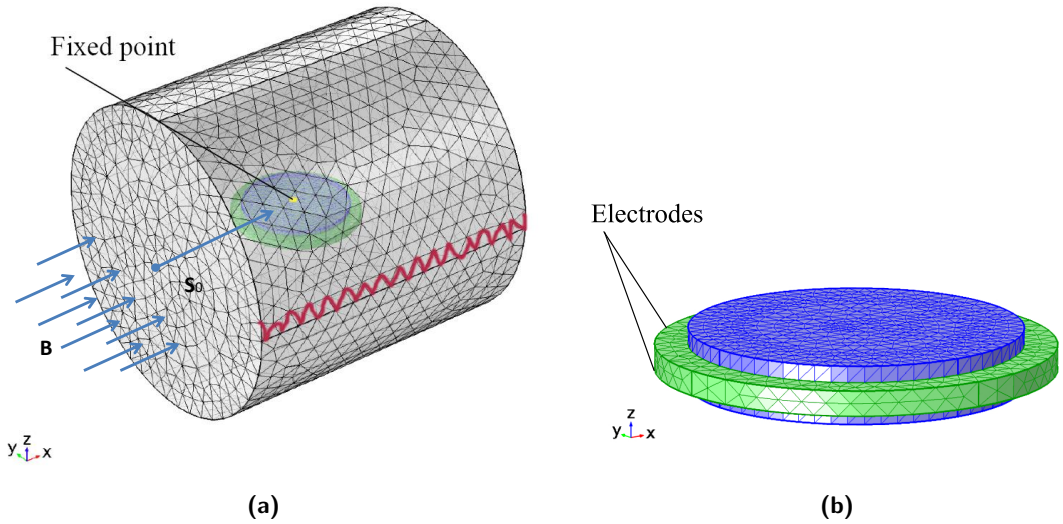

Figure 3.2: Mesh and boundary condition magnetostrictive layer in blue color and piezoelectric layer in green color

In order to validate the proposed model, the study is performed in two steps: First step consists to simulate the behavior of the MEC voltage coefficient in low frequency regime so that the optimal bias point is found. Second step consists to simulate the MEC voltage coefficient in dynamic analysis while taking into account the effect of the eddy currents.

3.3.2 Determination of the optimal magnetostatic bias

Figure 3.3 shows the MEC voltage coefficient $_V$ from the structure in TT-mode in function of $\boldsymbol{H}_{dc}$ (from 0 to 1350 Oe) and under different discrete values of the electrical resistance load R (1 kΩ, 10 kΩ, 50 kΩ, 90 kΩ). The nonlinear simulations have been performed with the piecewise linear solution using at step of $\Delta\boldsymbol{H}_{dc} = 1.35$ Oe (1350/1000). The linear harmonic simulation is performed at 1 kHz with a small dynamic excitation magnetic $\boldsymbol{h}_{ac}(t)$ equals to 1 Oe. It can be noticed that the MEC voltage coefficient $_V$ reaches its maximum around 700 Oe. The simulation results show a suitable agreement with the measurement ones (in TT-mode also) reported in [115] that we have reproduced here in dot-line.

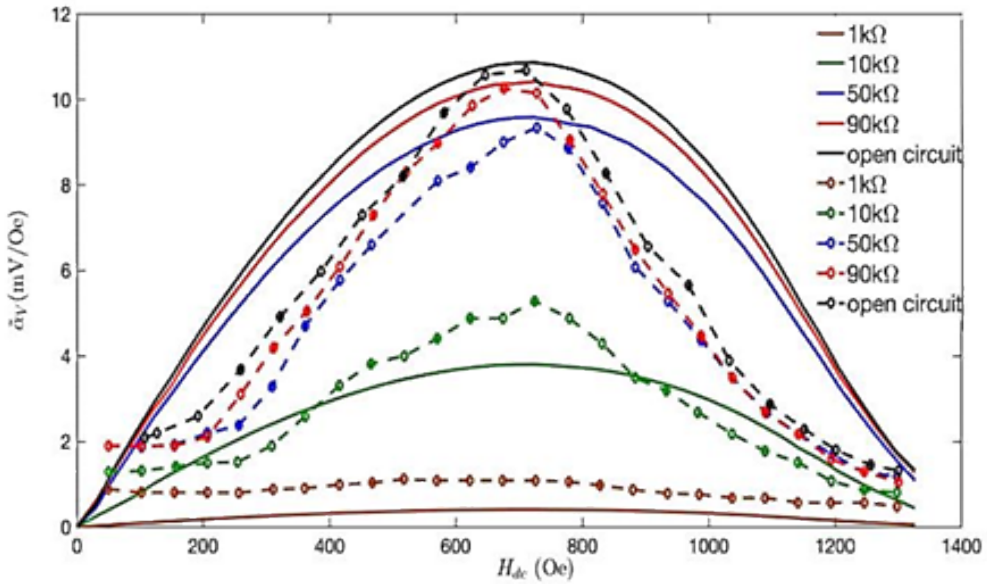

Figure 3.3: ME voltage coefficient as a function of DC magnetic field ($\boldsymbol{H}_{dc}$) under various electrical resistance load values for the ME laminated composite with $\boldsymbol{h}_{ac}(t) = 1$ Oe @ 1 kHz.

In Figure 3.4, the model is capable of representing the 3D diffusion of electric potential and magnetic flux in the domain. The polarization on piezoelectric layer is observed, electric potential vanishes at the boundary of the domain. As can be seen from the figures, magnetic flux are distorted around the material boundary, this is because the permeability of the magnetostrictive layer is relative larger than that of the free space.

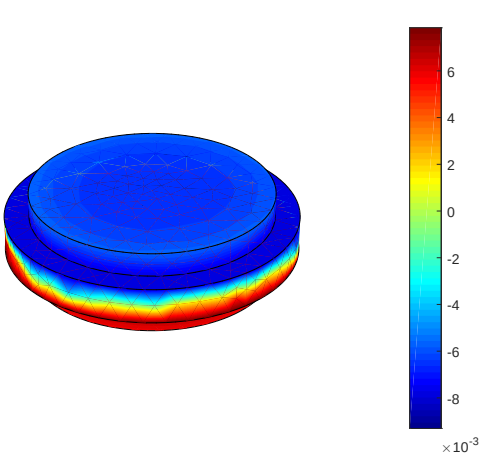

(a) electric potential diffusion

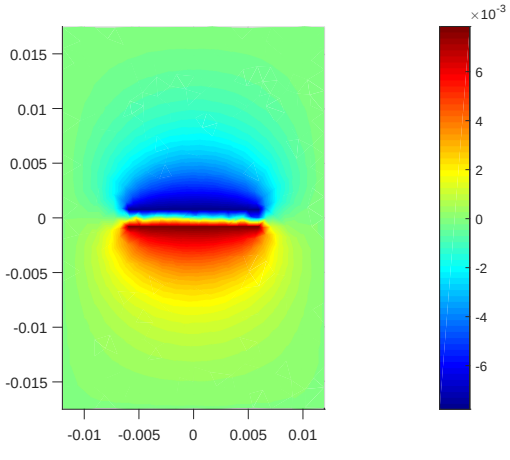

(b) electric potential of vertical section crossing the center

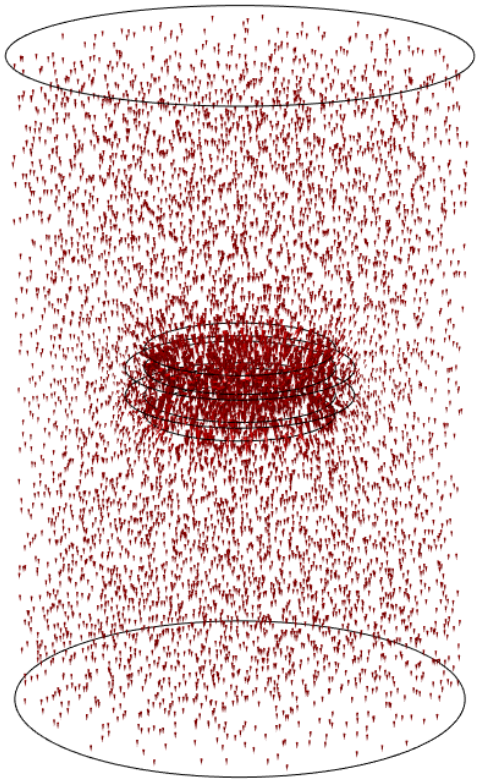

(c) magnetic flux in the domain

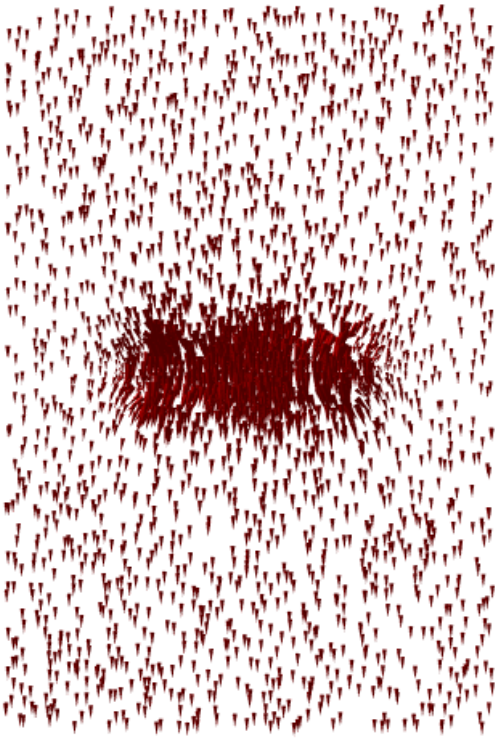

(d) magnetic flux of vertical section crossing the center

Figure 3.4: Simulation results of the model

3.3.3 Frequency response of the ME coefficient

As mentioned in section 2.6, under a dynamic magnetic field, the eddy currents may be induced in the magnetostrictive layer if its conductivity cannot be ignored. In this case, the performances of the MEC will be consequently degraded. Figure 3.5 is an illustration of the eddy currents when the MEC works in TT-mode. The circulating eddy currents

show clearly the skin effect as the frequency increases, which is in accordance with the following expression:

$$\boldsymbol{J} = J_S e^{(1+j)d/\delta} \tag{3.1}$$

where J_S is the current density saturation, $\delta = \sqrt{\frac{1}{\pi f \mu \sigma}}$ is the skin depth and d represents here the radius of the magnetostrictive layer, f stands for the frequency domain.

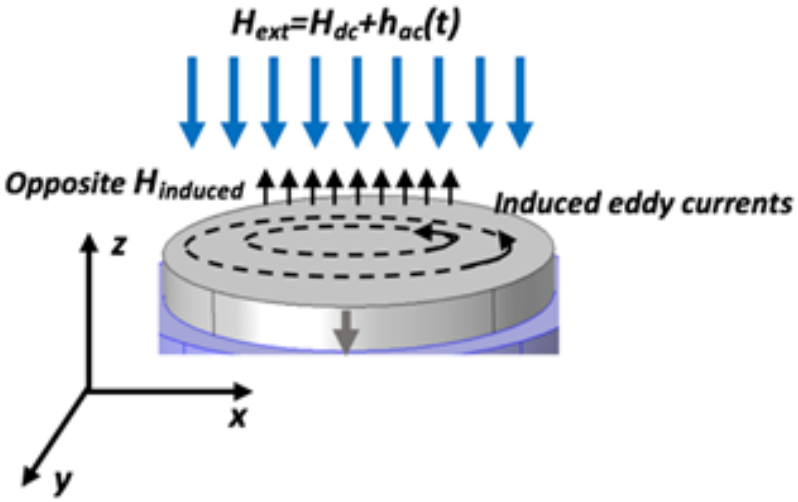

Figure 3.5: Illustration of the eddy-current for TT-mode.

Figure 3.6a, Figure 3.6b and Figure 3.6c shows through the x-y plan the simulated eddy current distribution inside the FeGa when the structure works in TT-mode @ 1 kHz, 10 kHz and 100 kHz, respectively. It can be noticed that the eddy currents concentrate to the edges of the structures as the frequency increases, which demonstrate clearly the skin effect.

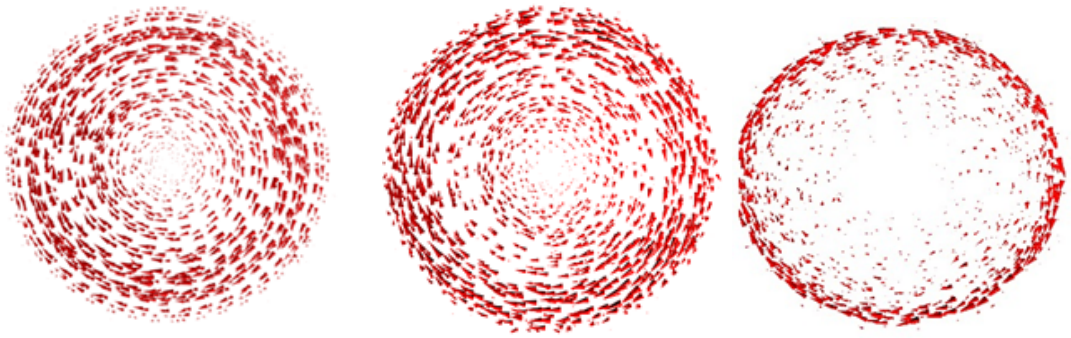

(a) 1 kHz **(b)** 10 kHz **(c)** 100 kHz

Figure 3.6: Distribution of the eddy current magnitude on the FeGa layer in plan x-y

Figure 3.7 shows the frequency dependence of MEC voltage coefficient $\tilde{\alpha}_V$ (in open-circuit condition) and Figure 3.8 shows the output deliverable power under various resistive load R at resonance for both modes in considering or not the effect of eddy currents. In

two cases, the frequency resonances are close to 100 kHz and the ME response of the laminate reaches its maximum. The highest value in TT and LT modes are respectively ≃65mV, ≃450mV with the eddy currents and ≃170mV, ≃1050mV without. The output deliverable power has been extracted in according to the procedure presented in [87]. The highest value in TT and LT modes are respectively ≃1.75 μW, ≃100 μW and ≃8 μW, ≃350 μW with and without eddy currents, respectively. It is interesting to note that the maximum output power obtained in LT mode is ≃100 μW which is enough for application in energy transducer of small electronic devices. As previously, the simulation results in TT-mode show a suitable agreement with the measurement ones reported in [115] that we have reproduced here in dot-line. The difference between the simulations and the experiment in TT mode is likely due to the fact that the damping losses from the thin resin Epoxy used to stick the layers are not included in the simulation, which needs the further investigation.

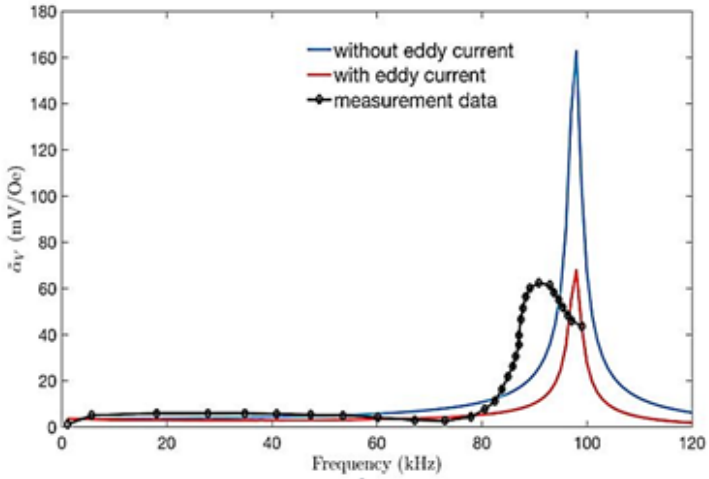

(a) TT mode

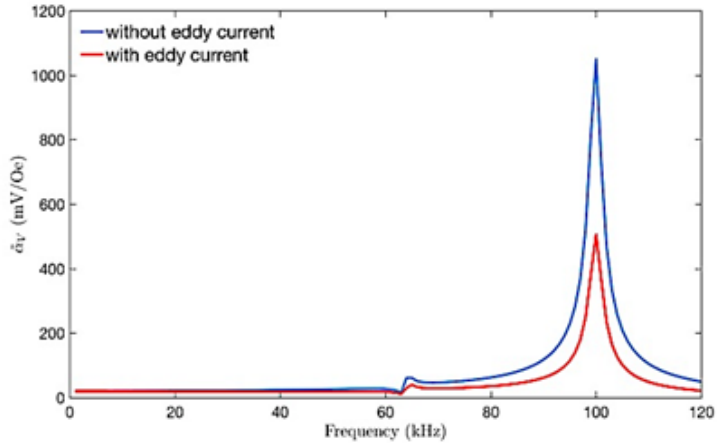

(b) LT mode

Figure 3.7: Frequency dependence of MEC voltage coefficient $\tilde{\alpha}_V$ for both modes (the measurement data in TT mode is extracted from [115]).

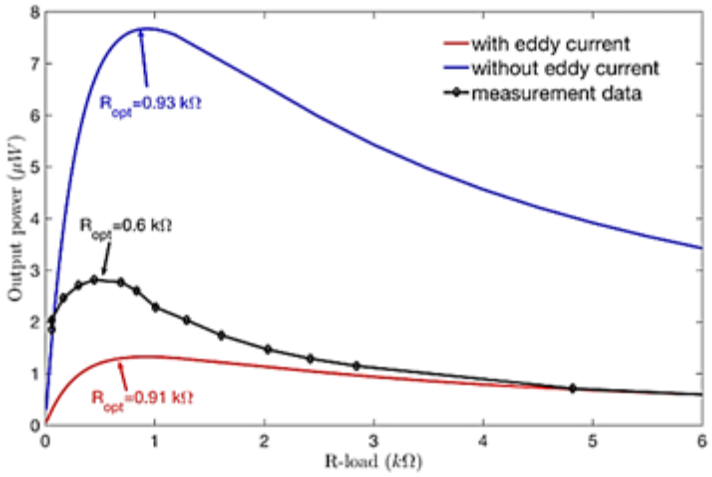

(a) TT mode

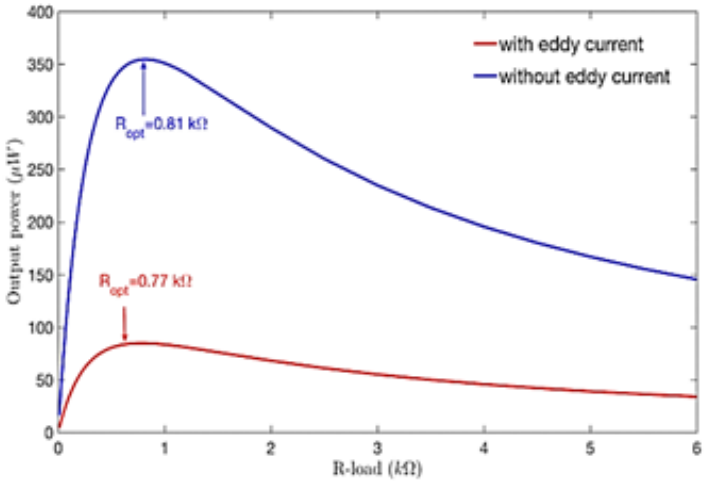

(b) LT mode

Figure 3.8: Output deliverable power as function of electrical load @ resonance for both modes.

Low frequency response

For a better understanding on the influence of eddy current, we calculate the response of composite with circular section under low frequency (from 100Hz to 20kHz). As can be seen from the Figure 3.9, taking to account the effect eddy current, the ME coefficient decreases from 2kHz.

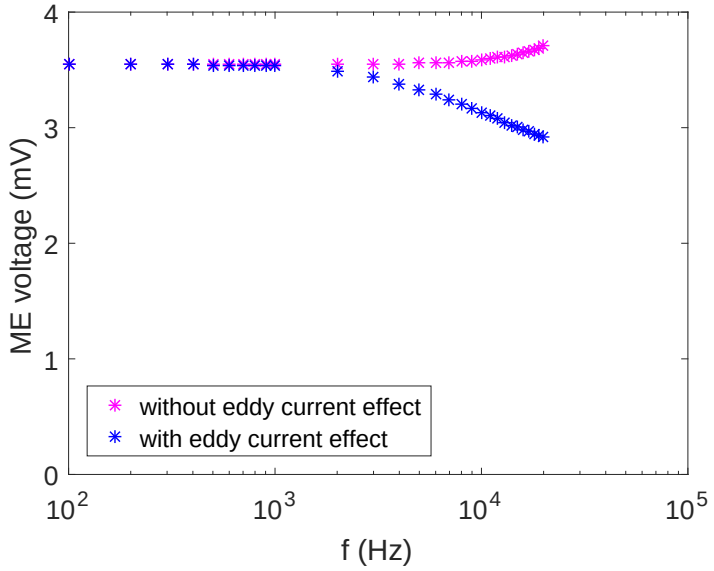

Figure 3.9: The output voltage as a function of frequency (100Hz – 20kHz).

3.3.4 Conclusion for ME laminate composite with circular section

A 3D finite element multiphysics analysis of the performance of ME composites has been presented. The analysis includes two steps. The first step consists of the analysis of the static magnetic biasing which takes into account the non-linear property of the magnetostrictive material by using the DEAM method. The second studies the dynamical performance of the composites based on the small signal assumption using a linear model. The impact of eddy currents is considered in the dynamic modeling. Numerical investigation of a tri-layer laminated ME energy transducer with a circular geometry is taken as an example. The simulations are performed on a tri-layer laminated ME energy transducer disks in TT and LT modes. The results of TT mode show a suitable agreement with the experiment available in the literature and their discrepancy will be further investigated by considering the effect of the resin Epoxy in the future work. The 3D analysis method provides a useful tool to study the performances of ME composites as energy transducers or sensors with complex geometries.

3.4 ME laminate composite in rectangular form

In this section, the performance of ME laminate with rectangular section is examined Figure 3.10. The simulation results are compared with the measurement in our lab by Kevin Malleron.

In fact, numerous 1D models of ME composites of equivalent electric model type exist in the literature. Following the results of these models, magnetoelectric coefficient depends not only on the material properties, but also on the size of the sample. The size of the

sample is defined by the thickness of different layers, the width . . . It is important to study the ME laminate with rectangular section and the influence of geometry parameters by 3D model.

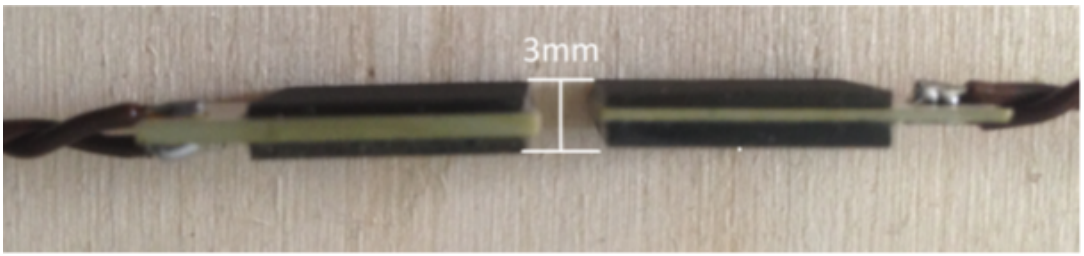

Figure 3.10: Illustration of ME samples with the thicknesses of different layers.

3.4.1 Geometry and boundary conditions

In this section, the ME composite, consisting of Terfenol-D / P51 / Terfenol-D, is considered (Figure 3.11). The magnetostrictive layer with blue color has the dimension of 14x10x1 mm, whereas the piezoelectric in green color has the dimension of 20x10x1 mm. The material properties are presented in Appendix B.1.

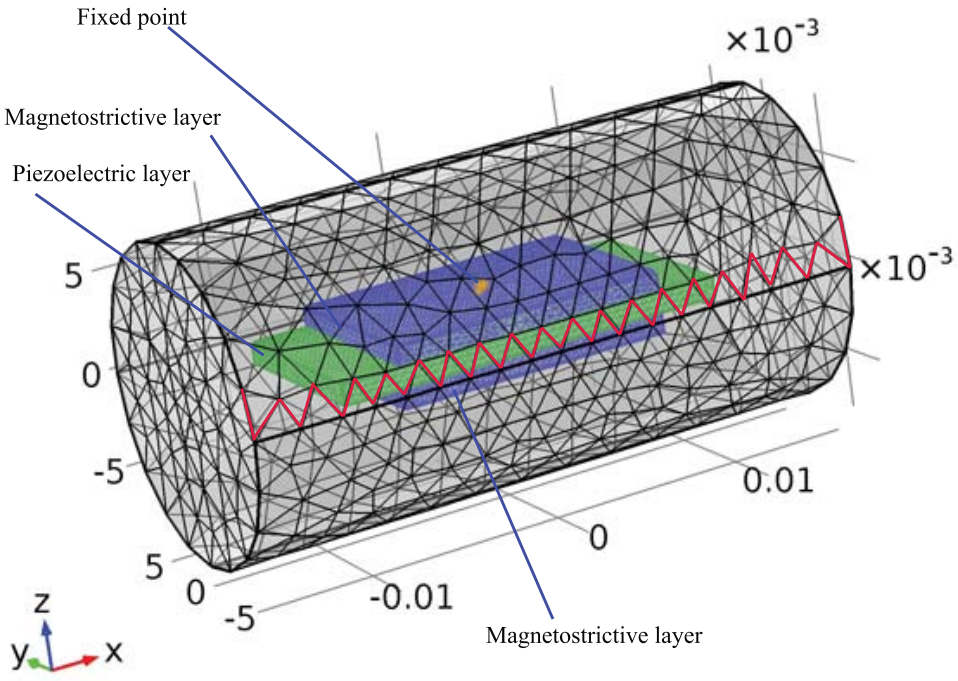

Figure 3.11: The mesh for simulation of ME composite with rectangular section.

We consider a cylinder box of air around the material as the solution domain. As presented

in chapter 2, the points in center of top and bottom faces of the composite are mechanically fixed. In order to introduce the magnetic flux in X direction, the cut line (in red) is build, on the edges of the cut line, the circulation of the magnetic potential is imposed. On the others edges they are assigned to zero. The boundary conditions for electrostatic problem are the same as reported in chapter 2.

3.4.2 Simulation results

Nonlinear magnetostrictive static analysis

Firstly, the nonlinear ME analysis is performed in LT mode. External DC magnetic field increases step by step from 0 Oe to 1000 Oe. At each step, the magnetostrictive coefficients are updated following piecewise linear solution procedure. The output voltage is computed through the harmonic analysis under magnetic field $\boldsymbol{H}_{ac}$ = 5 Oe @ 1kHz using these coefficients. In Figure 3.12, the comparison between simulation result and measurements are depicted, the maximal output voltage are obtained at the magnetic field $\boldsymbol{H}_{dc}$ = 650 Oe.

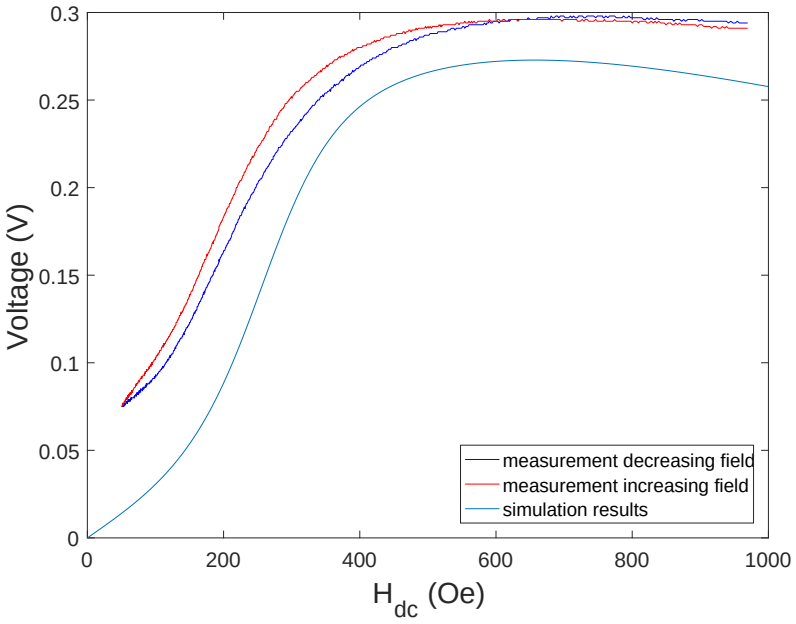

Figure 3.12: ME voltage coefficient as a function of DC magnetic field ($\boldsymbol{H}_{dc}$).

Linear harmonic analysis

Next, the computed coefficient at maximal output voltage will be used for dynamic analysis. The magnetic field is $\boldsymbol{H}_{ac}$ = 1 Oe and the frequency varies from 60 kHz to 80 kHz. The results for numerical computation and measurement are depicted in Figure 3.13. The output voltage reaches the peak at resonance frequency f = 70 kHz with $V_{max} \approx 1.8$ V.

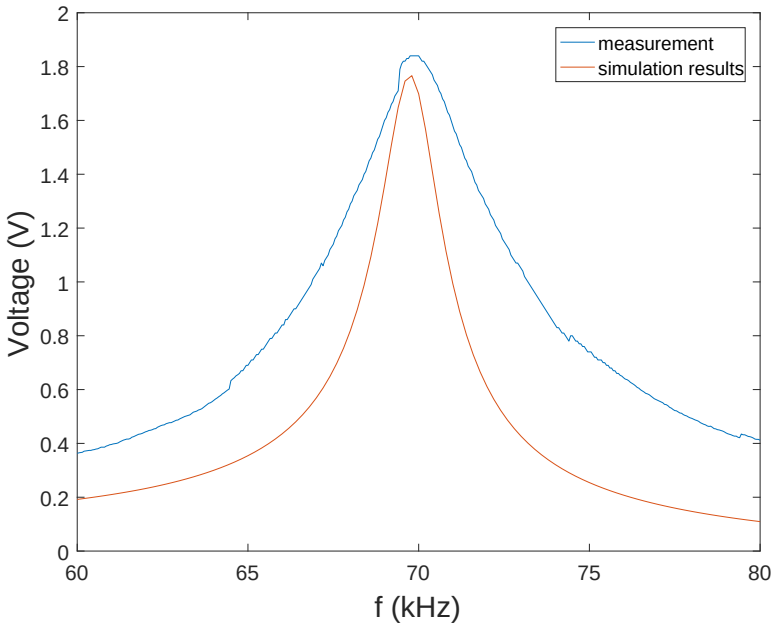

Figure 3.13: The output voltage in resonance frequency.

Field distributions

We present some results of field distributions obtained by 3D model. The magnetostrictive coefficients are obtained at the optimal static magnetic field $\boldsymbol{H}_{dc} = 650$ Oe. R is very large so that it can be considered as open circuit. The applied magnetic field is $\boldsymbol{H}_{ac} = 5$ Oe @ 1kHz.

The obtained magnetic induction is presented in Figure 3.14. As can be seen from the figure, the values of the magnetic induction are very large in the magnetostrictive layer, because the permeability of the magnetostrictive layer is larger than that of the free space and the piezoelectric layer.

Because of the magnetic-mechanic coupling, the magnetostrictive layer is deformed. Through mechanical contact, the piezoelectric layer is also deformed. The deformation of the material can be observed in Figure 3.15. It is symmetry through the axis connecting the two fixed points.

Since the piezoelectric layer is deformed, the electrical polarization is obtained in Figure 3.16. The electric field is concentrated in piezoelectric layer and vanishing near the air boundary.

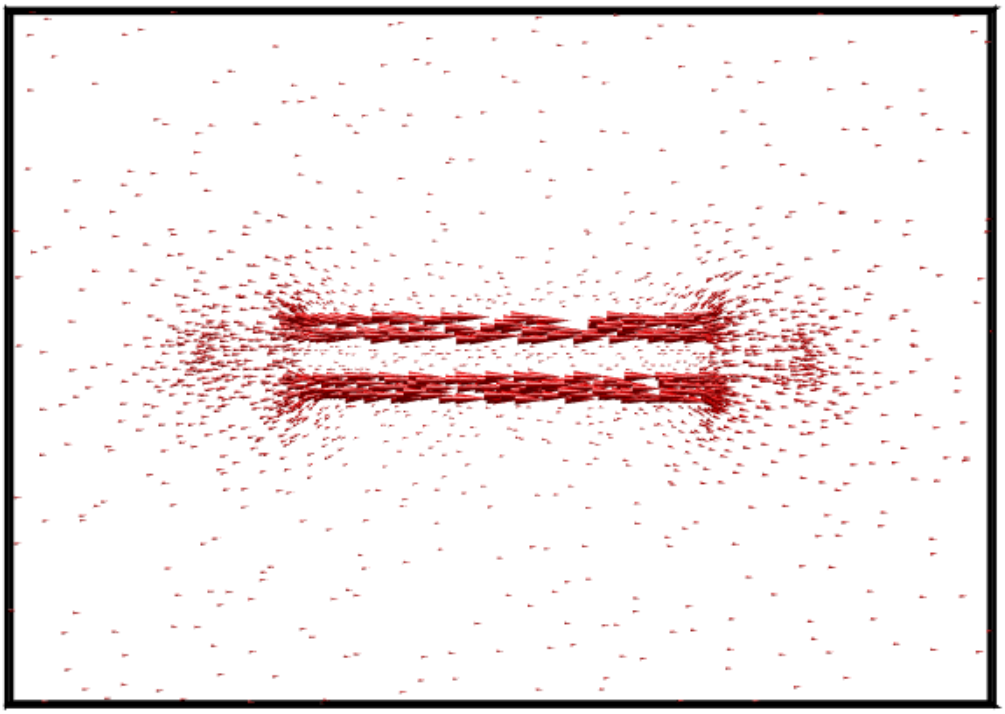

Figure 3.14: The magnetic flux in X direction from XZ view.

3.5 Study of novel structure

In fact, for application in energy transducer, it requires the ME composite being more effective. Thus, the investigation of the influence of the geometry dimension to the output deliverable power is required. A simulation tool which can properly consider the structure effect of the complex interaction is needed for optimal design of future ME structures. This section proposes to use the 3D FEM multiphysic code to investigate the effect of the layer width for the performance on rectangular laminated structure composed of Terfenol-D/PZT-5A/Terfenol-D.

3.5.1 Geometry and boundary condition

In this section, the 3D model is used to study the behavior of rectangular surface ME structures and the influence of the width parameter. The output power $P = V^2/R$ (W) is used to evaluate the performance of the structure, its capacity to supply a device represented by the electrical impedance Z. The simulation results in [118] show that a decrease in the width of the laminar ME composite generates a greater voltage. On the other hand, the decrease in the volume of material causes a decrease in the output power. From these observations we opted to model the laminar composite structures by modifying the width of the material. Three different forms are considered: (A) Example A is the standard structure of 5 mm width for all layers; (B) Example B uses a width of 1 mm for all layers; (C) Example C is a new shape like "⌅-shape" with 5 mm width

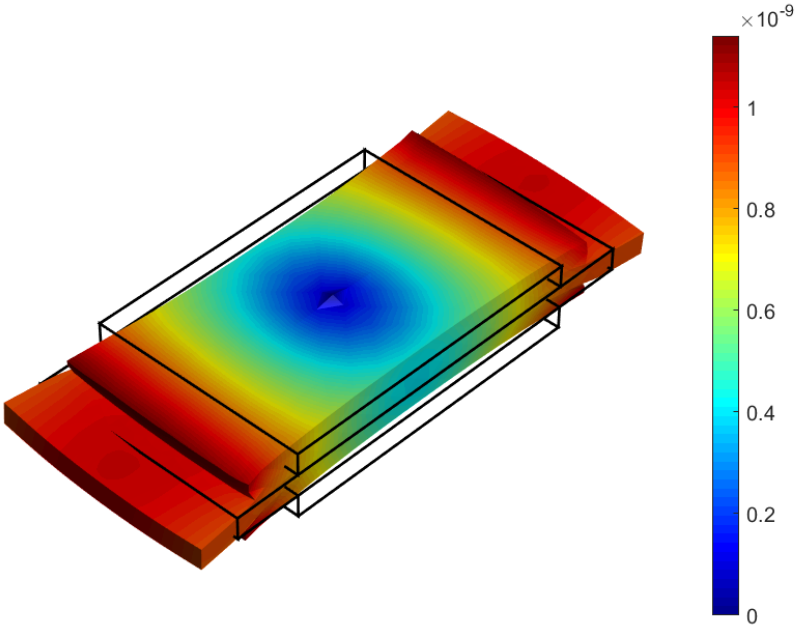

(a) 3Dview

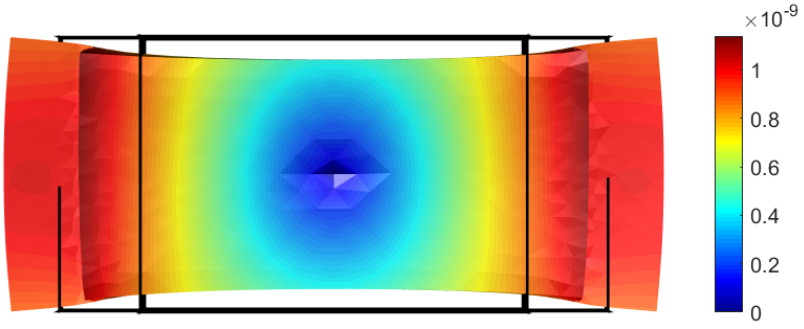

(b) XY view

Figure 3.15: The deformation of the composite.

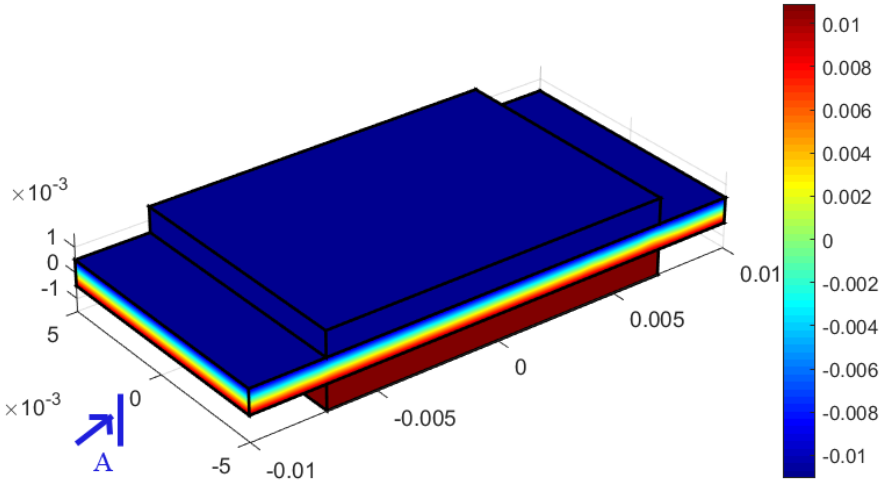

(a) Electric potential diffused on ME composite

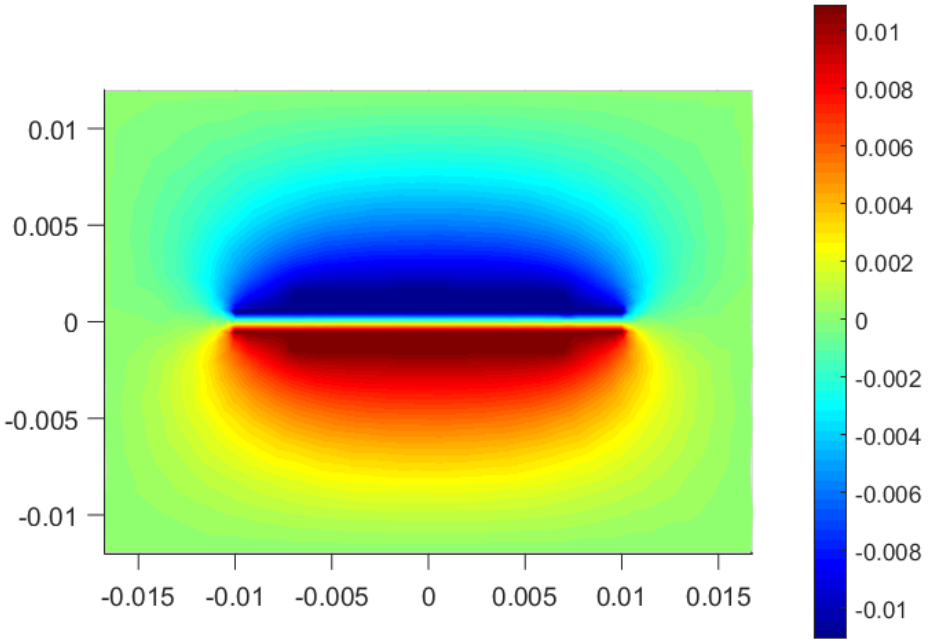

(b) Electric potential on section A

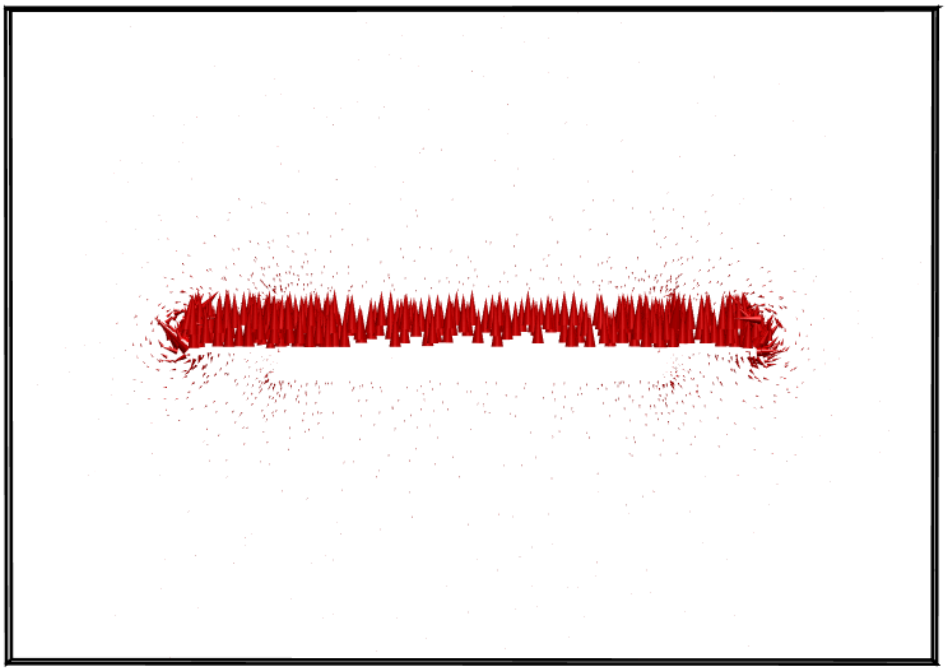

(c) Electric field on section A

Figure 3.16: The deformation of the composite.

for the magnetostrictive layers ($w_P = 5$) and 1 mm width for the central piezoelectric layer ($w_m = 1$) (Figure 3.17b). All layers are of 12 mm length and 1 mm thickness. All the structures are calculated under a dynamic magnetic field excitation of $\boldsymbol{H}_{ac} = 1$ Oe and the same values of the material coefficients are used for all structures (Terfenol-D for magnetostrictive and PZT-5A for piezoelectric). The material properties of PZT-5A are given in Appendix and which of Terfenol-D are calculated using DEAM.

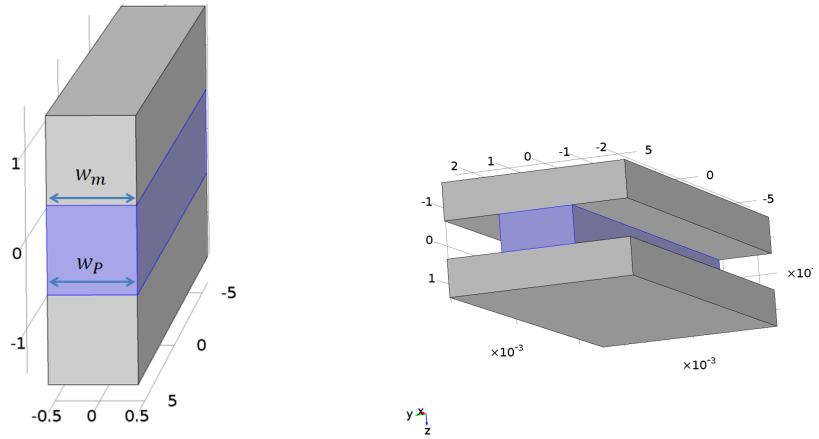

(a) ME laminate rectangular form

(b) ME laminate "Ⲏ-shape"

Figure 3.17: The classical rectangular geometry and the novel structure.

The solution domain considered in this study is a cylindrical air box enveloping the magnetoelectric device (Figure 3.18). The zero displacement condition is applied on the middle

of the top and bottom surfaces. The Dirichlet condition $\psi = 0$ is applied on the outer boundary of the solution domain. For the magnetic vector potential $\boldsymbol{a}$, the Dirichlet condition is applied on the cylindrical surface. To consider the externally applied magnetic field, all the edge values of $\boldsymbol{a}$ are assigned to zero on the cylindrical surface, except for those crossing a randomly built path (from one end to the other end of the domain). Those edges are shown in red in Figure 3.18, on which the values of $\boldsymbol{a}$ equal to the magnetic flux $\boldsymbol{B} \cdot \boldsymbol{S}_0$, where $\boldsymbol{B}$ is the externally applied magnetic induction and $\boldsymbol{S}_0$ the vector surface of the cross section of the solution domain.

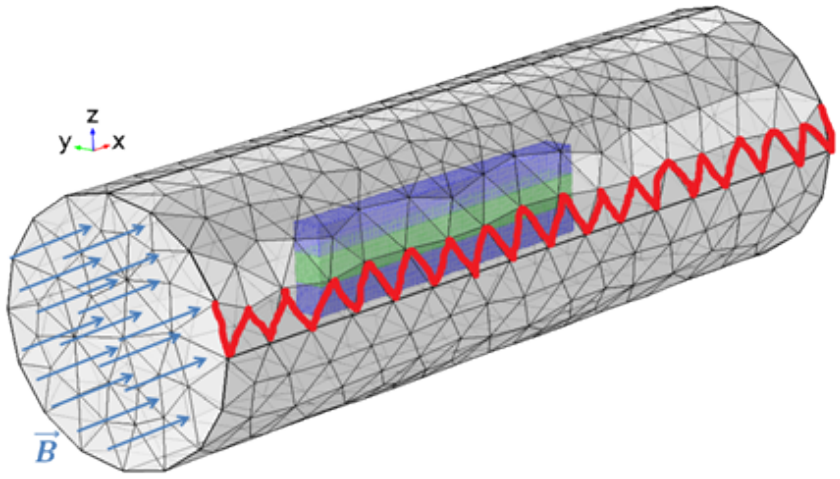

Figure 3.18: The study domain enveloping the magnetoelectric device. In red the cutting path on which nonzero edge values of a are applied to impose the magnetic flux.

3.5.2 Linear harmonic magnetoelectric analysis

In order to compare the performance of these forms, the linear harmonic magnetostrictive analysis is carried out under a given magnetic bias. When dynamic excitations are of small magnitudes, material constants can be viewed invariant around the working points which are determined under the magnetic bias condition. Consequently, the underlying problem is linear and we consider also the piezoelectric material homogenous. The analysis provides the details regarding the voltage output and the power output. Additionally, it demonstrates the capability of the 3-D finite element model to take into account the eddy currents (Figure 3.19). In Figure 3.19a, 3.19b, the eddy currents on a section perpendicular to the magnetic field direction are shown respectively under the frequency of 10kHz and under the resonance ($\simeq$82kHz). The skin effect is more pronounced at the higher frequency. The influence of eddy currents has been investigated in 3.3.3. Figure 3.19c compares the magnetoelectric coefficient $\tilde{\alpha}_V$ as a function of frequency with and without the eddy currents for the structure B and shows clearly the impact of the eddy currents on the performance of magnetoelectric device.

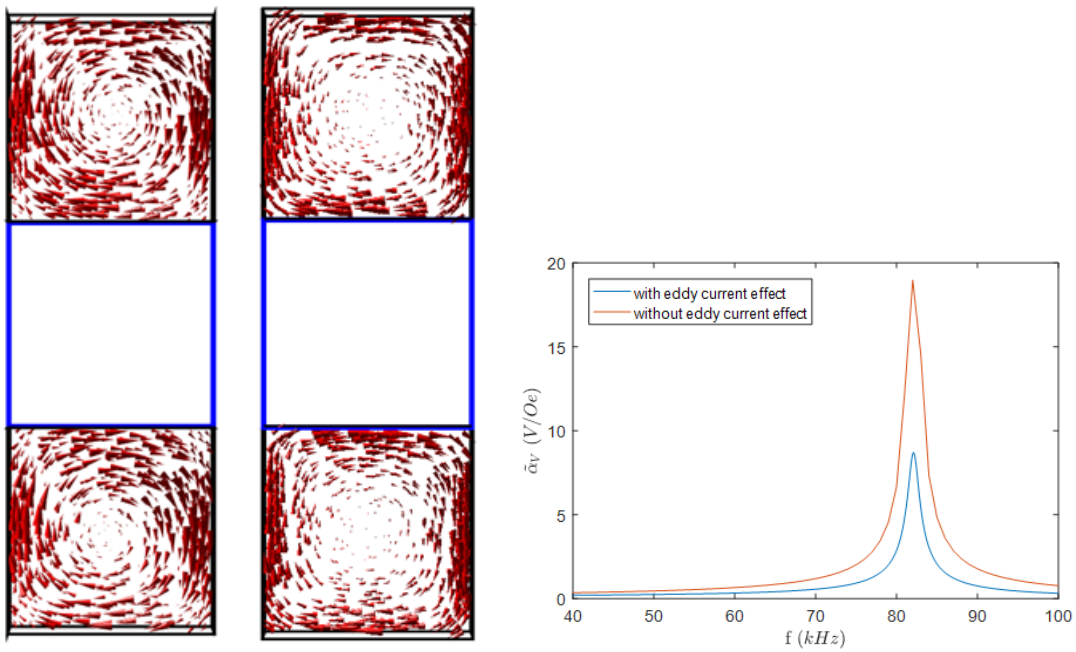

Figure 3.19: The ME eddy current induced in a X-Z plan (a) under 10kHz (b) and under the resonance frequency (c), and the effect of eddy currents for the structure B.

The evolution of the magnetoelectric coefficient $\tilde{\alpha}_V$ as a function of frequency is shown in Figure 3.20 for the 3 structure forms. It can be noticed that the example C has an output voltage about 15 V/Oe, which is larger in comparison with the conventional rectangular forms A and B (about 8 V/Oe and 9 V/Oe, respectively). The resonance frequency of this new structure is 66 kHz, while those of the first two structures are around 82 kHz.

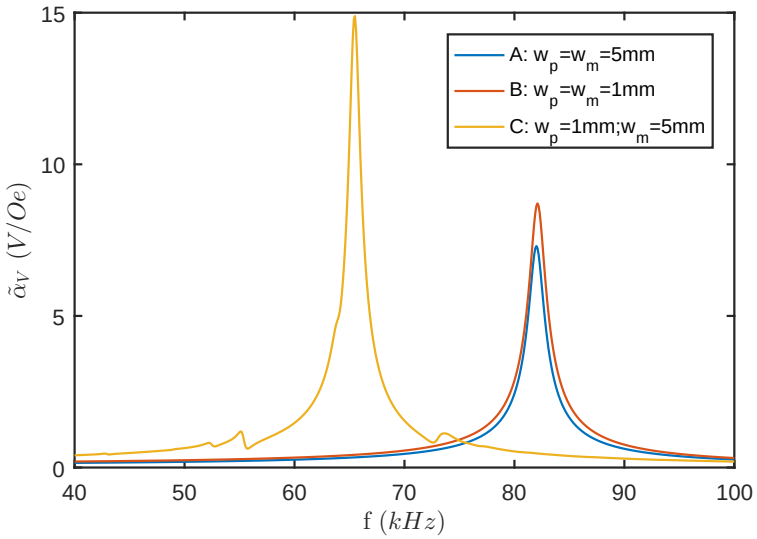

Figure 3.20: Frequency (f) dependence of ME coefficient for the three forms of ME laminated composite.

The output power P (W) is calculated at the resonance frequency and is plotted against the electric load R in Figure 3.21 for the 3 structures to compare their performance. The new shape C generates the best power ≃3.2 mW. B has a higher output voltage than A (9 V/Oe and 8 V/Oe) but its output power is much lower (<1 mW for B and ≃2.2 mW for A). This is explained by the reduction of the electric current because the surface of the piezoelectric material is smaller.

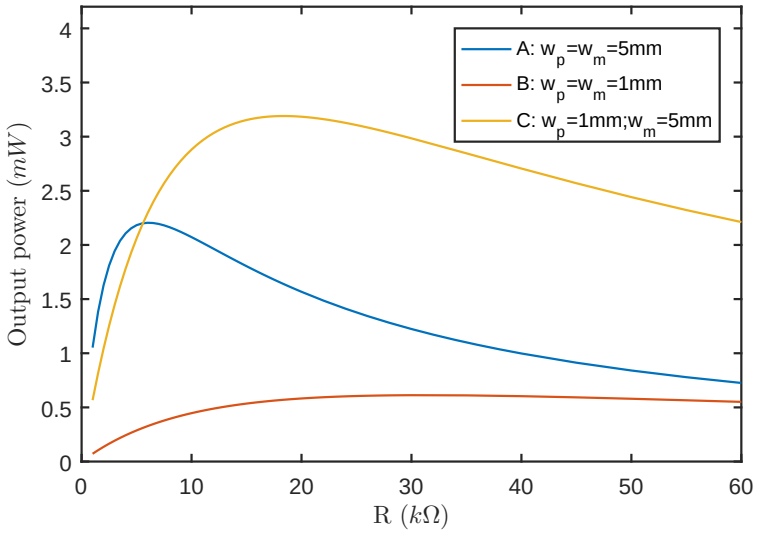

Figure 3.21: The output power P as a function of electrical resistance load for the three forms ME composite.

3.5.3 Study the influence of geometry parameter

The previous results motivated us to study the influence of the width of piezoelectric material w_P on the performance of new form C. We therefore modeled structures with w_P varying between 0.4 and 5 mm in order to obtain the optimal parameter for this new structure. It can be noticed that for the value of $w_P = 5$mm, C is equivalent to A.

The results of voltage and output power as a function of the width w_P are shown in Figure 3.22 and Figure 3.23. In Figure 3.22, it is observed that the maximum voltage corresponds to a width w_P of the piezoelectric layer of 0.6 mm. With the structure becomes narrow, the internal magnetic field will approach the external one [118]. The increasing of the magnetic field causes a larger strain in magnetostrictive layers. As a result, the piezoelectric layer will be polarized and generate a stronger electrical field.

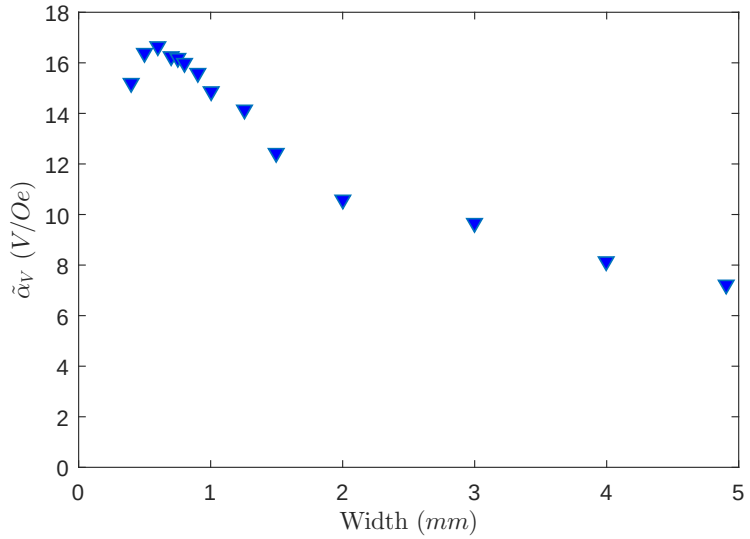

Figure 3.22: The ME coefficient as the function of w_P.

In Figure 3.23, the highest output power, of the order of 3.5 mW, is obtained for a width w_P of the piezoelectric layer of 0.8 mm.

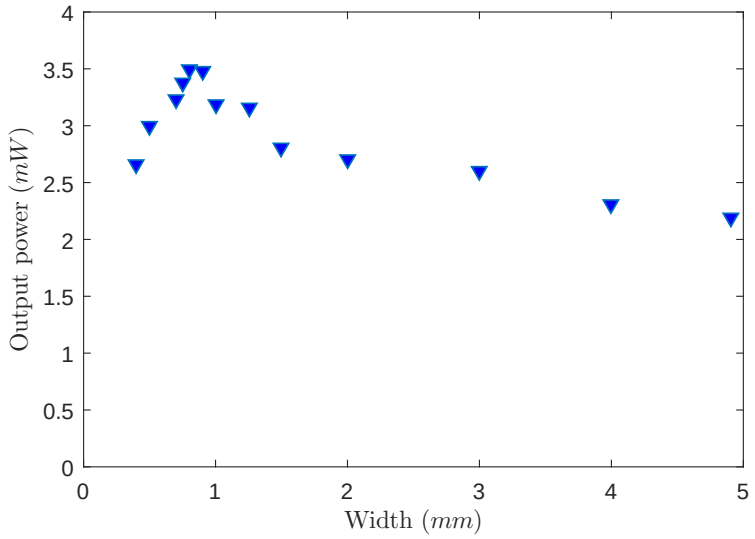

Figure 3.23: The output power P as the function of w_P.

In terms of the dynamic response, the width dependence of resonance frequency is shown in the Figure 3.24. With the decrease in the width of the piezoelectric layer, resonance frequency decreases gradually. Since the width decreases, the structure has lower stiffness and consequently lower the resonance frequency [114].

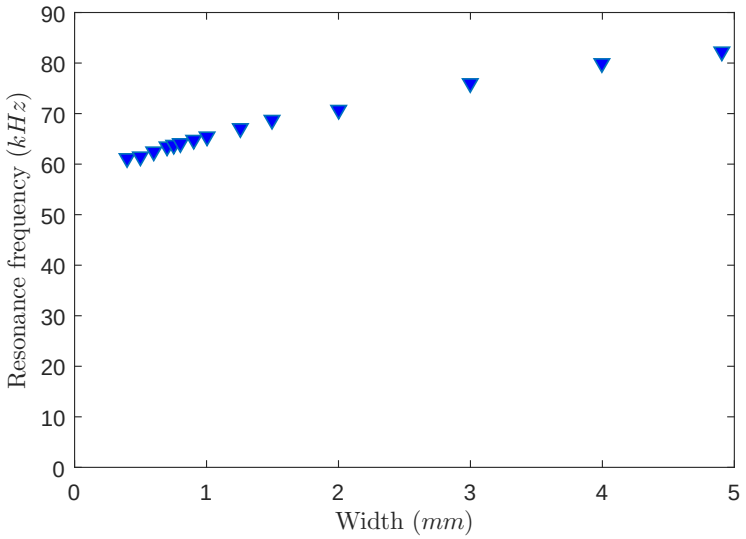

Figure 3.24: The frequency resonance as the function of w_P.

3.6 Conclusion

In this chapter, the linear harmonic analysis of the ME composite with circular section has been performed considering the influence of the eddy currents. The simulations are examined on a tri-layer laminated ME energy transducer disks in TT and LT modes. The results of TT mode show a suitable agreement with the experiment available in the literature.

The simulation of ME laminate with rectangular section has been presented. The results show good agreement in terms of nonlinear behavior and the maximum output voltage at resonance. Some results of field distributions have been reported.

The 3D model can be a useful tool to study the performance of complex geometries. A new structure has been presented which have the potential to generate more power for energy harvester.

In the next chapter, the other type of ME composite will be considered, the fiber composite and the particulate composite. The researches of these structures are still limited. Unlike the laminate composite, it is difficult to apply the FEM in macroscopic scale because of the complicated structure. Therefore, we will use the theory of homogenization in the next chapter. A REV which consists of a matrix and an inclusion is chosen to be investigated. The 3D FE is applied on this REV and performs the calculation.

Chapter 4

Homogenization of magnetoelectric 0-3 type and 1-3 type composites

Summary

4.1 Introduction

The ME composites can be found in three types: the laminate structure (2-2 type), the rod matrix structure (1-3 type) and the particle matrix structure (0-3 type). Among them, the composite laminate is the most widely used and investigated, while the number of researches for the other structures is still limited. The 3D finite element (FE) code has been developed to investigate the 2-2 type ME materials laminated structures in the previous chapter. This approach proved to be practical for homogeneous materials. However, for the 0-3 type ME particulate structure, the size of particles is the order of micrometers or nanometers according to the fabrication method (Figure 4.1). The FE calculation at macroscopic scale for the device of millimeters is not suitable anymore to take into account the tiny size of particles. The mesh of this structure can be very dense and that requires high computation time.

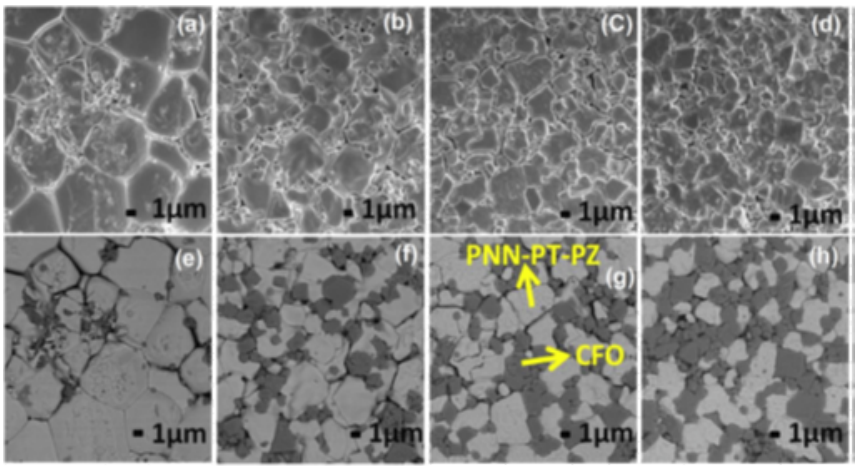

Figure 4.1: Microstructure of ME based perticulate composite [121]

Many specialized numerical methods have been developed and connected for the description of material behavior from nanoscale to mesoscale [122]. One of the strategies is considering a representative elementary volume (REV), a simple geometry with a particle embedded in a matrix for example, and performing the homogenization. Analytical methods have been proposed for estimating or formulating the effective properties of heterogeneous materials.

Fiber composite (1-3 type) was treated by non-self-consistent approach in [32] based on the Green's function method. Next, Li and Dunn [123] propose the Mori-Tanaka method to calculate the effective electro-magneto-elastic moduli of cylinder fibrous.

To deal with the fiber or particle composite structure, Romain [124] employs homogenization techniques adapted to coupled phenomena. The state variables of coupled problem are decomposed to conserve the classical uncoupled homogenization rules. This approaches is efficient but often limited to specific simple structures [124] (fiber composite, for example). Numerical homogenization techniques overcome the limitations mentioned above. In another way, the FE method can be appropriate to the homogenization procedure. This numerical calculation can be applied for complicated structures. The FE analysis

of REV has been presented in [125] where the magnetic scalar potential is used for the magnetic formulation. However, this approach cannot take into account the eddy currents in dynamics.

In this chapter, the FE method, presented in Chapter 2 where the formulation is established in terms of the magnetic vector potential using the edge elements for magnetic problem, is used for the REV analysis. This approach allows us to consider the eddy currents in dynamic regime. In the homogenization procedure, the local fields are averaged to get the effective properties of REV in macroscopic scale. In section 4.2, the basic equations and the boundary value problem are given. In section 4.3, the homogenization of a cylindrical composite of a rod matrix structure (1-3 type) is considered and compared with the analytical result in [124] for the validation of the method. The proposed method is then extended to investigate the behavior of a cubic inclusion composite which is not enabled for the analytical model.

4.2 Finite element analysis of REV

A REV of a ME fiber or particulate structure is taken as the studied domain. The finite element formulation is applied to solve the three coupled physical equations. The physical equations and the finite element formulation of the ME composite problem have been reported in chapter 2. They are briefly recalled below for the sake of clarity.

4.2.1 General equation

We firstly consider the case in statics, i.e. the elastic, the magnetostatic and the electrostatic field equations:

$$\begin{cases} \text{div } \boldsymbol{T} + \boldsymbol{f} = 0 \\ \text{curl } \boldsymbol{H} = \boldsymbol{J} \\ \text{div } \boldsymbol{D} = \rho \end{cases} \tag{4.1}$$

where $\boldsymbol{T}$ is the mechanical stress tensor, $\boldsymbol{f}$ the external applied volume force, $\boldsymbol{H}$ the magnetic field, $\boldsymbol{J}$ the current density, $\boldsymbol{D}$ the displacement field and ρ the volume density of the free electric charge.

The constitutive relations are the combination of the electro-mechanical and the magneto-mechanical constitutive laws of the respective magnetostrictive material and piezoelectric material [61]:

$$\begin{cases} \boldsymbol{T} = c\boldsymbol{S} - e^t\boldsymbol{E} - h^t\boldsymbol{B} \\ \boldsymbol{H} = -h\boldsymbol{S} + \nu\boldsymbol{B} \\ \boldsymbol{D} = -e\boldsymbol{S} + \varepsilon\boldsymbol{E} \end{cases} \tag{4.2}$$

where $\boldsymbol{S}$ denotes the mechanical strain, $\boldsymbol{B}$ the magnetic induction, $\boldsymbol{E}$ the electric field. The material coefficients $h = q\nu$, with q the piezomagnetic coefficient and ν the reluctivity, c the elastic stiffness under constant electric and magnetic induction fields, e the piezoelectric coefficient and ε the permittivity.

The fields $\boldsymbol{S}$, $\boldsymbol{E}$ and $\boldsymbol{B}$ can be expressed, respectively, by the state variables: the mechanical displacement $\boldsymbol{u}$, the electric scalar potential v and the magnetic vector potential $\boldsymbol{a}$.

$$\begin{cases} \boldsymbol{S} = \mathfrak{D}\boldsymbol{u} \\ \boldsymbol{B} = \text{curl } \boldsymbol{a} \\ \boldsymbol{E} = -\text{grad } v \end{cases} \tag{4.3}$$

It can be noticed that in our study, the assumption of small displacement is made and the linear strain–displacement relations is assumed.

4.2.2 FE matrix equation

The problem 4.1 is solved using the FE in 3D. Applying the variational principal to equation 4.1 in considering the equations 4.2 and 4.3, we get the following variational formulation.

$$\begin{cases} \int_\Omega \mathfrak{D}\boldsymbol{u}'(c\mathfrak{D}\boldsymbol{u} + e^t\text{grad } v - h^t\text{curl } \boldsymbol{a})d\Omega = \int_\Omega \boldsymbol{u}'\boldsymbol{f}d\Omega \\ \int_\Omega \text{curl } \boldsymbol{a}'(-h\mathfrak{D}\boldsymbol{u} + \nu\text{curl } \boldsymbol{a})d\Omega = 0 \\ \int_\Omega \text{grad } v'.(e\mathfrak{D}\boldsymbol{u} - \varepsilon^S\text{grad } v)d\Omega = 0 \end{cases} \tag{4.4}$$

where $\boldsymbol{u}', v', \boldsymbol{a}'$ are the test functions.

Equation 4.4 is discretized using the Galerkin approach. The nodal elements are applied for the mechanical displacement $\boldsymbol{u}$ and the electric scalar potential v, whereas the edge elements are used for the magnetic vector potential $\boldsymbol{a}$. The degrees of freedom are respectively the nodal displacement, the nodal electric potential and the line integral of $\boldsymbol{a}$ along edges. We obtain the matrix equation:

$$[\boldsymbol{K}]\{X\} = [F] \tag{4.5}$$

with $\{X\} = \{\boldsymbol{u},\ \boldsymbol{a},\ v\}^t$ and

$$[\boldsymbol{K}] = \begin{bmatrix} \boldsymbol{K}_{uu} & -\boldsymbol{K}_{au}^t & \boldsymbol{K}_{uv} \\ -\boldsymbol{K}_{au} & \boldsymbol{K}_{aa} & 0 \\ \boldsymbol{K}_{uv}^t & 0 & -\boldsymbol{K}_{vv} \end{bmatrix}$$

4.2.3 Periodic boundary condition

According to the periodicity in the composite structure (Figure 4.2), the periodic boundary conditions for all the elastic, electric and magnetic fields are applied. As a result, the boundary meshes on the opposite boundary surfaces of the REV are made the same as presented in Figure 4.3.

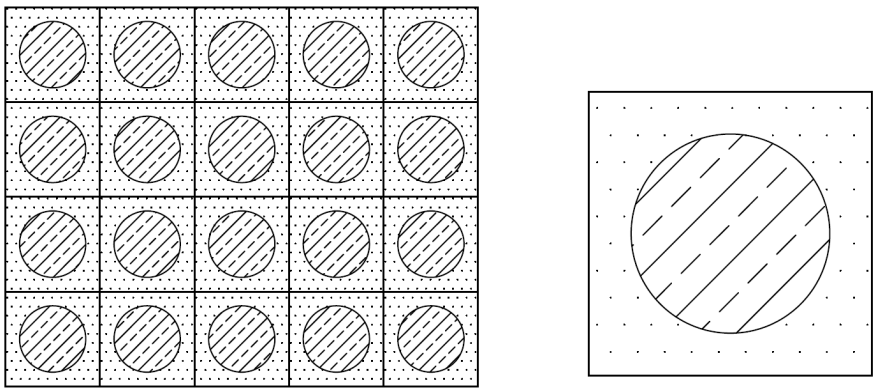

Figure 4.2: The square periodic arrangement and a representative elementary volume. (REV)

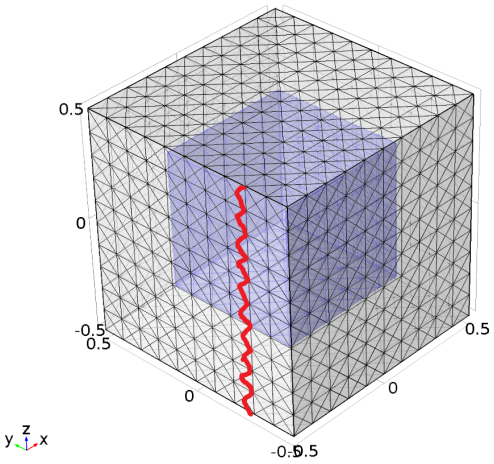

Figure 4.3: Mesh of a periodic REV cell. In red: cutting edges on which nonzero edge values of a are applied to allow the magnetic flux crossing the cell.

Let us denote k_i a point on the boundary surface normal to the $i(i = x, y, z)$ direction, $k_i{+}_i$ is then its counterpart on the opposite surface, where d_i is the ith component of the vector of periodicity [125].

Considering firstly the displacement field $\boldsymbol{u}$. To ensure the periodicity of the stain field, the jth component of the displacement u_j at the $k_i + d_i$ point must satisfy:

$$u_j(k_i + d_i) = u_j(k_i) + \bar{S}_{ji} d_i \tag{4.6}$$

where $\bar{S}_{ji}$ is the average strain. The microscopic displacement field on the RVE boundary $u_j\ (k_i + d_i\ )$ can be decomposed into two parts: the mean part $\bar{S}_{ji}d_i$ and the fluctuation part $u_j(k_i)$ based on [126].

In the same way for the electric scalar potential v, to guarantee the periodicity of the electric field, the scalar potentials on the opposite boundary surfaces are related by

$$v(k_i + d_i) = v(k_i) + \bar{E}_i d_i \tag{4.7}$$

with $\bar{E}_i$ the average i^th component of the electric field.

Next, for the magnetic vector potential $\boldsymbol{a}$, to guarantee the periodicity of the magnetic induction, we can impose the edge values of $\boldsymbol{a}$ (the circulation $\boldsymbol{a}$ along edges) to be equal on the boundary edges of the opposite sides (k_{i1}, k_{i2}) and $(k_{i1}+d_i, k_{i2}+d_i)$. This treatment is however not satisfactory because it will not allow the magnetic flux passing through the REV, since the line integral of the vector potential $\boldsymbol{a}$ on a close contour passing two pairs of opposite boundary surfaces will be identically zero. To overcome this problem, a random cutting path composed of cutting edges is introduced on the boundary surfaces for each direction as shown in the Figure 4.3. On each cutting edge of the cutting path, a value ϕ_j is added, where ϕ_j is the magnetic flux crossing the surface in j direction, perpendicular to the surface of the cutting edge. With this treatment, the edge values of the magnetic potential on the edges of opposite boundary surfaces fulfill the following relation:

$$a(k_{i1} + d_i, k_{i2} + d_i) = a(k_{i1}, k_{i2}) + c_j\phi_j + c_k\phi_k \tag{4.8}$$

where i, j, k can be respectively x, y, z, $c_j = 1$ or -1 if the edge belongs to the randomly build cutting path and $c_j = 0$ for the other edges.

4.2.4 Homogenization

The homogenization procedure is illustrated in Figure 4.4. To compute the effective macroscopic coefficients of the ME composite, the matrix equation 4.5 is solved by applying, respectively, a constant field component of $\boldsymbol{S}$, $\boldsymbol{B}$ or $\boldsymbol{E}$ while maintaining other components null. This will be done by using periodic boundary conditions of $\boldsymbol{u}$,$\boldsymbol{a}$ and v given in 4.6, 4.7, 4.8. Once the equation 4.5 is solved, the field distribution of $\boldsymbol{S}$, $\boldsymbol{B}$ or $\boldsymbol{E}$ are computed from the state variable $\boldsymbol{u}$,$\boldsymbol{a}$ and v using the relation 4.3, while the field distribution of $\boldsymbol{T}$, $\boldsymbol{H}$ or $\boldsymbol{D}$ are determined by the local constitutive laws 4.2.

The volume average of the stress, the magnetic field and the electric displacement are further computed to estimate the effective material coefficients: $\bar{T} = \frac{1}{V}\int \boldsymbol{T}dV$, $\bar{H} = \frac{1}{V}\int \boldsymbol{H}dV$, $\bar{D} = \frac{1}{V}\int \boldsymbol{D}dV$.

The effective properties of the magnetoelectric composite are finally defined as relations between the volume averages of these fields and the excitation fields over the REV of the ME composite according to the following effective constitutive relation:

$$\begin{bmatrix} \bar{\boldsymbol{T}} \\ \bar{\boldsymbol{H}} \\ \bar{\boldsymbol{D}} \end{bmatrix} = \begin{bmatrix} \tilde{\boldsymbol{C}} & -\tilde{\boldsymbol{h}}^t & -\tilde{\boldsymbol{e}}^t \\ \tilde{\boldsymbol{h}} & \tilde{\boldsymbol{\nu}} & \tilde{\boldsymbol{\alpha}}_H^t \\ \tilde{\boldsymbol{e}} & \tilde{\boldsymbol{\alpha}}_H & \tilde{\boldsymbol{\varepsilon}} \end{bmatrix} \begin{bmatrix} \bar{\boldsymbol{S}} \\ \bar{\boldsymbol{B}} \\ \bar{\boldsymbol{E}} \end{bmatrix} \tag{4.9}$$

where $\tilde{\boldsymbol{\alpha}}_H$ represents the coupling effect between the magnetic and electric fields, which does not exist in local scale, $\tilde{\boldsymbol{h}}$ the effective magnetostrictive coefficient, $\tilde{\boldsymbol{e}}$ the effective piezoelectric coefficient, $\tilde{\boldsymbol{C}}, \tilde{\boldsymbol{\nu}}, \tilde{\boldsymbol{\varepsilon}}$ are respectively effective stiffness, reluctivity, permittivity.

To determine the effective coefficients, it is essential to apply individually six constant strain states, three uniaxial constant electric fields and three uniaxial constant magnetic fields. For instant, a strain state is applied $\bar{S}_{11}$, the other state should be zero averaged by employing periodic boundary condition, we obtain

$$\begin{bmatrix} \bar{T}_{11} \\ \bar{T}_{22} \\ \bar{T}_{33} \\ \bar{T}_{23} \\ \bar{T}_{31} \\ \bar{T}_{12} \\ \bar{H}_1 \\ \bar{H}_2 \\ \bar{H}_3 \\ \bar{D}_1 \\ \bar{D}_2 \\ \bar{D}_3 \end{bmatrix} = \begin{bmatrix} \tilde{\boldsymbol{C}} & -\tilde{\boldsymbol{h}}^t & -\tilde{\boldsymbol{e}}^t \\ \tilde{\boldsymbol{h}} & \tilde{\boldsymbol{\nu}} & \tilde{\boldsymbol{\alpha}}_H^t \\ \tilde{\boldsymbol{e}} & \tilde{\boldsymbol{\alpha}}_H & \tilde{\boldsymbol{\varepsilon}} \end{bmatrix} \begin{bmatrix} \bar{S}_{11} \\ 0 \\ 0 \\ 0 \\ 0 \\ 0 \\ 0 \\ 0 \\ 0 \\ 0 \\ 0 \\ 0 \end{bmatrix} \tag{4.10}$$

From 4.10, the following effective coefficients can be computed: $\tilde{C}_{11}$, $\tilde{C}_{12}$, $\tilde{C}_{13}$, $\tilde{C}_{14}$, $\tilde{C}_{15}$, $\tilde{C}_{16}$, $\tilde{h}_{11}$, $\tilde{h}_{12}$, $\tilde{h}_{13}$, $\tilde{e}_{11}$, $\tilde{e}_{12}$, $\tilde{e}_{13}$. Since the magnetostrictive and piezoelectric materials are isotropic transversal, the important coefficients are: $\tilde{C}_{11}$, $\tilde{C}_{12}$, $\tilde{C}_{13}$, $\tilde{C}_{22}$, $\tilde{C}_{23}$, $\tilde{C}_{33}$, $\tilde{h}_{11}$, $\tilde{h}_{22}$, $\tilde{h}_{33}$, $\tilde{e}_{11}$, $\tilde{e}_{22}$, $\tilde{e}_{33}$.

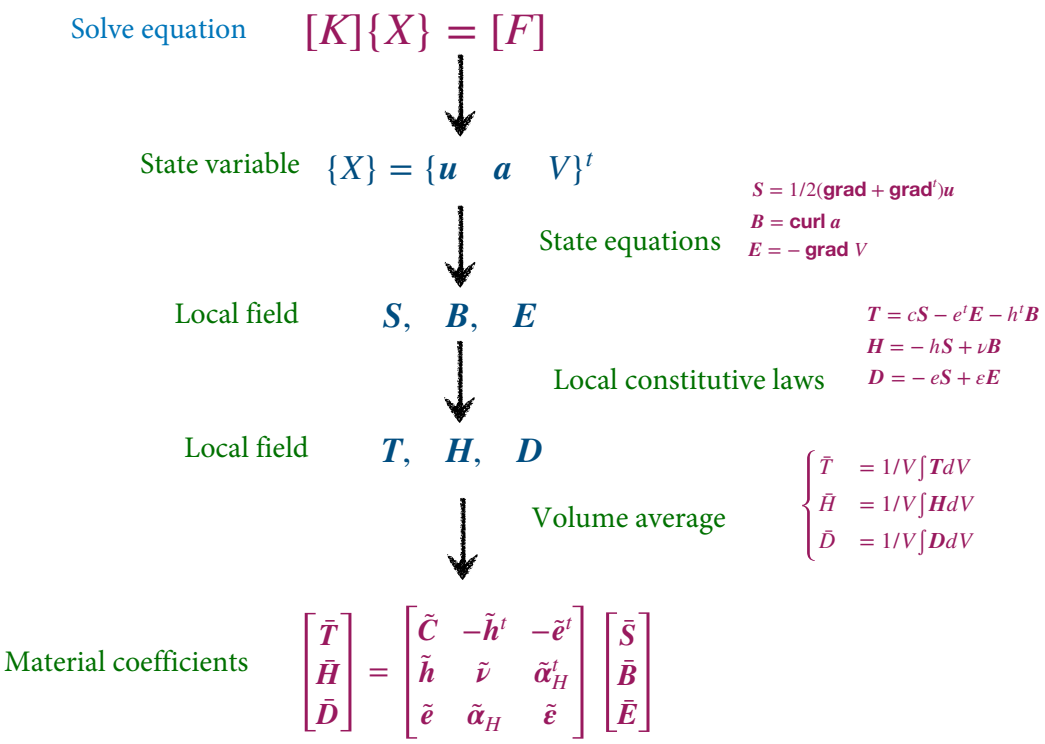

Figure 4.4: Illustration of homogenization procedure

4.3 Homogenization of a cylindrical composite

First, we examine a cylindrical composite (1-3 type) constituted of a magnetostrictive matrix ($CoFe_2O_4$) and piezoelectric fibers ($BaTiO_3$) (Figure 4.5). This composite has been investigated by an analytical method presented in [124], where the material properties of each phase can be found. As we work in the case of linear materials, the cubic REV is studied with the normalized dimension and variable fiber volume fractions.

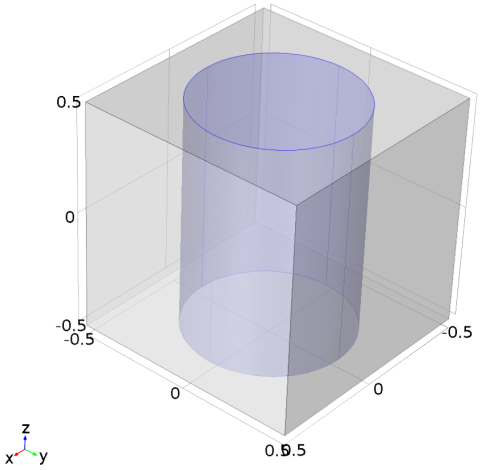

Figure 4.5: Cylindrical composite

Table 4.1: Material properties

	BaTiO3 piezoelectric phase	CoFe2O4 magnetostrictive phase
c_{11} (GPa)	166	286
c_{12} (GPa)	77	173
c_{13} (GPa)	78	170.5
c_{33} (GPa)	162	269.5
c_{44} (GPa)	43	45.3
ε_{11} (C^2/N m^2) x10^{-10}	112	0.8
ε_{33} (C^2/N m^2) x10^{-10}	126	0.93
ν_{11} (m/H) x10^3	200	1.695
ν_{33} (m/H) x10^3	100	6.370
e_{31} (C/ m^2)	-4.4	0
e_{33} (C/ m^2)	18.6	0
e_{15} (C/ m^2)	11.6	0
q_{31} (N/A m)	0	580.3
q_{33} (N/A m)	0	699.7
q_{15} (N/A m)	0	550

Using the proposed FE formulation described in the previous section, the effective proper-

ties of the cylindrical ME composite are evaluated for the range of the fiber volume fraction $f = 0$ to $f = 0.8$. The field excitation of each component of $\boldsymbol{S}$, $\boldsymbol{B}$ or $\boldsymbol{E}$ is respectively applied to determine the average fields $\boldsymbol{T}$, $\boldsymbol{H}$ and $\boldsymbol{D}$, and then the effective coefficients of 4.9. The averaged results of the piezomagnetic coefficient and the magnetoelectric coefficient are compared with the analytical results of [124].

4.3.1 Uniaxial magnetic excitation

Firstly the magnetic field is applied according to two directions X-axis (Figure 4.6) and direction Z-axis (Figure 4.9). Since the magnetic reluctivity of the piezoelectric material is higher than which of the magnetostrictive material, the magnetic induction in magnetostrictive phase is larger. X, Y, Z correspond, respectively, to the indices 1, 2, 3 of matrix representation.

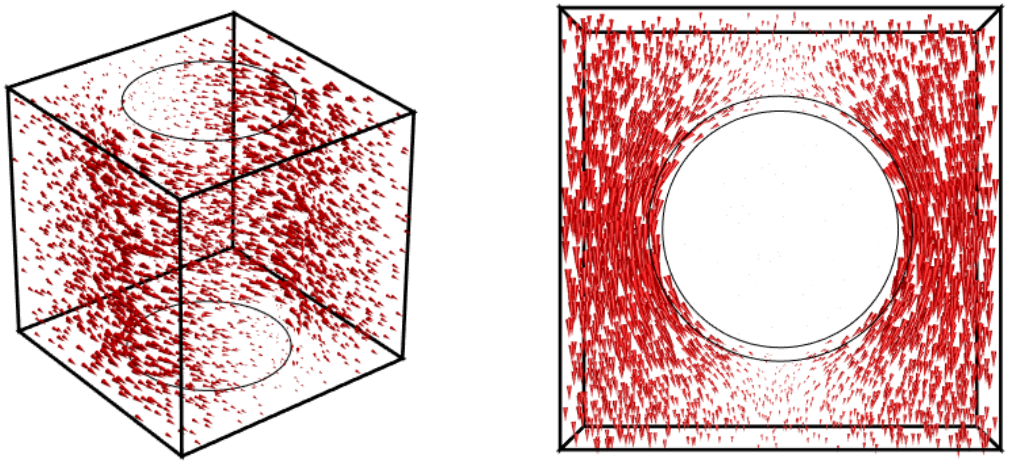

(a) 3D view **(b)** view on plan XY

Figure 4.6: Uniaxial magnetic induction $\bar{B}_1$ is applied

Zero electric field condition is applied, which results in the electric potential and electric field in Figure 4.7. The periodic boundary condition for electric potential is preserved.

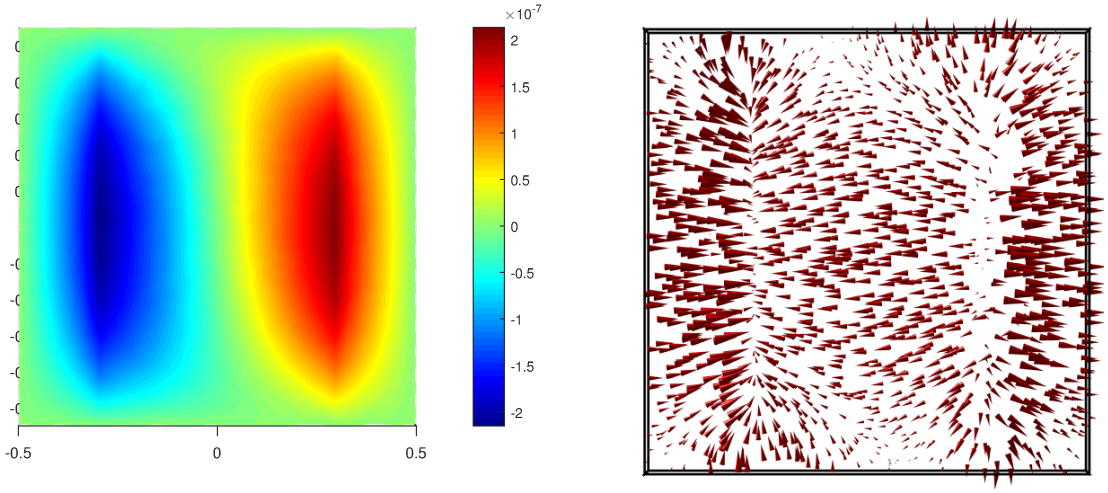

(a) electric potential YZ view

(b) electric filed YZ view

Figure 4.7: Zero boundary condition of electric potential

Since the magnetic induction is applied in X direction, the magnetic field H_1 is oriented in X direction (Figure 4.8).

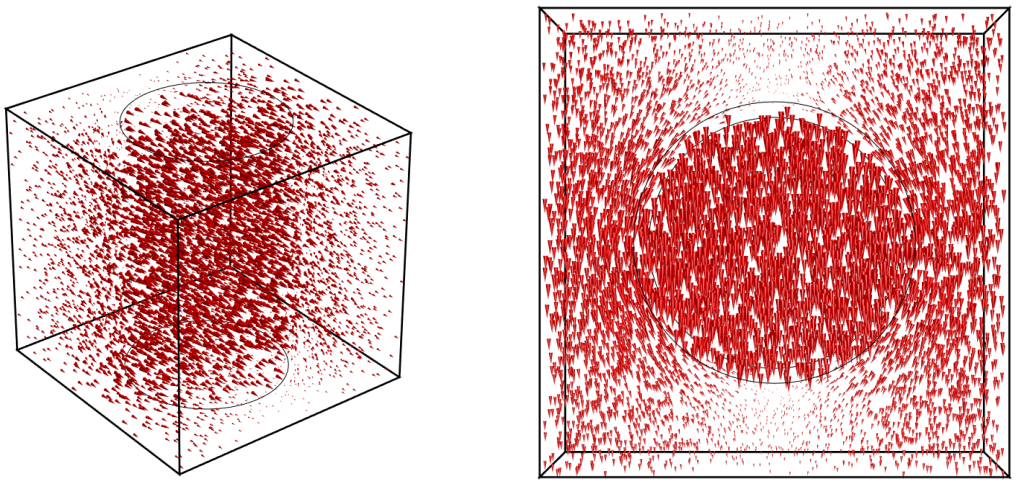

(a) 3D view

(b) View on plan XY

Figure 4.8: Magnetic field H_1 distribution of magnetoelectric composite reinforced by fiber piezoelectric when B_1 is applied

Next, when magnetic induction $\bar{B}_3$ is applied, this induces B_3 distribution of Figure 4.9. Zero electric field condition and periodic condition generate electric potential distribution of Figure 4.10. As a result, magnetic field distribution in Figure 4.11 and electric displacement in Figure 4.12 are obtained.

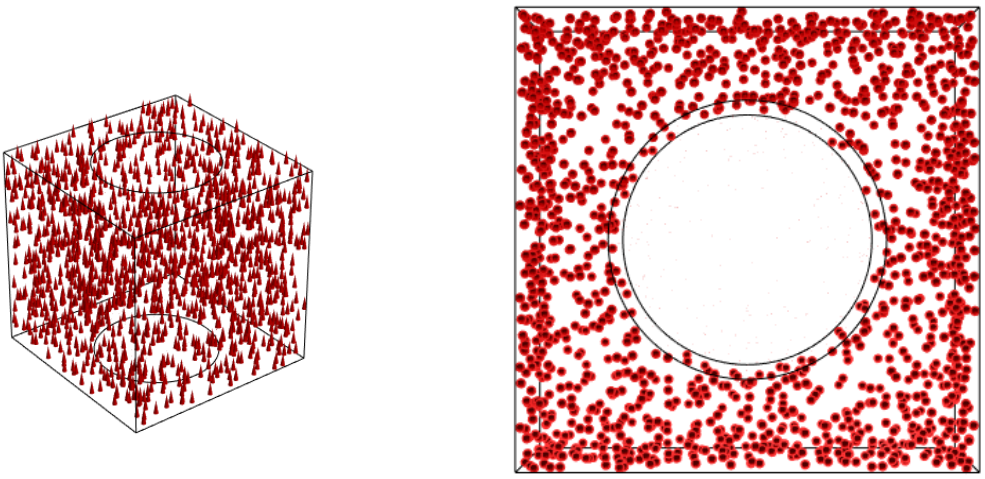

(a) 3D view **(b)** View on plan XY

Figure 4.9: Uniaxial magnetic field B_3 is applied

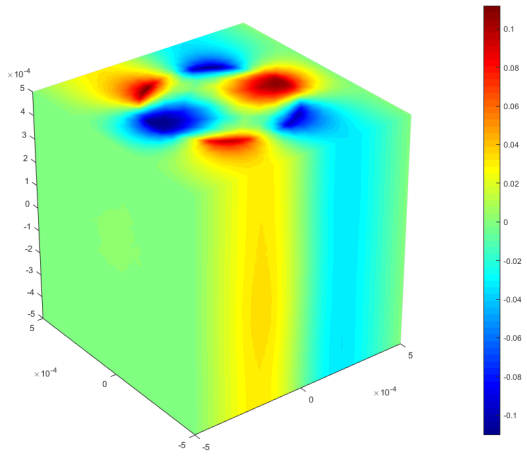

Figure 4.10: Electric potential distribution when magnetic field B_3 is applied

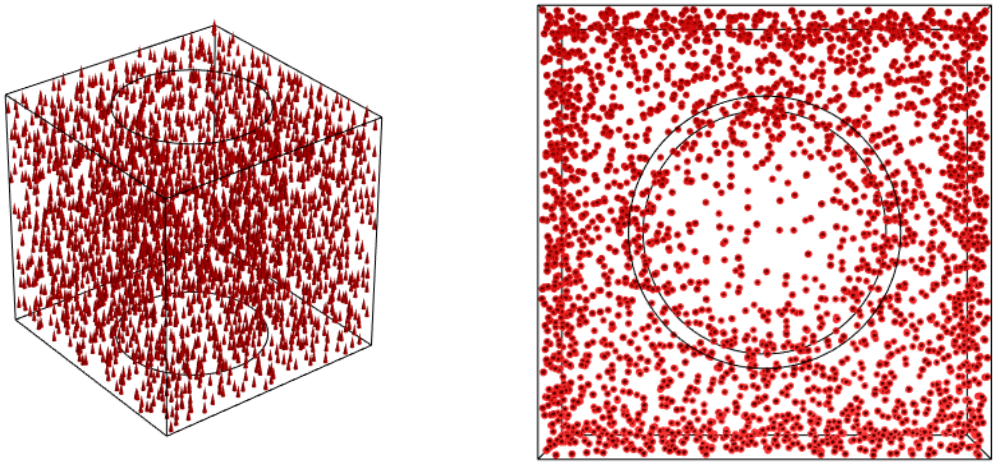

(a) 3D view **(b)** View on plan XY

Figure 4.11: Magnetic field H_3 distribution of magnetoelectric composite reinforced by fiber piezoelectric when B_3 is applied

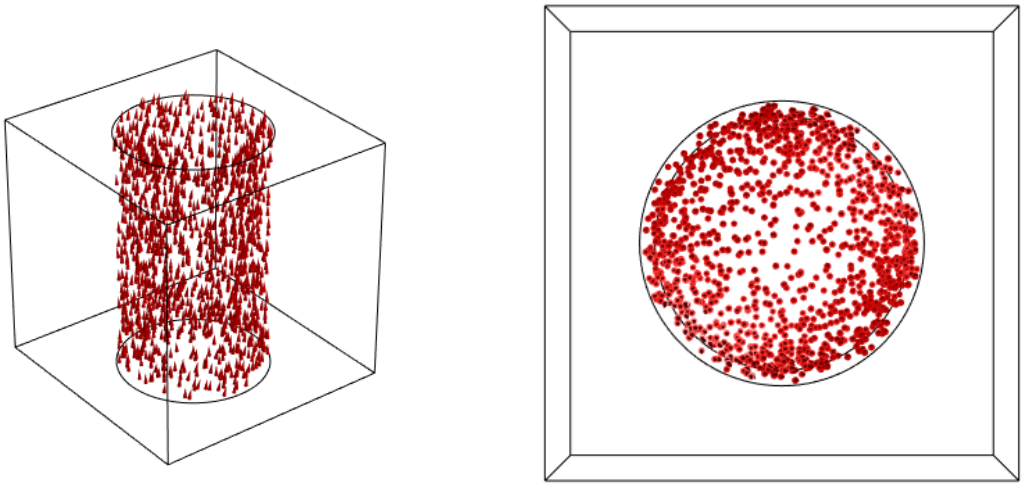

(a) 3D view **(b)** View on plan XY

Figure 4.12: Electric displacement D_3 distribution when B_3 is applied

The following coefficients can be determined:

$$\mu_{11} = \frac{\bar{B}_1}{\bar{H}_1}, \quad \mu_{33} = \frac{\bar{B}_3}{\bar{H}_3}$$

$$q_{11} = \frac{\bar{T}_1}{\bar{H}_1}, \quad q_{33} = \frac{\bar{T}_3}{\bar{H}_3}, \quad q_{31} = \frac{\bar{T}_1}{\bar{H}_3}$$

$$\alpha_{11} = \frac{\bar{D}_1}{\bar{H}_1}, \quad \alpha_{33} = \frac{\bar{D}_3}{\bar{H}_3}$$

Respectively, in Figure 4.13, Figure 4.14 and Figure 4.15, the FE analysis results have shown good agreement with the analytical results. They are also in concordance with the FEM analysis presented in [125]. It can be noticed that, as mentioned before, the macroscopic ME coupling coefficient of the composite shown in Figure 4.15 does not exist in either of the individual phases in the REV.

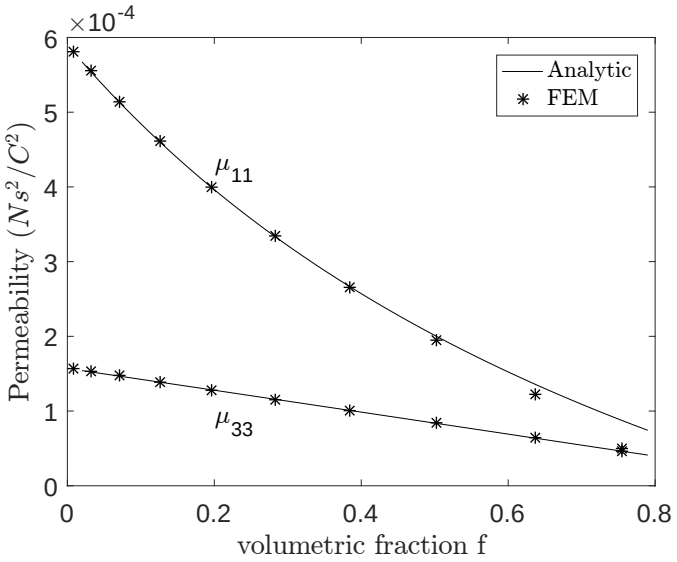

Figure 4.13: Effective permeability as the function of volume fraction f of piezoelectric phase.

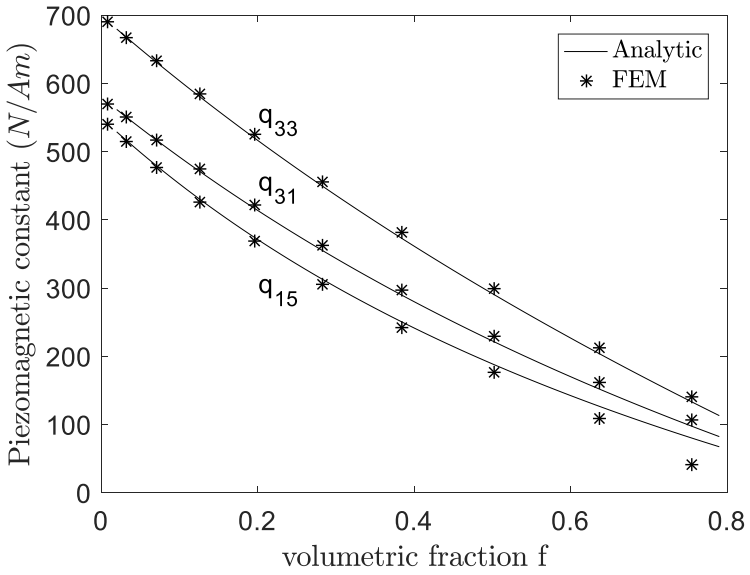

Figure 4.14: Effective piezomagnetic moduli as the function of volume fraction f of piezoelectric phase.

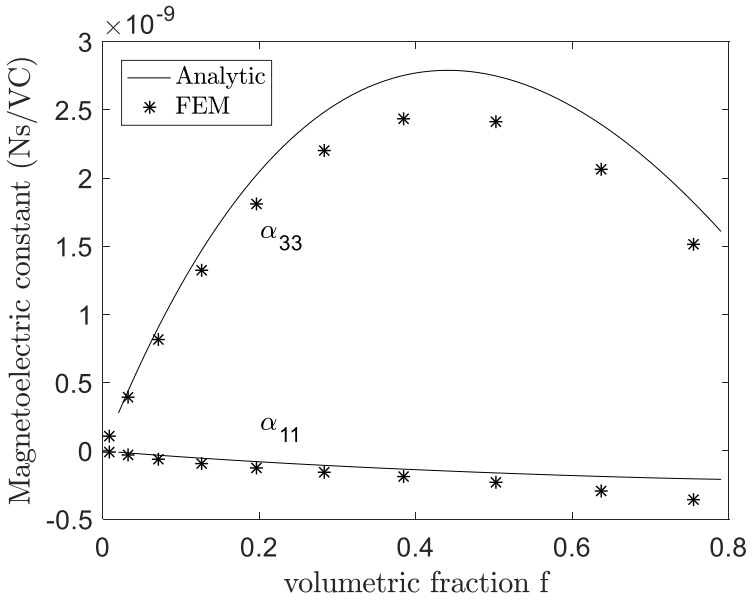

Figure 4.15: Effective magnetoelectric moduli as the function of volume fraction f of piezoelectric phase.

4.3.2 Uniaxial electric excitation

When electric field $\bar{E}_i$ is applied, this induces electric potential distribution (Figure 4.16) and electric field distribution (Figure 4.17, Figure 4.19), which results the electric displacement of Figure 4.18 and Figure 4.20.

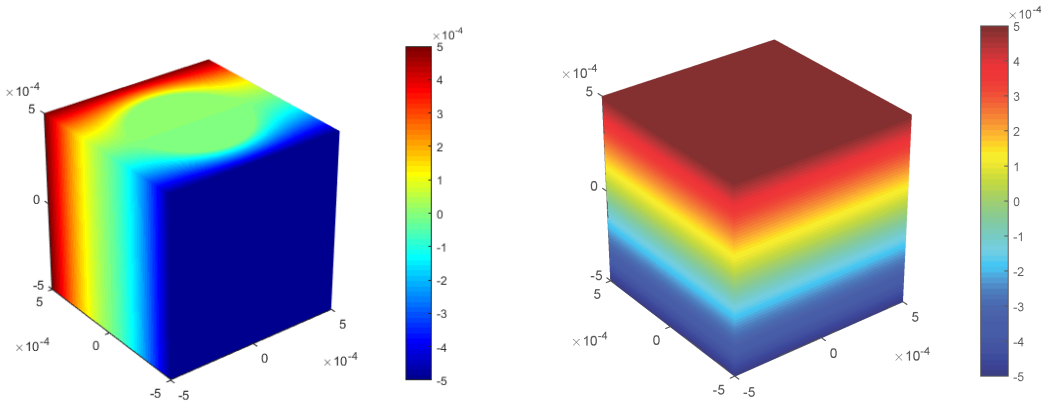

(a) **(b)**

Figure 4.16: Illustration of electric potential when (a) E_1 is applied (b) E_3 is applied

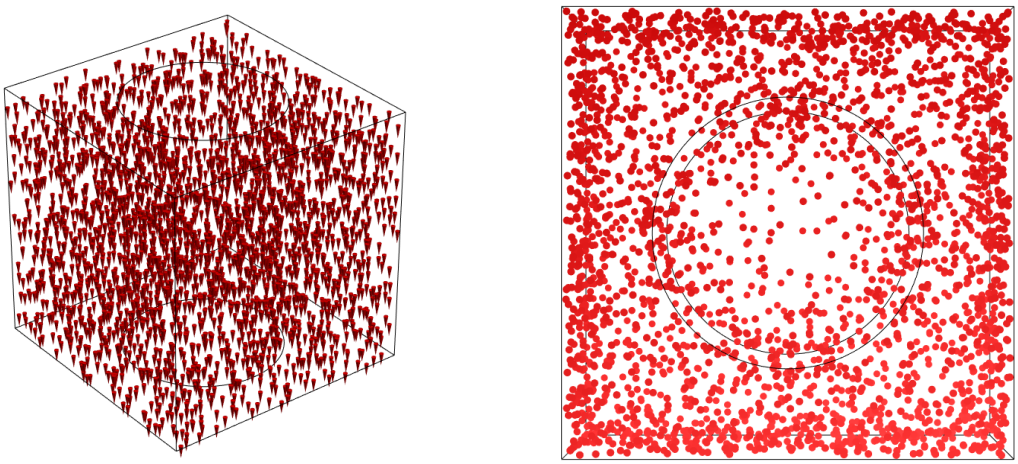

(a) 3D view **(b)** XY view

Figure 4.17: Electric field E_3 is applied

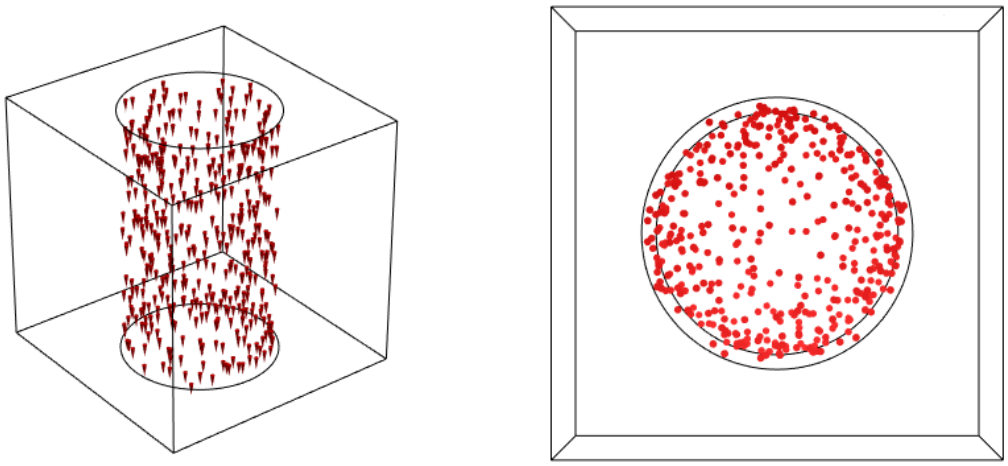

(a) 3D view **(b)** XY view

Figure 4.18: Electric displacement D_3 distribution when E_3 is applied

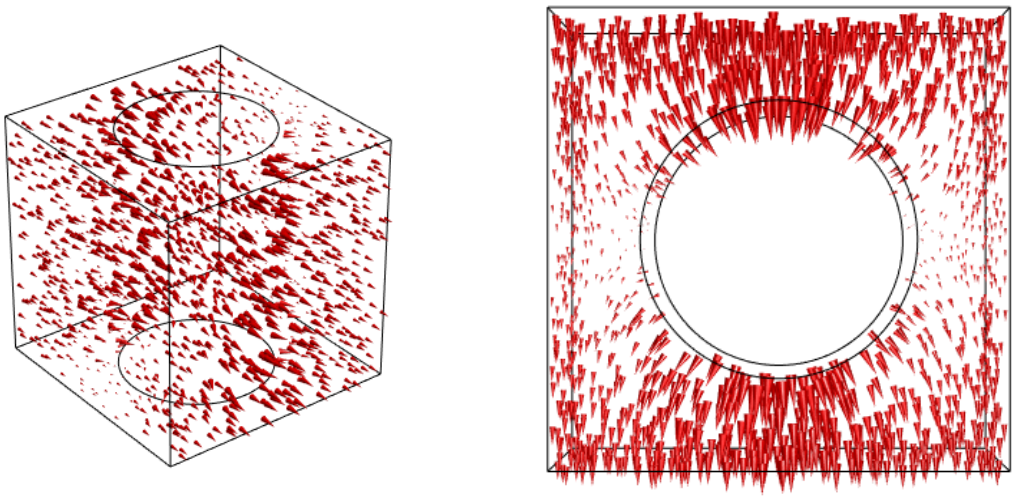

(a) 3D view **(b)** XY view

Figure 4.19: Electric field E_1 is applied

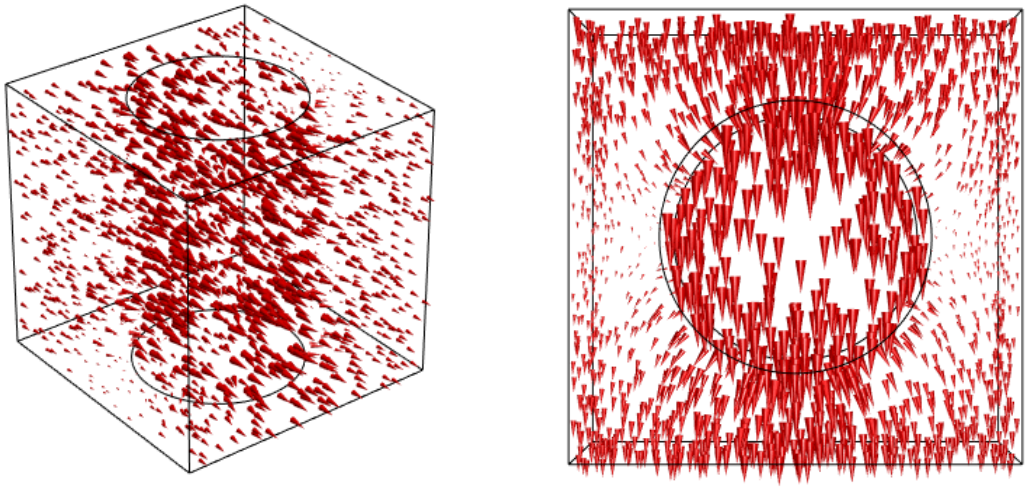

(a) 3D view **(b)** XY view

Figure 4.20: Electric displacement D_3 distribution when E_3 is applied

The following coefficients can be determined:

$$\epsilon_{11} = \frac{\bar{B}_1}{\bar{H}_1}, \quad \epsilon_{33} = \frac{\bar{B}_3}{\bar{H}_3}$$

$$e_{11} = \frac{\bar{T}_1}{\bar{H}_1}, \quad e_{33} = \frac{\bar{T}_3}{\bar{H}_3}, \quad e_{31} = \frac{\bar{T}_1}{\bar{H}_3}$$

As shown in the Figure 4.21 and Figure 4.22, the simulation results are in good agreement with the analytical results in term of piezoelectric constant and permittivity.

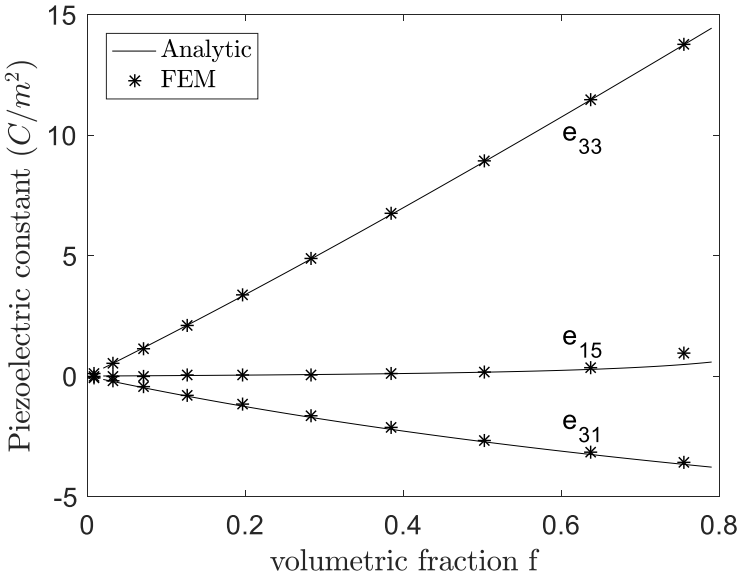

Figure 4.21: Effective piezoelectric moduli as the function of volume fraction f of piezoelectric phase.

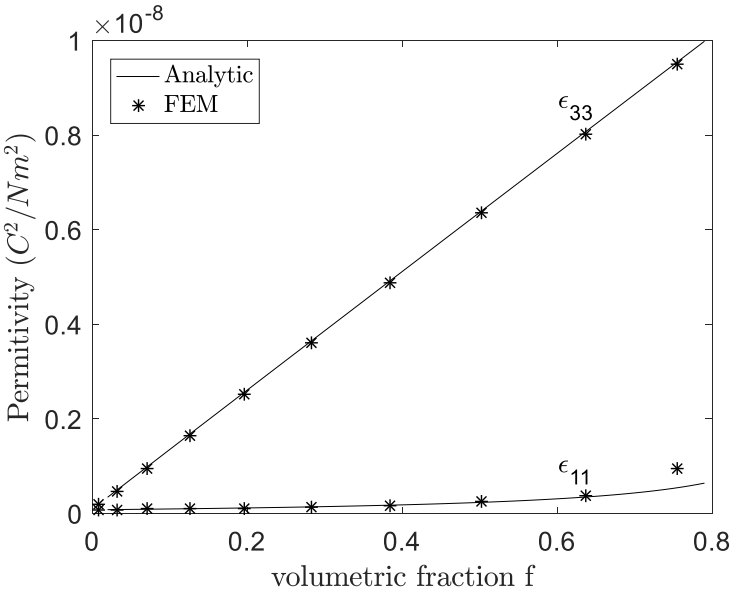

Figure 4.22: Effective permitivity as the function of volume fraction f of piezoelectric phase.

4.3.3 Mechanic excitation

Finally, we apply mechanic displacement to determine the mechanical properties. Figure 4.23 presents the mechanical deformation and the electric field distribution in the REV.

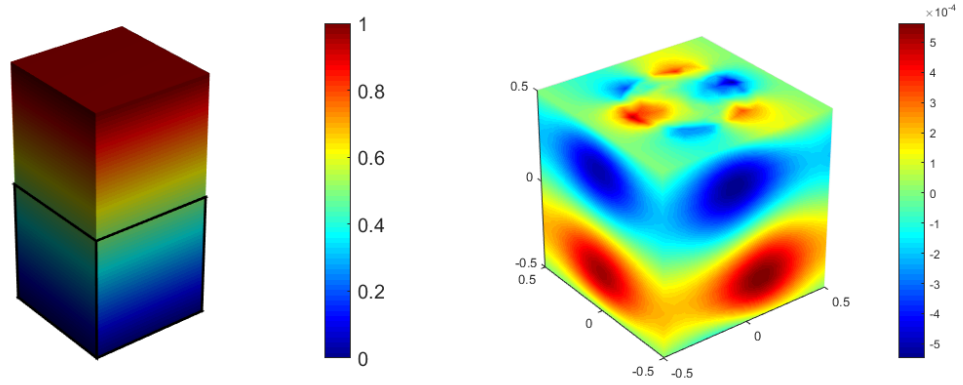

(a) Mechanical deformation **(b)** Electric potential distribution

Figure 4.23: Displacement field U_3 is applied

It is possible to compute the material stiffness

$$c_{ij} = \frac{\bar{T}_j}{\bar{S}_i}$$

Five independent coefficients are evaluated in Figure 4.24

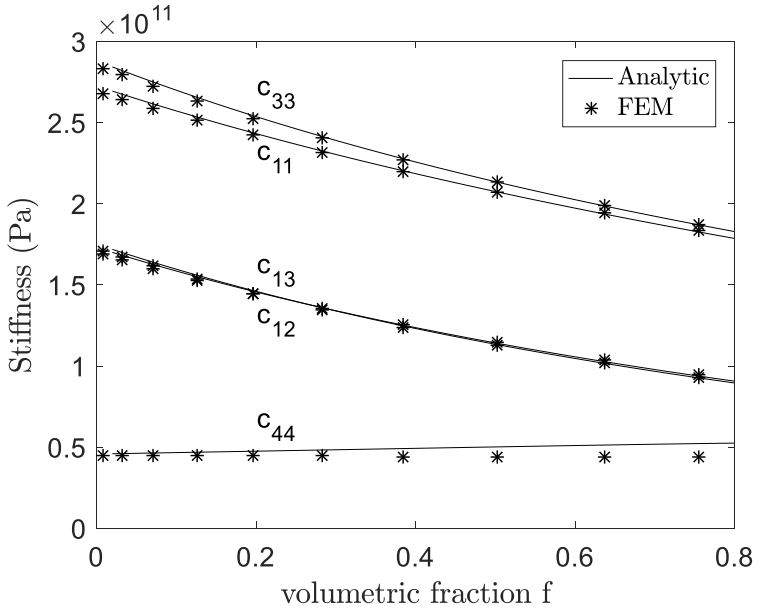

Figure 4.24: Effective stiffness as the function of volume fraction f of piezoelectric phase.

4.4 Homogenization of a cubic inclusion composite

In this section, the magnetoelectric composite in Figure 4.25 made of a piezoelectric matrix (PZT-5A) and cubic magnetostrictive inclusions (Terfenol-D) is considered. For this type of structure, the analytical method is no longer suitable. The FE analysis is applied to investigate the macroscopic properties of this composite. The material properties for Terfenol-D and PZT-5A are given in the Appendix. The ME effective properties are evaluated for the inclusion volume fraction $f = 0$ to $f = 0.9$.

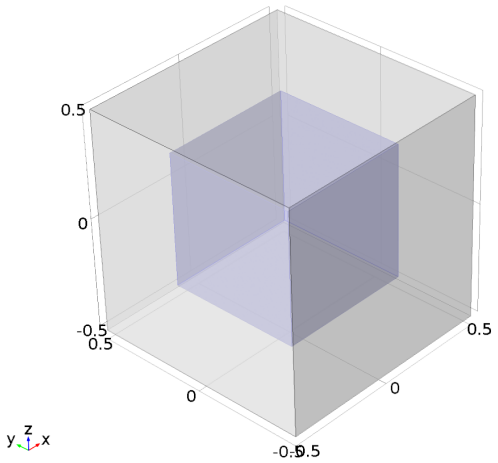

Figure 4.25: The composite with the piezoelectric matrix reinforced by the cubic magnetostrictive inclusion.

To illustrate the field distribution inside of the REV, we take the example of the applied magnetic field component $\bar{H}_3$. Figure 26 shows respectively the magnetic field, the displacement field, the electric field and the electric potential distributions on a cutting plan under this excitation when the volume fraction $f = 0.5$.

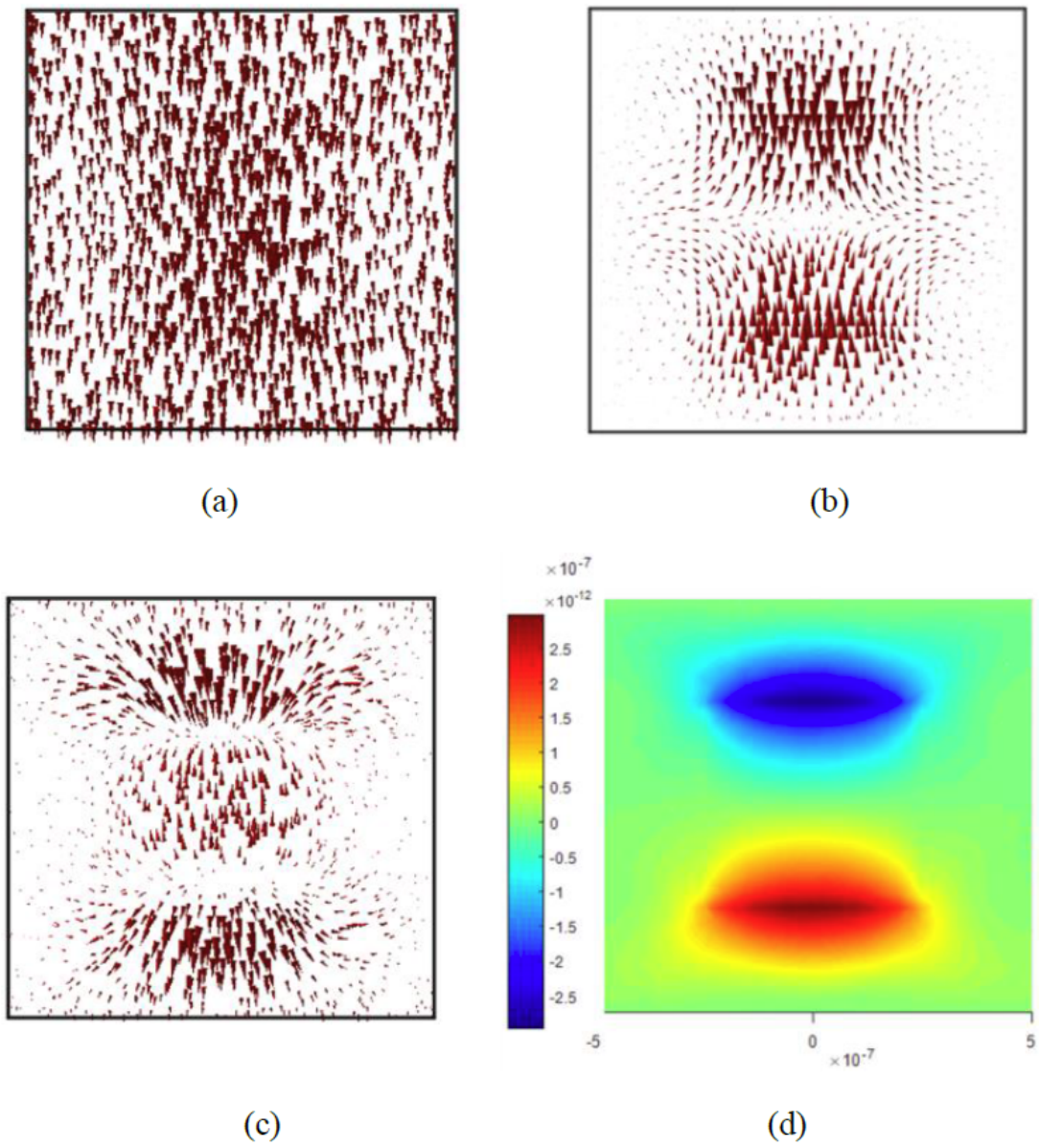

Figure 4.26: The magnetic field (a), displacement field (b) the electric field (c) and the electric potential (d) distributions on a cutting plan when $\bar{H}_3$ is applied.

The dependence of piezomagnetic constant on the volumetric fraction is shown in Figure 4.28. It increases with the volume fraction which is reasonable as this property exhibits only in magnetostrictive phase. The effective value is almost linear with the volume fraction. The dependence of the ME effective coefficient on the inclusion volume fraction is shown in Figure 4.29. The maximum value of ME constant α_{11} is reached at the volume fraction $f = 0.47$. This analysis allows in addition the determination of the optimal volume fraction of the composite to guide the fabrication of the composite.

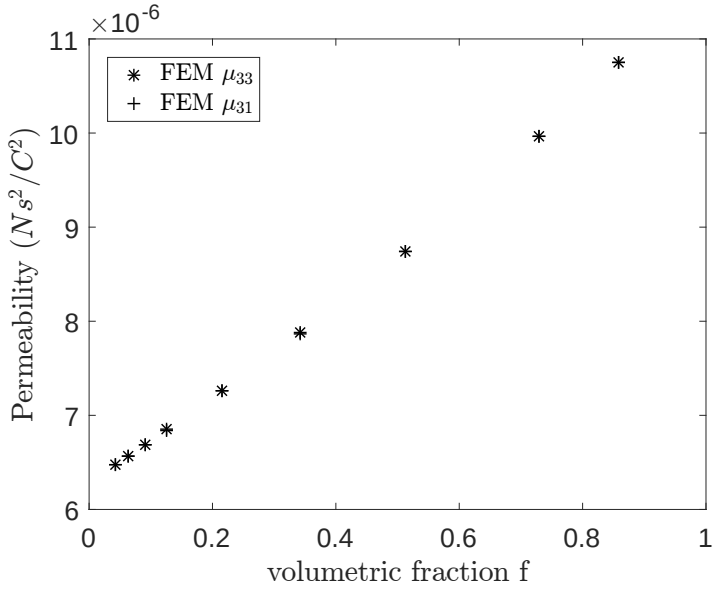

Figure 4.27: The permeability as a function of volumetric fraction.

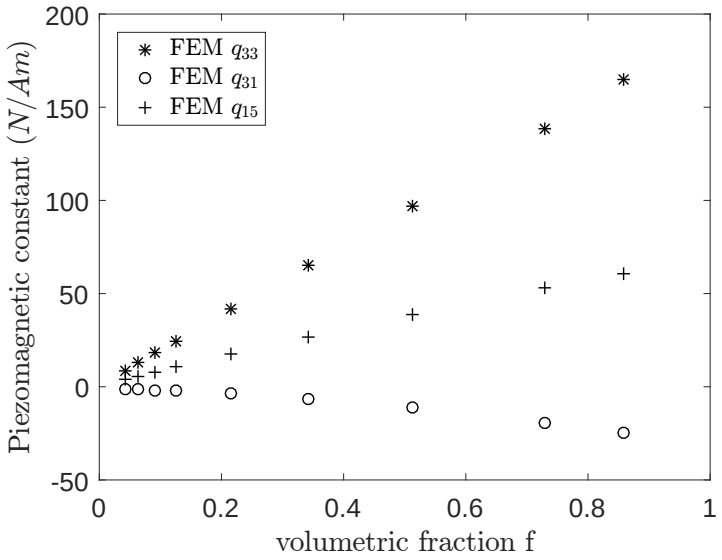

Figure 4.28: The piezomagnetic constant as a function of volumetric fraction.

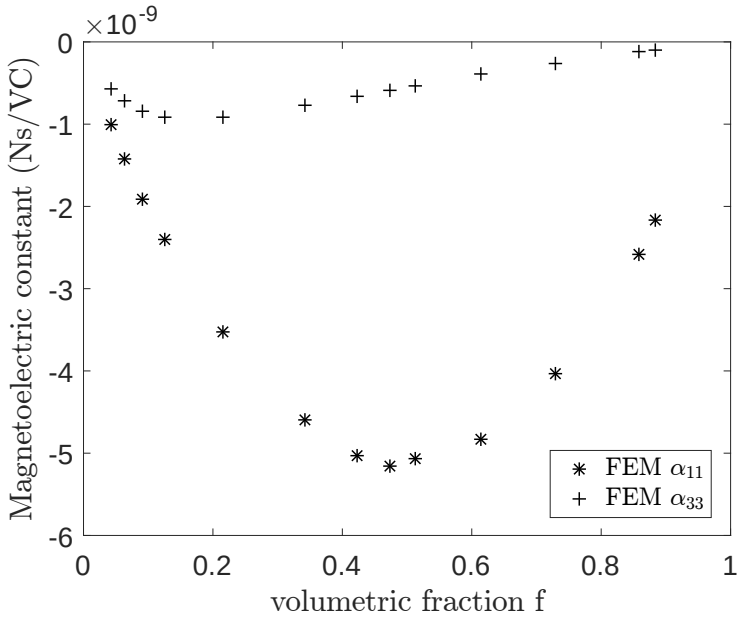

Figure 4.29: The magnetoelectric constant as a function of volumetric fraction.

Next, the example of applying an electric $\bar{E}_3$ is considered. The electric potential distribution, the results of electric field and electric displacement are presented in Figure 4.30. The piezoelectric constant and the permittivity can be evaluated.

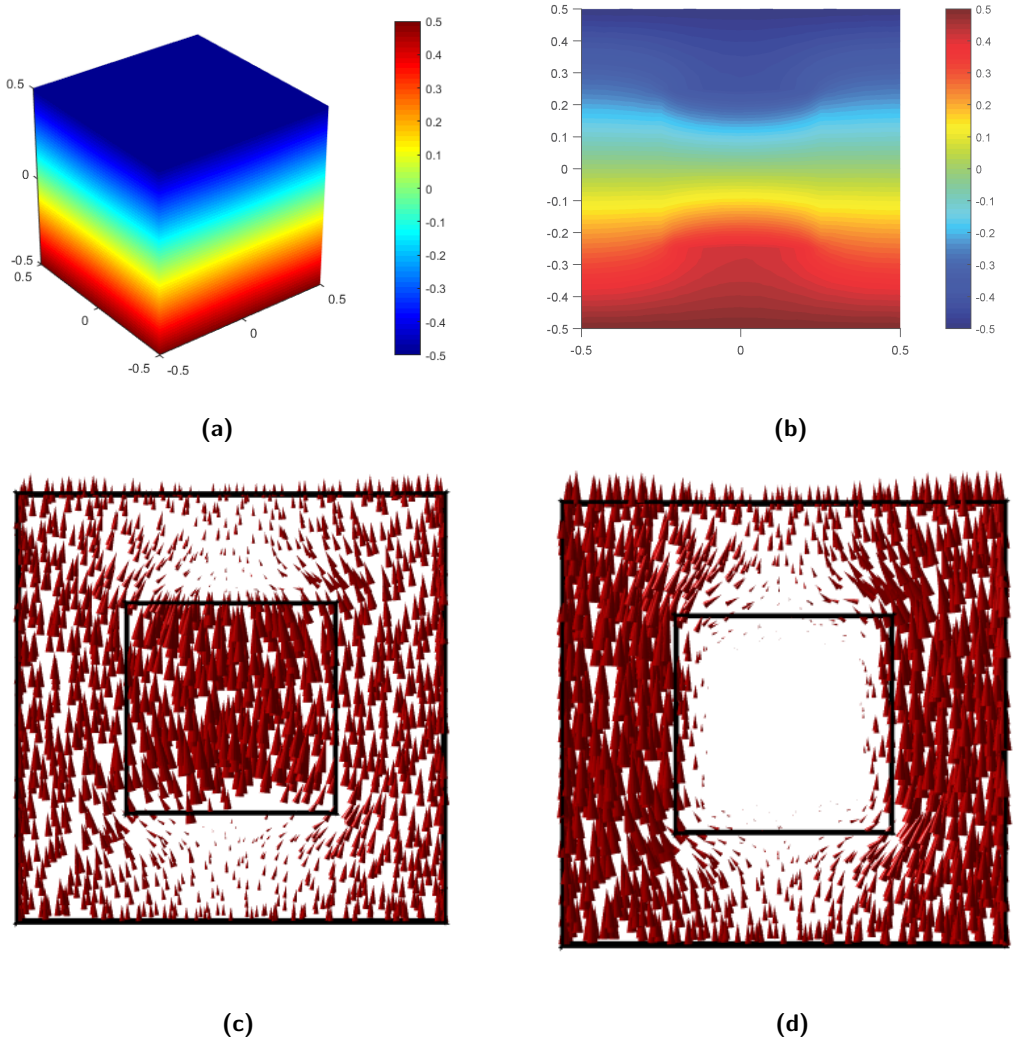

Figure 4.30: The electric potential 3D view (a), electric potential on cutting plane (b) the electric field (c) and the electric displacement (d) distributions on a cutting plan when $\bar{E}_3$ is applied.

The electric properties of this structure are given in Figure 4.31 and Figure 4.32. In opposition of the magnetic properties, the electric constants decrease when the volume fraction increase as the piezoelectric volume decreases.

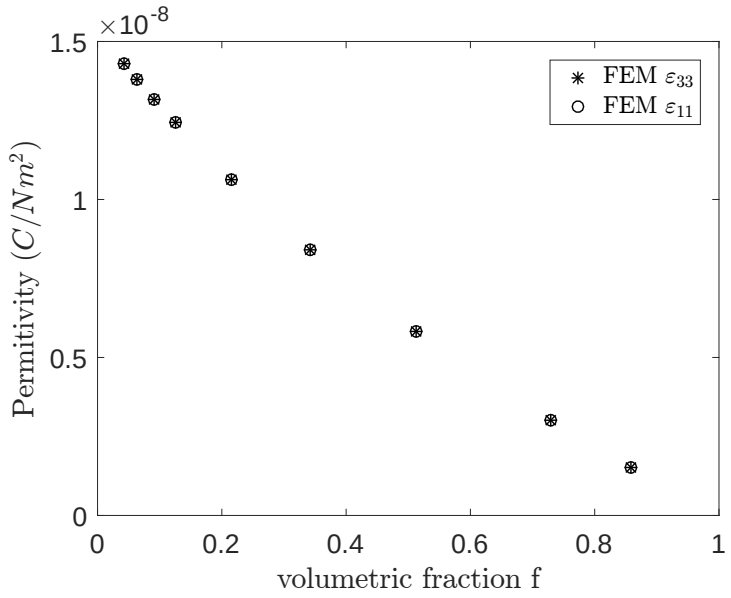

Figure 4.31: The effective permitivity as a function of volumetric fraction.

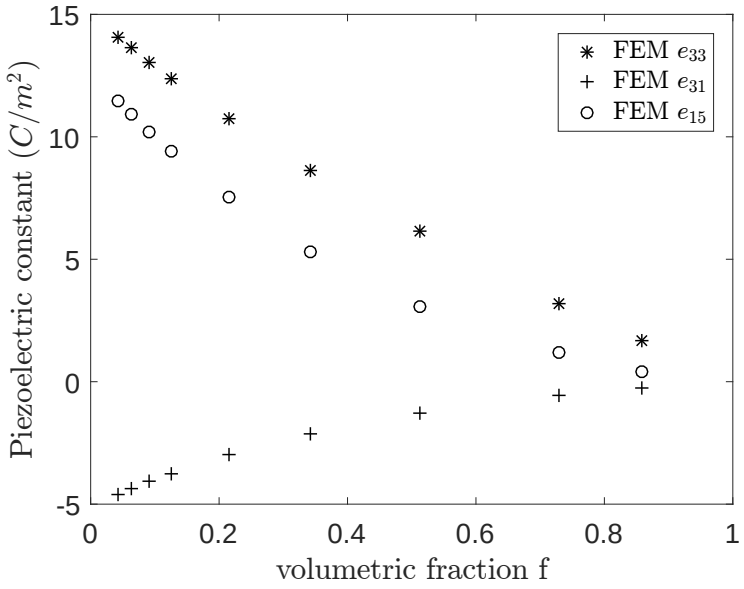

Figure 4.32: The piezoelectric effective as a function of volumetric fraction.

4.5 Nonlinear magnetostrictive analysis

In this section, the behavior of magnetostrictive composite under large signal static magnetic excitation is performed. Taking into account the nonlinear magnetostriction, the piecewise linear approach, which have been presented in chapter 2, is implemented in

FEM and homogenization procedure. Since the magnetic excitation is divided into small step, the local constitutive law (in Figure 4.4) is still linear.

We consider an example presented in [127] of Terfenol-D/glass composite (Figure 4.33). The Terfenol-D, which is sphere inclusion, is in the matrix to improve its mechanical properties.

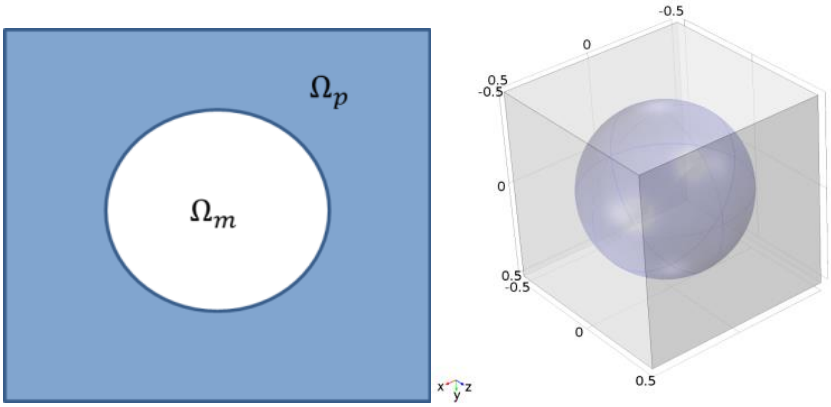

Figure 4.33: Magnetostrictive composite structure.

In Figure 4.34, the FEM results show qualitatively a good agreement with experiment in [128]. Next, we apply to Terfenol-D/Epoxy composite, the same effect as analytical in [127] is obtained Figure 4.35.

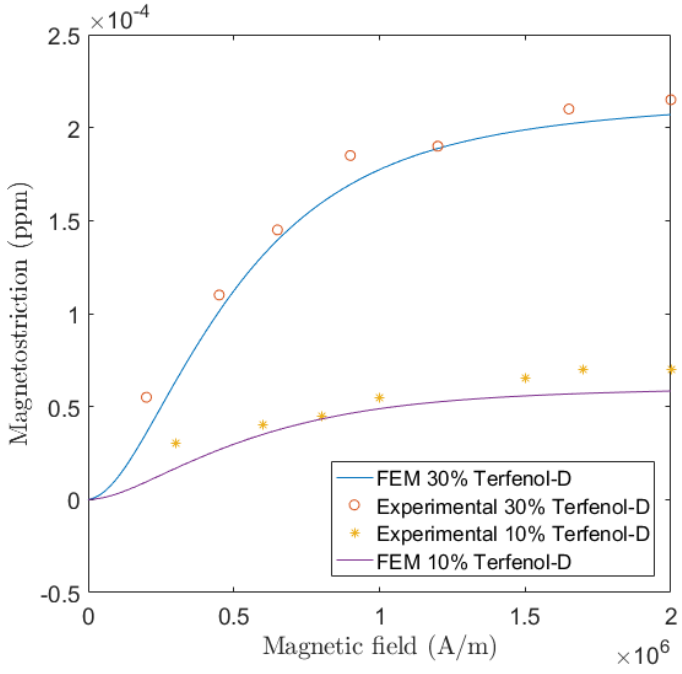

Figure 4.34: Magnetostrictive composite structure.

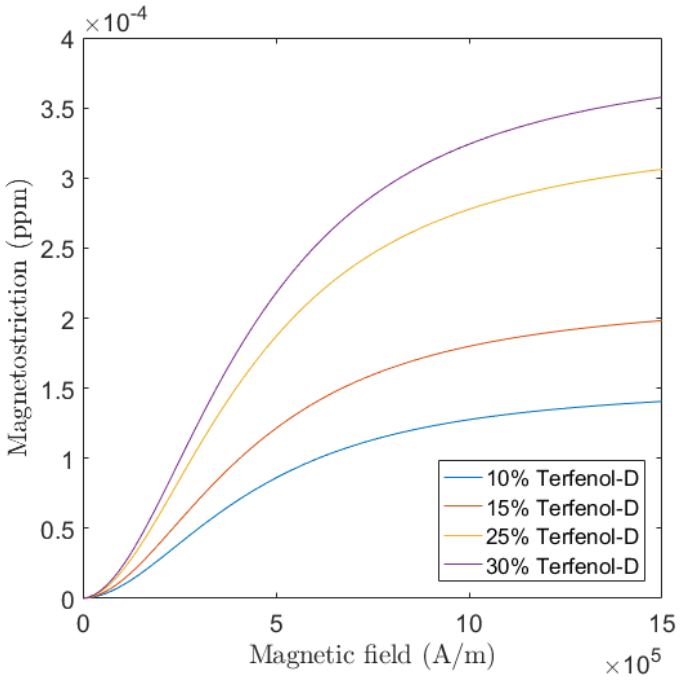

Figure 4.35: Magnetostrictive composite structure.

4.6 Dynamic analysis

In this section, the method is applied to perform the behavior of ME composite under small magnitude of dynamic excitation. The eddy current term is added in the coupled physics equations. In the homogenization procedure, the local fields are averaged to get the effective properties of REV in macroscopic scale. The periodic conditions for unknown variables are applied on the boundary of the REV. The final system in harmonic regime is obtained by expressing $\frac{\partial}{\partial t} \rightarrow iw$:

$$[\boldsymbol{K}]\{X\} = [F] \tag{4.11}$$

with $\{X\} = \{\mathbf{u},\ \mathbf{a},\ \psi\}^t$, $[F] = \{0,\ \Sigma_i \bar{a}_i,\ 0\}^t$ and

$$[\boldsymbol{K}] = \begin{bmatrix} -\omega^2 \boldsymbol{M}_{uu} + i\omega \boldsymbol{C}_{uu} + \boldsymbol{K}_{uu} & -\boldsymbol{K}_{au}^t & i\omega \boldsymbol{K}_{u\psi} \\ -\boldsymbol{K}_{au} & i\omega \boldsymbol{C}_{aa} + \boldsymbol{K}_{aa} & i\omega \boldsymbol{C}_{a\psi} \\ i\omega \boldsymbol{K}_{u\psi}^t & i\omega \boldsymbol{C}_{a\psi}^t & i\omega \boldsymbol{C}_{\psi\psi} + \omega^2 \boldsymbol{K}_{\psi\psi} \end{bmatrix}$$

The piezoelectric matrix reinforced by cube magnetostrictive inclusion and the magnetostrictive matrix reinforced by fiber piezoelectric are, respectively, examined. These composites are introduced in section 4.3 and 4.4. We consider a REV of 1 mm with the frequency vary from 1 Hz to 10 MHz.

For the cube magnetostrictive inclusion, the magnetic field H_3 and the eddy current distribution at 300 kHz and 3 MHz are presented respectively in Figure 4.36 and Figure 4.37. At higher frequency, the magnetic field and the current density are larger near the interface between magnetostrictive and piezoelectric because of the skin effect.

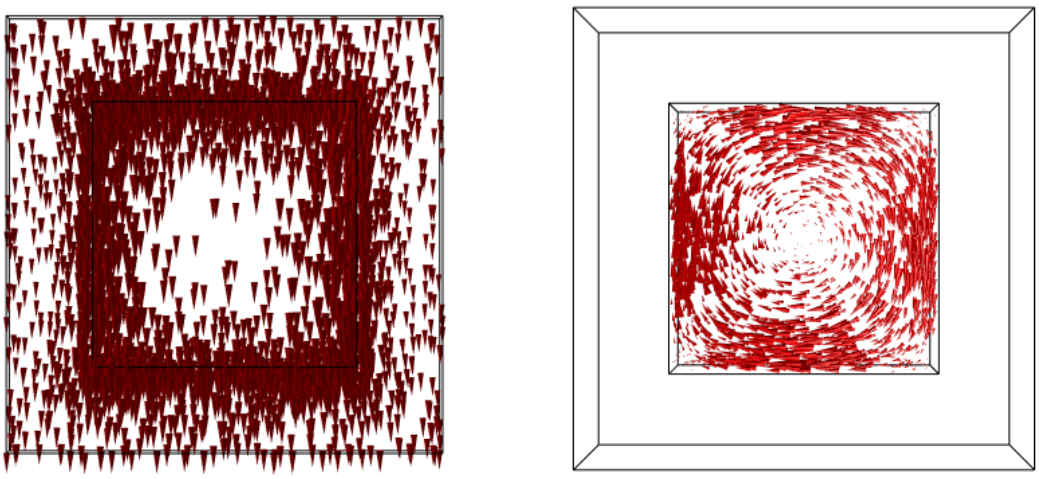

(a) (b)

Figure 4.36: Magnetic field (a) and eddy current (b) @ 300kHz

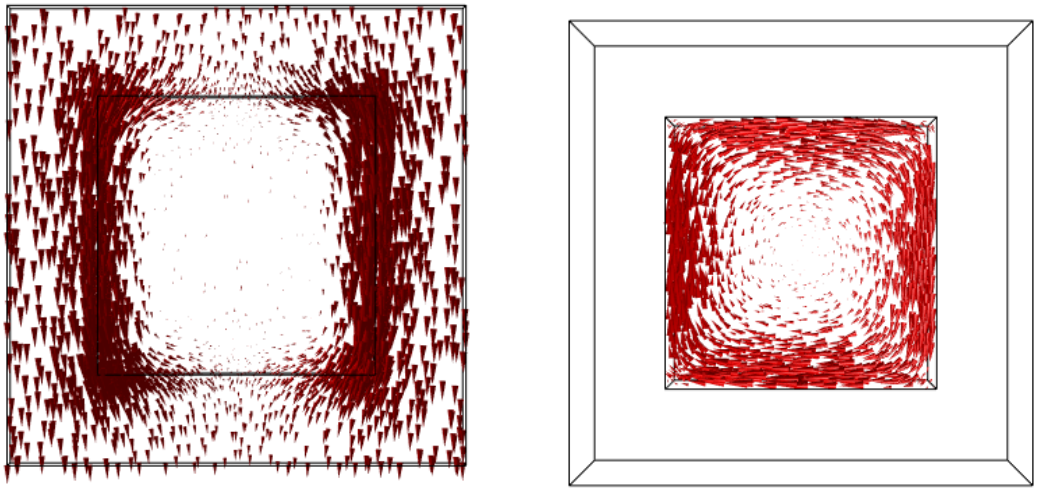

(a) (b)

Figure 4.37: Magnetic field (a) and eddy current (b) @ 3 MHz

Figure 4.38 shows the frequency dependence of magnetoelectric effective constant for the REV of ME composite with cube magnetostrictive inclusion. The influence of eddy current can be observed from 20kHz.

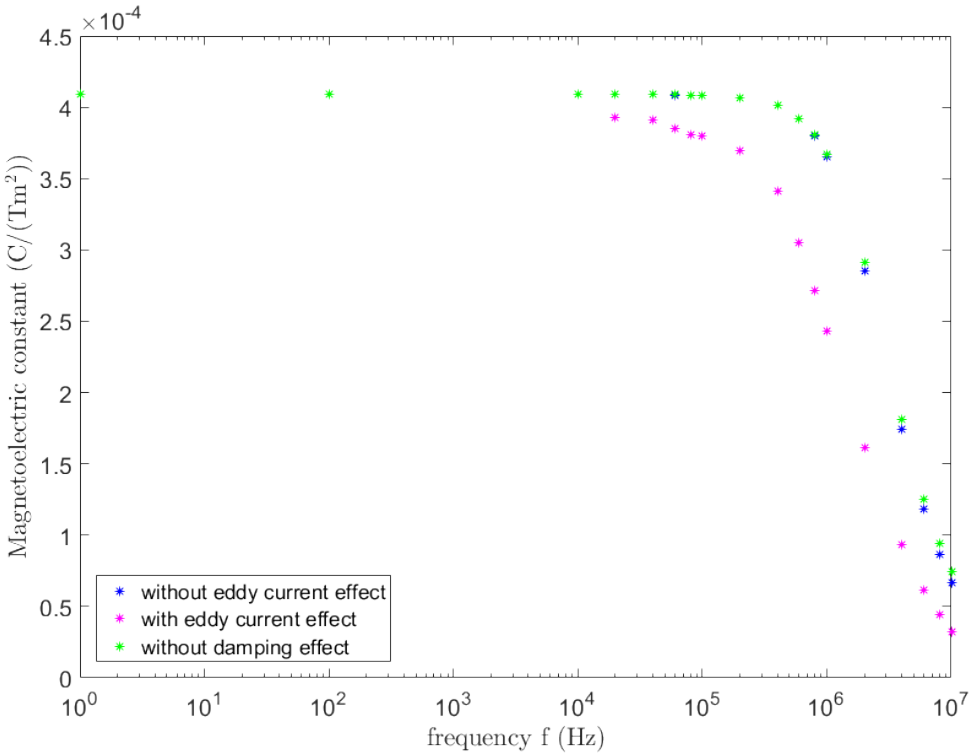

Figure 4.38: The effective magnetoelectric as a function of frequency.

For magnetostrictive matrix reinforced by fiber piezoelectric material, the current density is larger at four corners of the REV when the frequency increases, as shown in Figure 4.39,

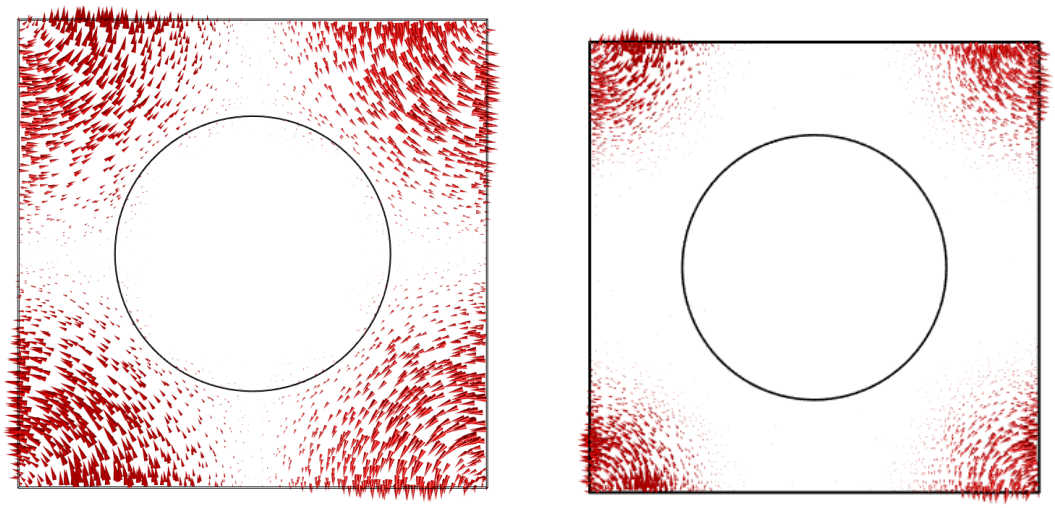

(a) 120 kHz **(b)** 1.5 MHz

Figure 4.39: Eddy current

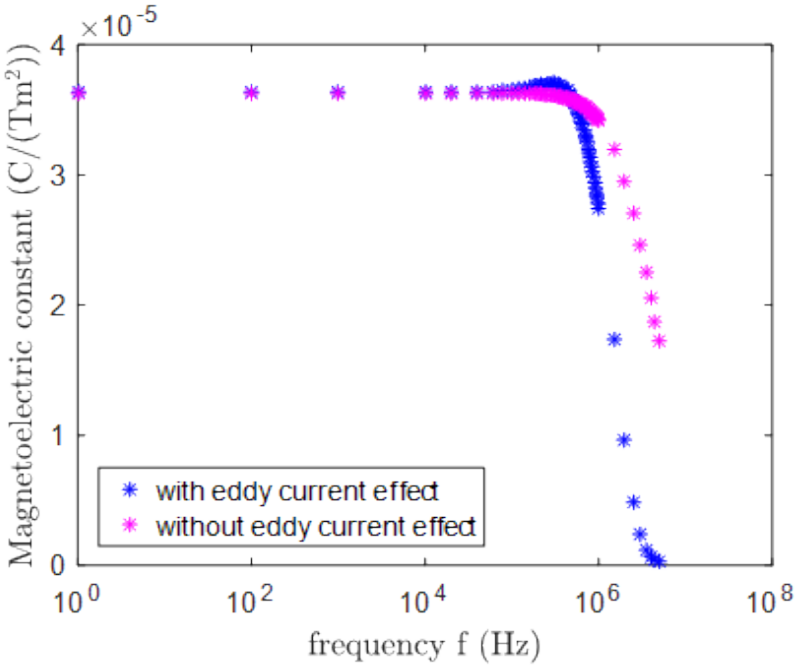

Figure 4.40: The effective magnetoelectric as a function of frequency.

The frequency dependence of magnetoelectric effective constant for the REV of ME composite with fiber piezoelectric material is presented in Figure 4.40. The eddy current effect is observed at higher frequency ($\approx$ 100 kHz).

4.7 Conclusion

In this chapter, the FE multiphysics analysis is applied to investigate the REV of ME composites to determine the effective properties by using the periodic boundary conditions. The homogenized composite exhibits a macroscopic ME coupling although the piezoelectric and the magnetostrictive phases which does not exist in local scale. The model is validated in comparison with the analytical method in a cylindrical inclusion composite. It was further extended to homogenize the cubic magnetostrictive inclusion composite. This analysis allows also the optimization of the volume fraction of the composites. We implement DEAM into the FEM and the homogenization procedure to analyze the nonlinear behavior of magnetostrictive material. Finally, the proposed method has been extended to the dynamic case to investigate the REV under the dynamic regime.

Chapter 5

Conclusion and perspective

Numerical modeling of active materials is rapidly developing to meet the needs for improvement of existing devices or the implementation of innovative systems. Several approaches (equivalent circuit method, homogenization, etc.) are possible. In this context, it is essential to have a robust tool which can take into account the influence of mechanical, magnetic and electric aspects to the performance of materials.

The objective of this thesis is to develop a 3D finite element multiphysics model for magnetic-mechanic-electric coupling based on the 3D analysis tool for magnetostrictive materials and piezoelectric material existing at the L2E laboratory. This method is developed to investigate different magnetoelectric composite structures under static to dynamic regimes and from the large to small signals.

From the application point of view, the magnetoelectric (ME) composite with the capacity of transforming the magnetic energy to electric energy attracts the scientific interest. Generating significantly ME coefficient at resonance, this material can be applied for magnetic sensor, inductor, energy transducer... In our laboratory, we are interested in using the ME material for energy harvesting. The purpose is responding to power demand of connected objects embedded in electronic devices. It is important that the composite performs efficiently and provide a significant ME coefficient with dimensions from mm to μm.

At the formulation step, the multiphysic model is established from Maxwell equations and mechanical equilibrium equation. Next, we introduced the multiphysic constitutive laws describing the magnetic-mechanic and mechanic-electric coupling. Applying the finite elements method (FEM), the Whitney edge elements have been applied to discretize the magnetic vector potential. Utilizing the edge elements for the magnetic vector potential allows us to compute the eddy currents, so that their effect on the material performance in dynamic regime could be considered. Under large signal, due to non-homogeneity and nonlinear behavior of magnetostrictive materials, we implemented the discrete energy averaged model (DEAM) to describe the nonlinearity. The nonlinear procedure is divided step by step adopting the piecewise linear strategy. In a iterative procedure, the FEM results were utilized to extract inputs (state variables magnetic field, tress) for DEAM, whereas the DEAM results were employed for matrices assembling of FEM. In brief, the 3D model can perform nonlinear static analysis of composite ME and the linear harmonic analysis.

We used this model to investigate foremost the behavior of ME laminate composite. Firstly, the laminate with circular section is considered. The calculations of the output voltage and the power have been shown. In linear harmonic analysis, the resonance frequency can be observed and the influence of eddy currents on magnetostrictive layers is included. In addition, the distributions of the magnetic field, the electric field, the mechanic deformation, the magnetic induction, the electric displacement, the stress field are reported in 3D. The simulation results have shown suitable agreement with the measurement in the reference. The difference can be the effect of the resin Epoxy, the effect of damping. Two functional modes have been examined to find a more efficient configuration. Secondly, the laminate with rectangular section is examined. The simulation results are compared with the experimental results in our laboratory. Finally, thanks to the 3D, we have studied the influence of geometry on ME coefficient output. From this work, we have proposed a novel structure which can improve the material performance.

Next, the non-homogeneous composite is analyzed. To overcome the limit of FEM which requires expensive computation time on meshing the tiny particulate or fiber structure, the homogenization theory is applied. We have performed the finite element analysis on a representative elementary volume and implement the homogenization procedure afterwards. At first, the ME fiber composite is considered. Six effective coefficients have been computed, the simulation results shown a good agreement with the analytical results. After that, we extended this approach to ME composite laminate with cubic inclusion. The nonlinear magnetostrictive analysis and the dynamic analysis are performed in order to study the capacity and the influence of eddy currents on the behavior of the composite particulate and fiber composites.

In the meanwhile, some perspectives to this work are suggested as following:

- In the modeling aspect, DEAM was employed to describe the nonlinear behavior of the magnetostriction. However, this model requires many parameters and time computation. Other formulations for characterizing nonlinear magnetostrictive materials can be tested. The effect of the resin Epoxy can be investigated. Furthermore, the effect of mechanical damping and eddy currents need to be properly examined. We can consider low frequency at first, the effect of eddy currents is neglected and we study the mechanical damping. When we have the coefficient for this effect, the effect of eddy currents will be considered at higher frequency.

- From the computational aspect, the FEM is versatile and able to provide detailed visualization in the simulated system. However, this approach also demands more computing resources, especially in cases of transient and parametric analysis. In order to preserve advantages of FEM while reduce time computation and memory requirement, the model order reduction can be considered, for example, by the proper generalized decomposition method. Moreover, the Matlab solver finds rapidly solution for a matrix of $10^5 \times 10^5$ but very slow for $10^6 \times 10^6$ matrix. A robust method for solving large matrix equation is needed.

- Some works can be proposed to improve the performance of ME materials: analyze the response of ME materials at dynamic regime under larger amplitudes of signals, study experimentally the influence of geometry parameters for novel structures, con-

sider different ME structures like disk-ring ME composite, investigate the energy extraction circuit based on ME material to improve energy harvesting.

Appendix A

Formulation

A.1 Voigt notation

The most well-known of the matrix formalisms for anisotropic elasticity is Voigt notation. The stress and strain tensors are written as follows:

$$\boldsymbol{T} = \begin{bmatrix} T_1 = T_{11} \\ T_2 = T_{22} \\ T_3 = T_{33} \\ T_4 = T_{23} \\ T_5 = T_{31} \\ T_6 = T_{12} \end{bmatrix} \qquad \boldsymbol{S} = \begin{bmatrix} S_1 = S_{11} \\ S_2 = S_{22} \\ S_3 = S_{33} \\ S_4 = 2S_{23} \\ S_5 = 2S_{31} \\ S_6 = 2S_{12} \end{bmatrix}$$

Thanks to the introduction of coefficients in 2 equation above, the Hooke's law

$$T_{ij} = \mathbb{E}_{ijkl} S_{kl}$$

Can be represented in matrix form

$$\boldsymbol{T} = [c]\boldsymbol{S}$$

where:

$$[c] = \begin{bmatrix} c_{11} & c_{12} & c_{13} & c_{14} & c_{15} & c_{16} \\ c_{12} & c_{22} & c_{23} & c_{24} & c_{25} & c_{26} \\ c_{13} & c_{23} & c_{33} & c_{34} & c_{35} & c_{36} \\ c_{14} & c_{24} & c_{34} & c_{44} & c_{45} & c_{46} \\ c_{15} & c_{25} & c_{35} & c_{45} & c_{55} & c_{56} \\ c_{16} & c_{26} & c_{36} & c_{46} & c_{56} & c_{66} \end{bmatrix}$$

There is a perfect coincidence between $\mathbb{E}_{ijkl}$ and the c_{pq}. However, for the inverse of Hooke's law

$$S_{ij} = \mathbb{Z}_{ijkl} T_{kl}$$

In matrix form $\boldsymbol{S} = [s]\boldsymbol{T}$ so :

$$[s_{ij}] = \begin{bmatrix} Z_{ppqq} & 2Z_{pprs} \\ sym & 4Z_{pqrs} \end{bmatrix}$$

A.2 Matrix representation

The coefficients of coupling as e, h, d are in (6x3) matrix form:

$$[d] = \begin{bmatrix} d_{11} & d_{12} & d_{13} & d_{14} & d_{15} & d_{16} \\ d_{12} & d_{22} & d_{23} & d_{24} & d_{25} & d_{26} \\ d_{13} & d_{23} & d_{33} & d_{34} & d_{35} & d_{36} \end{bmatrix}$$

For the uncoupling coefficients μ, ε the matric form is (3x3):

$$[\mu] = \begin{bmatrix} \mu_{11} & \mu_{12} & \mu_{13} \\ \mu_{12} & \mu_{22} & \mu_{23} \\ \mu_{13} & \mu_{23} & \mu_{33} \end{bmatrix}$$

A.3 Tetrahedron Barycentric Coordinates

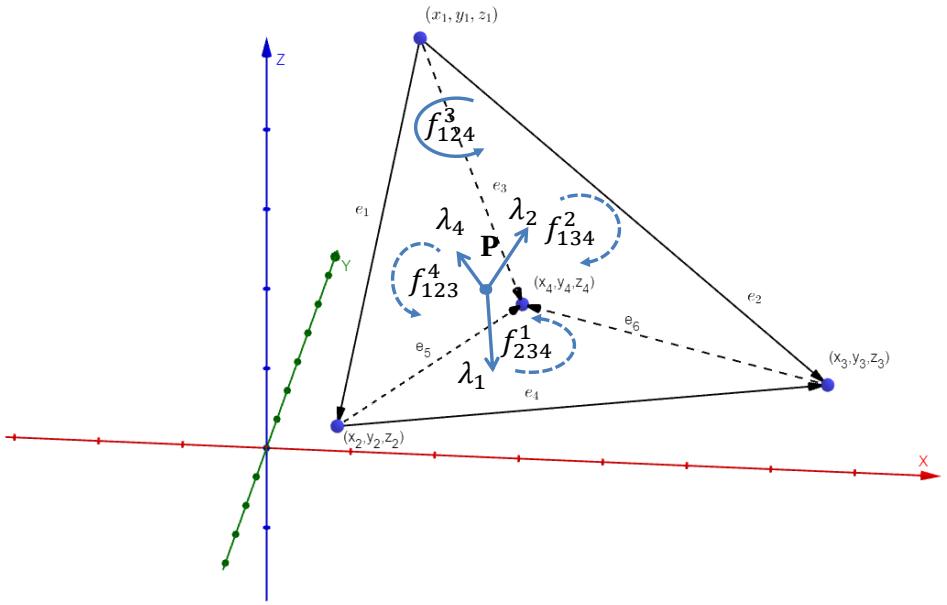

Figure A.1: Tetrahedron element

Let consider P is a point inside the tetrahedral. The tetrahedron is divided into four sub-tetrahedrons

$$V_1 = V_{P234}, \;\; V_2 = V_{P134}, \;\; V_3 = V_{P124}, \;\; V_4 = V_{P123}$$

The volume can be determined by

$$V_0 = \frac{1}{6}\begin{vmatrix} x_1 & y_1 & z_1 & 1 \\ x_2 & y_2 & z_2 & 1 \\ x_3 & y_3 & z_3 & 1 \\ x_4 & y_4 & z_4 & 1 \end{vmatrix}, \quad V_1 = \frac{1}{6}\begin{vmatrix} x & y & z & 1 \\ x_2 & y_2 & z_2 & 1 \\ x_3 & y_3 & z_3 & 1 \\ x_4 & y_4 & z_4 & 1 \end{vmatrix}, \quad V_2 = \frac{1}{6}\begin{vmatrix} x_1 & y_1 & z_1 & 1 \\ x & y & z & 1 \\ x_3 & y_3 & z_3 & 1 \\ x_4 & y_4 & z_4 & 1 \end{vmatrix},$$

$$V_3 = \frac{1}{6}\begin{vmatrix} x_1 & y_1 & z_1 & 1 \\ x_2 & y_2 & z_2 & 1 \\ x & y & z & 1 \\ x_4 & y_4 & z_4 & 1 \end{vmatrix}, \quad V_4 = \frac{1}{6}\begin{vmatrix} x_1 & y_1 & z_1 & 1 \\ x_2 & y_2 & z_2 & 1 \\ x_3 & y_3 & z_3 & 1 \\ x & y & z & 1 \end{vmatrix},$$

Based on linear interpolation, the barycentric coordinates of the point P are given by $\lambda_i = \frac{V_i}{V_0}$.

The determinant V_0 is related to the determinant of the so-called Jacobian, denoted by J which can be obtained from

$$J = (\boldsymbol{e}_1 \times \boldsymbol{e}_2) \cdot \boldsymbol{e}_3 = 6V_0$$

Since the λ_i are first order function, their gradients are constant:

$$\begin{aligned} \text{grad}(\lambda_1) &= \frac{\boldsymbol{e}_4 \times \boldsymbol{e}_5}{6V_0}, \quad \text{grad}(\lambda_2) = \frac{\boldsymbol{e}_2 \times \boldsymbol{e}_3}{6V_0}, \\ \text{grad}(\lambda_3) &= \frac{\boldsymbol{e}_3 \times \boldsymbol{e}_1}{6V_0}, \quad \text{grad}(\lambda_1) = \frac{\boldsymbol{e}_1 \times \boldsymbol{e}_2}{6V_0} \end{aligned}$$

A.4 Whitney element formulation basis function

A.4.1 Edge elements

$$\begin{aligned} N_e^1 = \lambda_1^e \overrightarrow{\nabla} \lambda_2^e - \lambda_2^e \overrightarrow{\nabla} \lambda_1^e, \quad N_e^2 = \lambda_1^e \overrightarrow{\nabla} \lambda_3^e - \lambda_3^e \overrightarrow{\nabla} \lambda_1^e, \quad N_e^3 = \lambda_1^e \overrightarrow{\nabla} \lambda_4^e - \lambda_4^e \overrightarrow{\nabla} \lambda_1^e, \\ N_e^4 = \lambda_2^e \overrightarrow{\nabla} \lambda_3^e - \lambda_3^e \overrightarrow{\nabla} \lambda_2^e, \quad N_e^5 = \lambda_2^e \overrightarrow{\nabla} \lambda_4^e - \lambda_4^e \overrightarrow{\nabla} \lambda_2^e, \quad N_e^6 = \lambda_3^e \overrightarrow{\nabla} \lambda_4^e - \lambda_4^e \overrightarrow{\nabla} \lambda_3^e \end{aligned}$$

A.4.2 Facet elements

$$\begin{aligned} N_f^1 &= 2(\lambda_2^e \overrightarrow{\nabla} \lambda_3^e \times \overrightarrow{\nabla} \lambda_4^e + \lambda_3^e \overrightarrow{\nabla} \lambda_4^e \times \overrightarrow{\nabla} \lambda_2^e + \lambda_4^e \overrightarrow{\nabla} \lambda_2^e \times \overrightarrow{\nabla} \lambda_3^e) \\ N_f^2 &= 2(\lambda_1^e \overrightarrow{\nabla} \lambda_3^e \times \overrightarrow{\nabla} \lambda_4^e + \lambda_3^e \overrightarrow{\nabla} \lambda_4^e \times \overrightarrow{\nabla} \lambda_1^e + \lambda_4^e \overrightarrow{\nabla} \lambda_1^e \times \overrightarrow{\nabla} \lambda_3^e) \\ N_f^3 &= 2(\lambda_1^e \overrightarrow{\nabla} \lambda_2^e \times \overrightarrow{\nabla} \lambda_4^e + \lambda_2^e \overrightarrow{\nabla} \lambda_4^e \times \overrightarrow{\nabla} \lambda_1^e + \lambda_4^e \overrightarrow{\nabla} \lambda_1^e \times \overrightarrow{\nabla} \lambda_2^e) \\ N_f^4 &= 2(\lambda_1^e \overrightarrow{\nabla} \lambda_2^e \times \overrightarrow{\nabla} \lambda_3^e + \lambda_2^e \overrightarrow{\nabla} \lambda_3^e \times \overrightarrow{\nabla} \lambda_1^e + \lambda_3^e \overrightarrow{\nabla} \lambda_1^e \times \overrightarrow{\nabla} \lambda_2^e) \end{aligned}$$

A.5 Incident matrices

The incidence matrices for a tetrahedron 1 2 3 4 are

$\boldsymbol{G}$	1 4	2 4	3 4	2 3	1 3	1 2
1	1	0	0	0	1	1
2	0	1	0	1	0	1
3	0	0	1	1	1	0
4	1	1	1	0	0	0

$\boldsymbol{C}$	2 3 4	1 3 4	1 2 4	1 2 3
1 4	0	1	1	0
2 4	1	0	1	0
3 4	1	1	0	0
2 3	1	0	0	1
1 3	0	1	0	1
1 2	0	0	1	1

In our problem, the dimension of incident matrices $\boldsymbol{C}$ and $\boldsymbol{G}$ can be expressed as $n_f \times n_e$ and $n_e \times n_n$ where n_f, n_e, n_n are respectively number of facets, edges and nodes. The value of incident matrix can be -1, 1 and 0. $C_{ij} = 0$ when the j_{th} edge does not locate with the i_{th} facet. Otherwise, j_{th} edge is one of the constituting of i_{th} facet. $C_{ij} = 1$ when the local orientation is consist with the global orientation and $C_{ij} = -1$ if not.

Appendix B

Material properties

B.1 Characteristics of utilized materials

B.1.1 PZT-5H

Elastic constants under electric field constant in 10^9 N m^{-2}.

$$\boldsymbol{c}^E = \begin{bmatrix} c_{11}^E & c_{12}^E & c_{13}^E & 0 & 0 & 0 \\ c_{21}^E & c_{22}^E & c_{23}^E & 0 & 0 & 0 \\ c_{31}^E & c_{32}^E & c_{33}^E & 0 & 0 & 0 \\ 0 & 0 & 0 & c_{44}^E & 0 & 0 \\ 0 & 0 & 0 & 0 & c_{55}^E & 0 \\ 0 & 0 & 0 & 0 & 0 & c_{44}^E \end{bmatrix}$$

$c_{11}^E = c_{22}^E = 127.21$, $c_{33}^E = 117.44$, $c_{12}^E = c_{21}^E = 80.21$, $c_{13}^E = c_{31}^E = c_{23}^E = c_{32}^E = 84.68$, $c_{44}^E = c_{55}^E = 22.99$, $c_{66}^E = 23.47$

Piezoelectric coefficients in C.m^{-2}.

$$\boldsymbol{e} = \begin{bmatrix} 0 & 0 & 0 & 0 & e_{15} & 0 \\ 0 & 0 & 0 & e_{24} & 0 & 0 \\ e_{31} & e_{32} & e_{33} & 0 & 0 & 0 \end{bmatrix}$$

$e_{31} = e_{32} = -6.62$, $e_{24} = e_{15} = 17.03$, $e_{33} = 23.24$

Permittivity

$$\boldsymbol{e} = \frac{1}{\varepsilon_0}\begin{bmatrix} \varepsilon_{11} & 0 & 0 \\ 0 & \varepsilon_{22} & 0 \\ 0 & 0 & \varepsilon_{33} \end{bmatrix}$$

$\varepsilon_{11} = \varepsilon_{22} = 1704$, $\varepsilon_{33} = 1433$

Density $\rho_E = 7500$ kg.m^{-3}

B.1.2 PZT-5A

Density:
$(\rho) = 7600$ kg.m^{-3}

Elastic stiffness (GPa):
$c_{11} = c_{22} = 138.5$, $c_{12} = 77.37$, $c_{13} = c_{23} = 73.64$, $c_{33} = 114.7$, $c_{44} = c_{55} = 25.6$, $c_{66} = 30.6$

Piezoelectric coefficients (C.m^{-2}):
$e_{31} = e_{32} = -5.2$, $e_{24} = e_{15} = 12.72$, $e_{33} = 15.08$

Relative permittivity:
$\varepsilon_{11} = \varepsilon_{22} = 1730$, $\varepsilon_{33} = 1700$

Relative permeability:
$\mu_{11} = \mu_{22} = \mu_{33} = 5.0$

B.1.3 P51

Density:
$(\rho) = 7600$ kg.m^{-3}

Elastic stiffness:
$E_y = 60$ GPa, $\nu_v = 0.36$

Piezoelectric coefficients (10^{-12} m/v):
$d_{31} = 186$, $d_{33} = 600$

Relative permittivity:
$\varepsilon_{11} = \varepsilon_{22} = \varepsilon_{33} = 2200$

B.1.4 BaTiO3

Density:
$(\rho) = 5800kg.m^{-3}$

Elastic constants:
$s_{11}^{E} = 34.38pm^2/N$, $s_{12}^{E} = -10.55pm^2/N$

Piezoelectric coefficients in $C.m^{-2}$:
$e_{31} = -4.4$,$e_{33} = 18.6$, $e_{15} = 11.6$

Relative permittivity:
$\varepsilon_{31} = \varepsilon_{33} = 1265$

B.1.5 Terfenol-D

Elastic stiffness (GPa):
$c_{11} = c_{22} = 35.87$, $c_{12} = 17.69$, $c_{13} = c23 = 23.25$, $c_{33} = 46.12$, $c_{44} = c_{55} = 4.166$, $c_{66} = 9.09$

Piezomagnetic coefficient $(NA^{-1}m^{-1})$:
$q_{31} = q_{32} = -32.63$, $q_{24} = 62.75$ $q_{15} = 150$, $q_{33} = 195.3$

Relative permeability:
$\mu_{11} = \mu_{22} = \mu_{33} = 9.3$

Relative permittivity:
$\varepsilon_{11} = \varepsilon_{22} = \varepsilon_{33} = 1.0$

B.1.6 Galfenol

Density:
$(\rho) = 9200$ kg.m^{-3}

Elastic constants:
$s_{11}^{H} = 220$ pm^2/N, $s_{12}^{H} = -55$ pm^2/N

B.1.7 DEAM parameter for Galfenol and Terfenol-D

	Galfenol	Terfenol-D
Ms (A/m)	$85.2*10^3$	$50*10^3$
λ_{100}	$75.31*10^{-6}$	$752.31*10^{-6}$
λ_{111}	0	0
K (J/m^3)	$35.58*10^3$	$35.58*10^3$
K_{100} (J/m^3)	412.18	412.18
Ω	630	9500

Bibliography

[1] W. C. Röntgen and J. Schneider, "Ueber die Compressibilität des Wassers," *Annalen der Physik*, vol. 269, no. 4, pp. 644–660, 1888.

[2] P. Curie, "Sur la symétrie dans les phénomènes physiques, symétrie d'un champ électrique et d'un champ magnétique," *Journal de Physique Théorique et Appliquée*, vol. 3, no. 1, pp. 393–415, 1894.

[3] S. Thomas, N. Kalarikkal, A. M. Stephan, and B. Raneesh, *Advanced Nanomaterials: Synthesis, Properties, and Applications*. CRC Press, June 2014. Google-Books-ID: coihAwAAQBAJ.

[4] S. Zhou, J. Wang, X. Chang, S. Wang, B. Qian, Z. Han, Q. Xu, J. Du, P. Wang, and S. Dong, "Magnetoelectricity coupled exchange bias in BaMnF4," *Scientific Reports*, vol. 5, p. 18392, Nov. 2016.

[5] M. Eibschütz and H. J. Guggenheim, "Antiferromagnetic-piezoelectric crystals: BaMe4 (M = Mn, Fe, Co and Ni)," *Solid State Communications*, vol. 6, pp. 737–739, Oct. 1968.

[6] C.-W. Nan, M. I. Bichurin, S. Dong, D. Viehland, and G. Srinivasan, "Multiferroic magnetoelectric composites: Historical perspective, status, and future directions," *Journal of Applied Physics*, vol. 103, p. 031101, Feb. 2008.

[7] J. P. J. Esq, "XVII. On the effects of magnetism upon the dimensions of iron and steel bars," *The London, Edinburgh, and Dublin Philosophical Magazine and Journal of Science*, vol. 30, pp. 76–87, Feb. 1847.

[8] Y. Kikuchi, "Magnetostrictive materials and applications," *IEEE Transactions on Magnetics*, vol. 4, pp. 107–117, June 1968.

[9] D. C. Jiles, "Theory of the magnetomechanical effect," *Journal of Physics D: Applied Physics*, vol. 28, pp. 1537–1546, Aug. 1995.

[10] A. E. Clark, B. F. DeSavage, and R. Bozorth, "Anomalous Thermal Expansion and Magnetostriction of Single-Crystal Dysprosium," *Physical Review*, vol. 138, pp. A216–A224, Apr. 1965.

[11] S. Legvold, J. Alstad, and J. Rhyne, "Giant Magnetostriction in Dysprosium and Holmium Single Crystals," *Physical Review Letters*, vol. 10, pp. 509–511, June 1963.

[12] A. E. Clark and M. Wun-Fogle, "Modern magnetostrictive materials: classical and nonclassical alloys," in *Smart Structures and Materials 2002: Active Materials: Behavior and Mechanics*, vol. 4699, pp. 421–437, International Society for Optics and Photonics, July 2002.

[13] A. Khachaturyan and D. Viehland, "Structurally Heterogeneous Model of Extrinsic Magnetostriction for Fe-Ga and Similar Magnetic Alloys: Part I. Decomposition and Confined Displacive Transformation," *Metallurgical and Materials Transactions A*, vol. 38, pp. 2308–2316, Sept. 2007.

[14] C. Mudivarthi, M. Laver, J. Cullen, A. B. Flatau, and M. Wuttig, "Origin of magnetostriction in Fe–Ga," *Journal of Applied Physics*, vol. 107, p. 09A957, May 2010.

[15] S. Karunanidhi and M. Singaperumal, "Design, analysis and simulation of magnetostrictive actuator and its application to high dynamic servo valve," *Sensors and Actuators A: Physical*, vol. 157, pp. 185–197, Feb. 2010.

[16] J. Daw, B. Tittmann, B. Reinhardt, G. Kohse, P. Ramuhalli, R. Montgomery, H.-T. Chien, J.-F. Villard, J. Palmer, and J. Rempe, "Irradiation testing of ultrasonic transducers," in *2013 3rd International Conference on Advancements in Nuclear Instrumentation, Measurement Methods and their Applications (ANIMMA)*, (Marseille, France), pp. 1–7, IEEE, June 2013.

[17] E. Hristoforou, "Magnetostrictive delay lines: engineering theory and sensing applications," *Measurement Science and Technology*, vol. 14, pp. R15–R47, Jan. 2003.

[18] G. Gautschi, *Piezoelectric Sensorics: Force Strain Pressure Acceleration and Acoustic Emission Sensors Materials and Amplifiers*. Berlin Heidelberg: Springer-Verlag, 2002.

[19] J. Curie and P. Curie, "Développement par compression de l'électricité polaire dans les cristaux hémièdres à faces inclinées," *Bulletin de Minéralogie*, vol. 3, no. 4, pp. 90–93, 1880.

[20] X. Mininger, E. Lefeuvre, M. Gabsi, C. Richard, and D. Guyomar, "Semiactive and active piezoelectric vibration controls for switched reluctance machine," *IEEE Transactions on Energy conversion*, vol. 23, no. 1, pp. 78–85, 2008.

[21] B. İlik, A. Koyuncuoğlu, z. Şardan Sukas, and H. Külah, "Thin film piezoelectric acoustic transducer for fully implantable cochlear implants," *Sensors and Actuators A: Physical*, vol. 280, pp. 38–46, Sept. 2018.

[22] M. Zhou, Y. Ruan, W. Liu, S. Huang, and X. Fu, "A bio-inspired piezoelectric motor with simple structured asymmetric stator," *Smart Materials and Structures*, vol. 23, p. 045003, Feb. 2014.

[23] M. Han, H. Wang, Y. Yang, C. Liang, W. Bai, Z. Yan, H. Li, Y. Xue, X. Wang, B. Akar, H. Zhao, H. Luan, J. Lim, I. Kandela, G. A. Ameer, Y. Zhang, Y. Huang, and J. A. Rogers, "Three-dimensional piezoelectric polymer microsystems for vi-

brational energy harvesting, robotic interfaces and biomedical implants," *Nature Electronics*, vol. 2, p. 26, Jan. 2019.

[24] R. E. Newnham, D. P. Skinner, and L. E. Cross, "Connectivity and piezoelectric-pyroelectric composites," *Materials Research Bulletin*, vol. 13, pp. 525–536, May 1978.

[25] Y. Wang, J. Hu, Y. Lin, and C.-W. Nan, "Multiferroic magnetoelectric composite nanostructures," *NPG Asia Materials*, vol. 2, pp. 61–68, Apr. 2010.

[26] S. Priya, R. Islam, S. Dong, and D. Viehland, "Recent advancements in magnetoelectric particulate and laminate composites," *Journal of Electroceramics*, vol. 19, pp. 149–166, Sept. 2007.

[27] Y. Liu, X. Ruan, B. Zhu, S. Chen, Z. Lu, J. Shi, and R. Xiong, "CoFe2o4/BaTiO3 Composites via Spark Plasma Sintering with Enhanced Magnetoelectric Coupling and Excellent Anisotropy," *Journal of the American Ceramic Society*, vol. 94, no. 6, pp. 1695–1697, 2011.

[28] H. Zheng, J. Wang, S. E. Lofland, Z. Ma, L. Mohaddes-Ardabili, T. Zhao, L. Salamanca-Riba, S. R. Shinde, S. B. Ogale, F. Bai, D. Viehland, Y. Jia, D. G. Schlom, M. Wuttig, A. Roytburd, and R. Ramesh, "Multiferroic BaTiO3-CoFe2o4 Nanostructures," *Science*, vol. 303, pp. 661–663, Jan. 2004.

[29] C. W. Nan, M. Li, and J. H. Huang, "Calculations of giant magnetoelectric effects in ferroic composites of rare-earth–iron alloys and ferroelectric polymers," *Physical Review B*, vol. 63, p. 144415, Mar. 2001.

[30] Y. Li, Z. Wang, J. Yao, T. Yang, Z. Wang, J.-M. Hu, C. Chen, R. Sun, Z. Tian, J. Li, L.-Q. Chen, and D. Viehland, "Magnetoelectric quasi-(0-3) nanocomposite heterostructures," *Nature Communications*, vol. 6, p. 6680, Dec. 2015.

[31] K. Lefki and G. J. M. Dormans, "Measurement of piezoelectric coefficients of ferroelectric thin films," *Journal of Applied Physics*, vol. 76, pp. 1764–1767, Aug. 1994.

[32] C.-W. Nan, "Magnetoelectric effect in composites of piezoelectric and piezomagnetic phases," *Physical Review B*, vol. 50, pp. 6082–6088, Sept. 1994.

[33] K. Malleron, A. Gensbittel, H. Talleb, and Z. Ren, "Etude expérimentale d'un transducteur magnétoélectrique pour les besoins de la télé-alimentation de capteurs biomédicaux implantés.," in *Journées d'Etude sur la TéléSANté, 6ème edition*, (Bourges, France), Pôle Capteurs, Université d'Orléans, May 2017.

[34] J. Zhai, S. Dong, Z. Xing, J. Li, and D. Viehland, "Giant magnetoelectric effect in Metglas/polyvinylidene-fluoride laminates," *Applied Physics Letters*, vol. 89, no. 8, p. 083507, 2006.

[35] M. Batty, K. W. Axhausen, F. Giannotti, A. Pozdnoukhov, A. Bazzani, M. Wa-

chowicz, G. Ouzounis, and Y. Portugali, "Smart cities of the future," *The European Physical Journal Special Topics*, vol. 214, pp. 481–518, Nov. 2012.

[36] D. McLaren and J. Agyeman, *Sharing Cities: A Case for Truly Smart and Sustainable Cities*. MIT Press, Nov. 2015. Google-Books-ID: KhvLCgAAQBAJ.

[37] L. Columbus, "Roundup Of Internet Of Things Forecasts And Market Estimates, 2016."

[38] E. Lefeuvre, A. Badel, A. Brenes, S. Seok, and C.-S. Yoo, "Power and frequency bandwidth improvement of piezoelectric energy harvesting devices using phase-shifted synchronous electric charge extraction interface circuit," *Journal of Intelligent Material Systems and Structures*, vol. 28, no. 20, pp. 2988–2995, 2017.

[39] R. Xie, N. Ishijima, H. Sugime, and S. Noda, "Enhancing the photovoltaic performance of hybrid heterojunction solar cells by passivation of silicon surface via a simple 1-min annealing process," *Scientific reports*, vol. 9, no. 1, pp. 1–7, 2019.

[40] M. D. S. Soares, J. Ferreira, J. Simões, R. Pascoal, J. Torrão, X. Xue, and E. P. Furlani, "Magnetic levitation-based electromagnetic energy harvesting: a semi-analytical non-linear model for energy transduction.," *Scientific reports*, vol. 6, pp. 18579–18579, 2016.

[41] S. P. Beeby, M. J. Tudor, and N. M. White, "Energy harvesting vibration sources for microsystems applications," *Measurement Science and Technology*, vol. 17, pp. R175–R195, Oct. 2006.

[42] J. A. Paradiso and T. Starner, "Energy scavenging for mobile and wireless electronics," *IEEE Pervasive Computing*, vol. 4, pp. 18–27, Jan. 2005.

[43] S. Priya, J. Ryu, C.-S. Park, J. Oliver, J.-J. Choi, and D.-S. Park, "Piezoelectric and Magnetoelectric Thick Films for Fabricating Power Sources in Wireless Sensor Nodes," *Sensors (Basel, Switzerland)*, vol. 9, pp. 6362–6384, Aug. 2009.

[44] R. C. Kambale, W.-H. Yoon, D.-S. Park, J.-J. Choi, C.-W. Ahn, J.-W. Kim, B.-D. Hahn, D.-Y. Jeong, B. Chul Lee, G.-S. Chung, and J. Ryu, "Magnetoelectric properties and magnetomechanical energy harvesting from stray vibration and electromagnetic wave by Pb(Mg1/3nb2/3)O3-Pb(Zr,Ti)O3 single crystal/Ni cantilever," *Journal of Applied Physics*, vol. 113, p. 204108, May 2013.

[45] P. Martins and S. Lanceros-Méndez, "Polymer-Based Magnetoelectric Materials," *Advanced Functional Materials*, vol. 23, no. 27, pp. 3371–3385, 2013.

[46] G. Srinivasan, E. T. Rasmussen, J. Gallegos, R. Srinivasan, Y. I. Bokhan, and V. M. Laletin, "Magnetoelectric bilayer and multilayer structures of magnetostrictive and piezoelectric oxides," *Physical Review B*, vol. 64, p. 214408, Nov. 2001.

[47] P. Li, Y. Wen, C. Jia, and X. Li, "A MAGNETOELECTRIC ENERGY HARVESTER AND MANAGEMENT CIRCUIT," 2009.

[48] Y. Zhou, D. J. Apo, M. Sanghadasa, M. Bichurin, V. M. Petrov, and S. Priya, "7 - Magnetoelectric energy harvester," in *Composite Magnetoelectrics* (G. Srinivasan, S. Priya, and N. X. Sun, eds.), Woodhead Publishing Series in Electronic and Optical Materials, pp. 161–207, Woodhead Publishing, Jan. 2015.

[49] M. Kumari, C. Prakash, and R. Chatterjee, "Room temperature large self-biased magnetoelectric effect in non-lead based piezoelectric and magnetostrictive (0-3) particulate composite system," *Journal of Magnetism and Magnetic Materials*, vol. 429, pp. 60–64, May 2017.

[50] Y. Cheng, B. Peng, Z. Hu, Z. Zhou, and M. Liu, "Recent development and status of magnetoelectric materials and devices," *Physics Letters A*, vol. 382, pp. 3018–3025, Oct. 2018.

[51] Y. Hui, T. X. Nan, N. X. Sun, and M. Rinaldi, "MEMS resonant magnetic field sensor based on an AlN/FeGaB bilayer nano-plate resonator," in *2013 IEEE 26th International Conference on Micro Electro Mechanical Systems (MEMS)*, pp. 721–724, Jan. 2013.

[52] T. Nan, Y. Hui, M. Rinaldi, and N. X. Sun, "Self-Biased 215mhz Magnetoelectric NEMS Resonator for Ultra-Sensitive DC Magnetic Field Detection," *Scientific Reports*, vol. 3, p. 1985, June 2013.

[53] R. Guduru, P. Liang, M. Yousef, J. Horstmyer, and S. Khizroev, "Mapping the Brain's electric fields with Magnetoelectric nanoparticles," *Bioelectronic Medicine*, vol. 4, p. 10, Aug. 2018.

[54] D. Gun Lee, S. Man Kim, Y. Kyung Yoo, J. Hyun Han, D. Won Chun, Y.-C. Kim, J. Kim, K. Seon Hwang, T. Song Kim, W. Woo Jo, H. Kim, S.-H. Song, and J. Hoon Lee, "Ultra-sensitive magnetoelectric microcantilever at a low frequency," *Applied Physics Letters*, vol. 101, p. 182902, Oct. 2012.

[55] V. Röbisch, S. Salzer, N. O. Urs, J. Reermann, E. Yarar, A. Piorra, C. Kirchhof, E. Lage, M. Höft, G. U. Schmidt, R. Knöchel, J. McCord, E. Quandt, and D. Meyners, "Pushing the detection limit of thin film magnetoelectric heterostructures," *Journal of Materials Research*, vol. 32, pp. 1009–1019, Mar. 2017.

[56] A. S. Tatarenko, G. Srinivasan, and M. I. Bichurin, "Magnetoelectric microwave phase shifter," *Applied Physics Letters*, vol. 88, p. 183507, May 2006.

[57] A. S. Tatarenko, D. V. B. Murthy, and G. Srinivasan, "Hexagonal ferrite-piezoelectric composites for dual magnetic and electric field tunable 8–25 GHz microstripline resonators and phase shifters," *Microwave and Optical Technology Letters*, vol. 54, no. 5, pp. 1215–1218, 2012.

[58] J. Lou, D. Reed, M. Liu, and N. X. Sun, "Electrostatically tunable magnetoelectric inductors with large inductance tunability," *Applied Physics Letters*, vol. 94, p. 112508, Mar. 2009.

[59] W. Voigt, *Lehrbuch der Kristallphysik*. Wiesbaden: Vieweg+Teubner Verlag, 1966.

[60] "IEEE Standard on Piezoelectricity," *ANSI/IEEE Std 176-1987*, pp. 0_1–, 1988.

[61] "IEEE Standard on Magnetostrictive Materials: Piezomagnetic Nomenclature," *IEEE Std 319-1990*, pp. 1–, 1991.

[62] D. C. Jiles and D. L. Atherton, "Theory of ferromagnetic hysteresis," *Journal of Magnetism and Magnetic Materials*, vol. 61, pp. 48–60, Sept. 1986.

[63] J. Kim and E. Jung, "Finite element analysis for acoustic characteristics of a magnetostrictive transducer," *Smart Materials and Structures*, vol. 14, pp. 1273–1280, Oct. 2005.

[64] W. D. Armstrong, "An incremental theory of magneto-elastic hysteresis in pseudo-cubic ferro-magnetostrictive alloys," *Journal of Magnetism and Magnetic Materials*, vol. 263, pp. 208–218, July 2003.

[65] L. Daniel, "An Analytical Model for the Effect of Multiaxial Stress on the Magnetic Susceptibility of Ferromagnetic Materials," *IEEE Transactions on Magnetics*, vol. 49, pp. 2037–2040, May 2013.

[66] P. G. Evans and M. J. Dapino, "Efficient magnetic hysteresis model for field and stress application in magnetostrictive Galfenol," *Journal of Applied Physics*, vol. 107, p. 063906, Mar. 2010.

[67] J. Íñiguez, "First-Principles Approach to Lattice-Mediated Magnetoelectric Effects," *Physical Review Letters*, vol. 101, p. 117201, Sept. 2008.

[68] E. Bousquet, N. A. Spaldin, and K. T. Delaney, "Unexpectedly Large Electronic Contribution to Linear Magnetoelectricity," *Physical Review Letters*, vol. 106, p. 107202, Mar. 2011.

[69] S. Prosandeev, I. A. Kornev, and L. Bellaiche, "Magnetoelectricity in BiFeO 3 films: First-principles-based computations and phenomenology," *Physical Review B*, vol. 83, p. 020102, Jan. 2011.

[70] W. Ren and L. Bellaiche, "Size effects in multiferroic BiFeO 3 nanodots: A first-principles-based study," *Physical Review B*, vol. 82, p. 113403, Sept. 2010.

[71] S. Butterworth and F. D. Smith, "The equivalent circuit of the magnetostriction oscillator," *Proceedings of the Physical Society*, vol. 43, pp. 166–185, Mar. 1931.

[72] G. Srinivasan, E. T. Rasmussen, B. J. Levin, and R. Hayes, "Magnetoelectric effects in bilayers and multilayers of magnetostrictive and piezoelectric perovskite oxides," *Physical Review B*, vol. 65, p. 134402, Mar. 2002.

[73] K. Mori and M. Wuttig, "Magnetoelectric coupling in Terfenol-

D/polyvinylidenedifluoride composites," *Applied Physics Letters*, vol. 81, pp. 100–101, July 2002.

[74] M. Avellaneda and G. Harshé, "Magnetoelectric Effect in Piezoelectric/Magnetostrictive Multilayer (2-2) Composites," *Journal of Intelligent Material Systems and Structures*, vol. 5, pp. 501–513, July 1994.

[75] I. A. Osaretin and R. G. Rojas, "Theoretical model for the magnetoelectric effect in magnetostrictive/piezoelectric composites," *Physical Review B*, vol. 82, p. 174415, Nov. 2010.

[76] S. Dong and J. Zhai, "Equivalent circuit method for static and dynamic analysis of magnetoelectric laminated composites," *Chinese Science Bulletin*, vol. 53, pp. 2113–2123, July 2008.

[77] D. A. Filippov, M. I. Bichurin, C. W. Nan, and J. M. Liu, "Magnetoelectric effect in hybrid magnetostrictive-piezoelectric composites in the electromechanical resonance region," *Journal of Applied Physics*, vol. 97, p. 113910, June 2005.

[78] M. Bichurin and V. Petrov, "Magnetoelectric Effect in Electromechanical Resonance Region," in *Modeling of Magnetoelectric Effects in Composites* (M. Bichurin and V. Petrov, eds.), Springer Series in Materials Science, pp. 57–73, Dordrecht: Springer Netherlands, 2014.

[79] Y. Wang, D. Hasanyan, M. Li, J. Gao, J. Li, D. Viehland, and H. Luo, "Theoretical model for geometry-dependent magnetoelectric effect in magnetostrictive/piezoelectric composites," *Journal of Applied Physics*, vol. 111, p. 124513, June 2012.

[80] H.-M. Zhou, X.-W. Ou, Y. Xiao, S.-X. Qu, and H.-P. Wu, "An analytical nonlinear magnetoelectric coupling model of laminated composites under combined pre-stress and magnetic bias loadings," *Smart Materials and Structures*, vol. 22, p. 035018, Feb. 2013.

[81] G. Liu, C. Zhang, W. Chen, and S. Dong, "Eddy-current effect on resonant magnetoelectric coupling in magnetostrictive-piezoelectric laminated composites," *Journal of Applied Physics*, vol. 114, p. 027010, July 2013.

[82] D. Davino, A. Giustiniani, C. Visone, and W. Zamboni, "Stress-Induced Eddy Currents in Magnetostrictive Energy Harvesting Devices," *IEEE Transactions on Magnetics*, vol. 48, pp. 18–25, Jan. 2012.

[83] H. Talleb and Z. Ren, "Finite element modeling of magnetoelectric laminate composites in considering nonlinear and load effects for energy harvesting," *Journal of Alloys and Compounds*, vol. 615, pp. 65–74, 2014.

[84] T. T. Nguyen, *Modélisation par éléments finis de matériaux composites magnéto-électriques*. PhD thesis, Université Paris Sud-Paris XI, 2011.

[85] T. T. Nguyen, X. Mininger, F. Bouillault, and L. Daniel, "Finite element harmonic modeling of magnetoelectric effect," *IEEE Transactions on Magnetics*, vol. 47, no. 5, pp. 1142–1145, 2011.

[86] T. T. Nguyen, F. Bouillault, L. Daniel, and X. Mininger, "Finite element modeling of magnetic field sensors based on nonlinear magnetoelectric effect," *Journal of Applied Physics*, vol. 109, no. 8, p. 084904, 2011.

[87] K. Malleron, H. Talleb, A. Gensbittel, and Z. Ren, "Finite-Element Modeling of Magnetoelectric Energy Transducers With Interdigitated Electrodes," *IEEE Transactions on Magnetics*, vol. 53, pp. 1–4, June 2017.

[88] N. Galopin, X. Mininger, F. Frederic, and L. Daniel, "Finite Element Modeling of Magnetoelectric Sensors," *IEEE Transactions on Magnetics*, vol. 44, pp. 834–837, June 2008.

[89] V. Piefort, "Finite Element Modelling of Piezoelectric Active Structures," p. 154.

[90] A. Belahcen, *Magnetoelasticity, magnetic forces and magnetostriction in electrical machines*. Helsinki University of Technology, Aug. 2004.

[91] K. Azoum, *Contribution à la modélisation numérique de phénomènes magnéto-élastiques : étude de dispositifs à base de matériaux magnétostrictifs*. thesis, Paris 11, Jan. 2005.

[92] N. Galopin, "Modélisation et caractérisation de matériaux actifs pour la conception de dispositifs magnéto-électriques," Dec. 2007.

[93] T. Ueno and T. Higuchi, "Magnetic sensor for high temperature using a laminate composite of magnetostrictive material and piezoelectric material," in *Smart Structures and Materials 2005: Active Materials: Behavior and Mechanics*, vol. 5761, pp. 156–163, International Society for Optics and Photonics, May 2005.

[94] H. Talleb, A. Gensbittel, and Z. Ren, "Multiphysics modeling of a magnetoelectric composite Rosen-type device," *Composite Structures*, vol. 137, pp. 1–8, 2016.

[95] H. Talleb, A. Gensbittel, and Z. Ren, "Multiphysics modeling of multiferroic artificial materials by the finite element method," *The European Physical Journal Applied Physics*, vol. 73, p. 30901, Mar. 2016.

[96] M. J. Dapino, R. C. Smith, L. E. Faidley, and A. B. Flatau, "A Coupled Structural-Magnetic Strain and Stress Model for Magnetostrictive Transducers," *Journal of Intelligent Material Systems and Structures*, vol. 11, pp. 135–152, Feb. 2000.

[97] G. Yang, *Contribution to modelling of magnetoelectric composites for energy harvesting*. Theses, Université Pierre et Marie Curie - Paris VI, Dec. 2016.

[98] Q. H. Jiang, Z. J. Shen, J. P. Zhou, Z. Shi, and C.-W. Nan, "Magnetoelectric

composites of nickel ferrite and lead zirconnate titanate prepared by spark plasma sintering," *Journal of the European Ceramic Society*, vol. 27, pp. 279–284, Jan. 2007.

[99] A. Aubert, V. Loyau, F. Mazaleyrat, and M. LoBue, "Enhancement of the Magnetoelectric Effect in Multiferroic CoFe $_2$ O $_4$ /PZT Bilayer by Induced Uniaxial Magnetic Anisotropy," *IEEE Transactions on Magnetics*, vol. 53, pp. 1–5, Nov. 2017.

[100] Fu-Sheng Hsiao, Jen-Ai Chao, and Yi-Cheng Huang, "3d finite element analysis and experiment on the piezoelectric ultrasonic transducer motion," in *2009 International Conference on Mechatronics and Automation*, (Changchun, China), pp. 158–163, IEEE, Aug. 2009.

[101] D. Braess and M. Kaltenbacher, "Efficient 3d-finite element formulation for thin mechanical and piezoelectric structures," *INTERNATIONAL JOURNAL FOR NUMERICAL METHODS IN ENGINEERING Int. J. Numer. Meth. Engng*, vol. 06, pp. 1–6, Jan. 2000.

[102] M. Schinnerl, M. Kaltenbacher, U. Langer, R. Lerch, and J. Schöberl, "A Survey in Mathematics for Industry An efficient method for the numerical simulation of magneto-mechanical sensors and actuators," *European Journal of Applied Mathematics*, vol. 18, pp. 233–271, Apr. 2007.

[103] P. G. Evans and M. J. Dapino, "Dynamic Model for 3-D Magnetostrictive Transducers," *IEEE Transactions on Magnetics*, vol. 47, pp. 221–230, Jan. 2011.

[104] "The Finite Element Method in Electromagnetics, 3rd Edition."

[105] O. Bíró, "Edge element formulations of eddy current problems," *Computer Methods in Applied Mechanics and Engineering*, vol. 169, pp. 391–405, Feb. 1999.

[106] Z. Qin, *Finite Element Modeling and PGD Based Model Reduction for Piezoelectric & Magnetostrictive Materials*. PhD thesis, University Pierre Marie Curie, 2016.

[107] Z. Qin, H. Talleb, J.-Y. Duquesne, M. Marangolo, and Z. Ren, "Finite-element modeling of thermoelastic attenuation in piezoelectric surface acoustic wave devices," *IEEE Transactions on Magnetics*, vol. 51, no. 3, pp. 1–4, 2015.

[108] M. J. Dapino and S. Chakrabarti, "Modeling of 3d Magnetostrictive Systems with Application to Galfenol and Terfenol-D Actuators," 2013.

[109] S. Chakrabarti and M. J. Dapino, "Nonlinear finite element model for 3d Galfenol systems," *Smart Materials and Structures*, vol. 20, p. 105034, Sept. 2011.

[110] H. Tari, J. J. Scheidler, and M. J. Dapino, "Robust solution procedure for the discrete energy-averaged model on the calculation of 3d hysteretic magnetization and magnetostriction of iron–gallium alloys," *Journal of Magnetism and Magnetic Materials*, vol. 384, pp. 266–275, June 2015.

[111] A. Bossavit, *Computational Electromagnetism: Variational Formulations, Com-*

plementarity, Edge Elements. Academic Press, Feb. 1998. Google-Books-ID: RQ_9hc8U7MsC.

[112] A. Bossavit, "Whitney forms: a class of finite elements for three-dimensional computations in electromagnetism," *IEE Proceedings A - Physical Science, Measurement and Instrumentation, Management and Education - Reviews*, vol. 135, pp. 493–500, Nov. 1988.

[113] S. Chakrabarti and M. J. Dapino, "Fully coupled discrete energy-averaged model for Terfenol-D," *Journal of Applied Physics*, vol. 111, p. 054505, Mar. 2012.

[114] G. Nader, E. C. N. Silva, and J. C. Adamowski, "Determination of piezoelectric transducer damping by using experimental and finite element simulations," in *Smart Structures and Materials 2003: Damping and Isolation*, vol. 5052, pp. 116–128, International Society for Optics and Photonics, July 2003.

[115] L. Wang, Z. Du, C. Fan, L. Xu, H. Zhang, and D. Zhao, "Effect of load resistance on magnetoelectric properties in FeGa/BaTiO 3/FeGa laminate composites," *Journal of Alloys and Compounds*, vol. 509, no. 30, pp. 7870–7873, 2011.

[116] R. Myers, R. A. Islam, M. Karmarkar, and S. Priya, "Magnetoelectric laminate composite based tachometer for harsh environment applications," *Applied Physics Letters*, vol. 91, p. 122904, Sept. 2007.

[117] Y. Zong, T. Zheng, P. Martins, S. Lanceros-Mendez, Z. Yue, and M. J. Higgins, "Cellulose-based magnetoelectric composites," *Nature Communications*, vol. 8, Dec. 2017.

[118] J. Wen, J. Zhang, and Y. Gao, "A coupling finite element model for analysis the nonlinear dynamic magnetoelectric response of tri-layer laminate composites," *Composite Structures*, vol. 166, pp. 163–176, Apr. 2017.

[119] X. Mininger, N. Galopin, Y. Dennemont, and F. Bouillault, "3d finite element model for magnetoelectric sensors," *The European Physical Journal - Applied Physics*, vol. 52, Nov. 2010.

[120] H. Talleb and Z. Ren, "Finite-element modeling of a magnetoelectric energy transducer including the load effect," *IEEE Transactions on Magnetics*, vol. 51, no. 3, pp. 1–5, 2015.

[121] S. S. Vadla, A. R. Kulkarni, and V. Narayanan, "Magnetoelectric coupling in 0.5pb(Ni1/3nb2/3)O3–0.35pbtio3–0.15pbzro3 and CoFe2o4 based particulate composites," *Scripta Materialia*, vol. 112, pp. 140–143, Feb. 2016.

[122] S. Schmauder and I. Schäfer, *Multiscale Materials Modeling: Approaches to Full Multiscaling*. Walter de Gruyter GmbH & Co KG, Aug. 2016. Google-Books-ID: FOk5DQAAQBAJ.

[123] J. Y. Li and M. L. Dunn, "Micromechanics of Magnetoelectroelastic Composite

Materials: Average Fields and Effective Behavior," *Journal of Intelligent Material Systems and Structures*, vol. 9, pp. 404–416, June 1998.

[124] R. Corcolle, L. Daniel, and F. Bouillault, "Generic formalism for homogenization of coupled behavior: Application to magnetoelectroelastic behavior," *Physical Review B*, vol. 78, p. 214110, Dec. 2008.

[125] J. Lee, J. G. Boyd, and D. C. Lagoudas, "Effective properties of three-phase electro-magneto-elastic composites," *International Journal of Engineering Science*, vol. 43, pp. 790–825, June 2005.

[126] V. D. Nguyen, E. Béchet, C. Geuzaine, and L. Noels, "Imposing periodic boundary condition on arbitrary meshes by polynomial interpolation," *Computational Materials Science*, vol. 55, pp. 390–406, Apr. 2012.

[127] R. Corcolle, L. Daniel, and F. Bouillault, "Optimal Design of Magnetostrictive Composites: An Analytical Approach," *IEEE Transactions on Magnetics*, vol. 44, pp. 17–23, Jan. 2008.

[128] Y. Zhou and F. G. Shin, "Modeling of magnetostriction in particulate composite materials," *IEEE Transactions on Magnetics*, vol. 41, pp. 2071–2076, June 2005.